GFZ Helmholtz Centre Potsdam

Freie Universität Berlin

Magnetotelluric Investigation of the Sipoholon Geothermal Field, Indonesia

Sintia W. Niasari

Dissertation
zur Erlangung des akademischen Grades
doctor rerum naturalium (Dr. rer. nat.)
im Fachbereich Geowissenschaften
der Freien Universität Berlin

Berlin, 2015

Erstgutachter	**Zweitgutachter**
PD Dr. Oliver Ritter	Prof. Dr. Serge A. Shapiro
(Freie Universität Berlin,	(Freie Universität Berlin)
GeoForschungsZentrum Potsdam)	

Tag der Disputation: 09.01.2015

Abstract

The Sipoholon geothermal system is located in the vicinity the Tarutung basin, which is part of the Sumatra fault system, Indonesia. In the Sipoholon area, 18 hot springs indicate interconnected (hot saline) fluids in the subsurface. The hot saline fluids in the rock pore space increase the bulk electrical conductivity. Hence, an electrical conductivity model can be analysed based on the dependence of resistivity on porosity, fluid conductivity and temperature.

Here, I present a magnetotelluric (MT) study which provides the electrical conductivity distribution at depth of the Sipoholon geothermal system. The main objective of this study is to develop a conceptual model for the Sipoholon geothermal system based on the conductivity distribution at depth. Together with additional geological, geochemical, and seismological studies, the MT results infer a comprehensive understanding about the Sipoholon geothermal system, particularly about the reservoir and the heat source.

The MT data reveal a deep reaching conductive anomaly (< 10 Ωm) approximately 6 km to the east of the Tarutung basin. This conductor is associated spatially with the Panabungan normal fault zone and the Panabungan hot spring. At shallow depths, i.e. from surface to 3 km depth, the conductivity anomaly could be caused by ascending magmatic and/or meteoric water from a deeper zone. At depths of 1 km until 2 km, the vertical conductor shows a resistivity of 2 Ωm, which is most likely the location of a possible reservoir.

Below the reservoir, the deep reaching conductive anomaly is interpreted as circulating hot fluids which heat up the fluids in the reservoir. It is likely that the heat is caused by magmatic activity related to the subduction process. This interpretation is consistent with geochemical studies which indicate magmatic origin of fluids sampled from the Panabungan hot spring.

About 2 km to the south-west of the Tarutung basin, a shallow conductive body is revealed at depths of 0.5-2 km beneath cold springs close to the inactive Martimbang volcano. This conductor is interpreted as Andesitic material which was altered by high temperatures in the past due to the magma intrusion of the Martimbang. Geochemical and geophysical studies,

including MT, do not support a hypothesis that the heat source of the Sipoholon geothermal system is related to the inactive Martimbang volcano.

A shallow conductive anomaly is also revealed beneath the Tarutung basin. This shallow conductor is interpreted as unconsolidated sediments of volcanic origin (Quaternary Toba Tuff). In the westernmost part of the study area, a very resistive region corresponds to Permian granites. This resistor is interpreted as the western border of the Sipoholon geothermal system.

In summary, the resistivity models from this study display the previously unknown fluid distribution of the Sipoholon non-volcanic geothermal system. This interpretation is consistent with the high porosity of surface rocks and the distribution of low Vp and high Vp/Vs observed around the Panabungan hot spring. Combined with other geoscience disciplines, MT is a very powerful geothermal exploration tool because of its sensitivity to image hot saline fluids as zones of high conductivity.

Kurzfassung

Das Geothermie-System Sipoholon befindet sich um das Tarutung-Becken, das Teil des Sumatra-Störungssystems ist. In dieser Region weisen 18 Heißwasserquellen auf miteinander verbundene (heiße salzhaltige) Fluide in den Untergrund hin. Heißen salzhaltige Fluide in den Gesteinporen erhöhen die Volumenleitfähigkeit. Daher kann ein Model der elektrischen Leitfähigkeit erstellt werden, das von der Porosität, Leitfähigkeit der Fluide und der Temperatur abhängt.

Hier, stelle ich eine magnetotellurische (MT) Studie vor welche die elektrische Leitfähigkeitsverteilung des Untergrunds im Sipoholon Geothermie-System zeigt. Diese Leitfähigkeitsverteilung kann mit den bekannten geologischen Einheiten in Zusammenhang gebracht werden, was auch mögliche Fluidwege einschließt. Das Hauptziel der vorliegenden Studie ist es, ein konzeptionelles Modell des Sipoholon Geothermie-Systems anhand der Leitfähigkeitsverteilung in der Tiefe zu entwickeln. Zusammen mit weiteren geologischen, geochemischen und seismologische Studien ergeben, die MT-Ergebnisse ein aussagekräftig Bild des Sipoholon Geothermie-Systems, insbesondere des Reservoirs und Wärmequelle.

Die MT-Daten zeigen eine tiefereichende leitfähige Anomalie (<10 Ωm) ca. 6 km östlich vom Tarutung-Becken. Dieser Leiter ist räumlich mit der Panabungan-Störungszone und der Panabungan-Heißwasserquelle verbunden. In geringen Tiefen, d.h. von der Oberfläche bis 3 km Tiefe, kann die Leitfähigkeitsanomalie durch aufsteigendes magmatisches und /oder Niederschlagswasser aus einer tieferen Zone verursacht werden. In einer Tiefe von 1 bis 2 km, zeigt der vertikale Leiter einen spezifischen Widerstand von 2 Ωm, was höchstwahrseheinlich auf die Lage des Reservoirs hindeutet.

Die tiefreichende leitfähige Anomalie unterhalb des Reservoirs wird auf die zirkulierenden heißen Fluide zurückgeführt, welche die Fluide im Reservoirs aufheizen. Es ist wahrscheinlich, dass die Wärme, durch magmatische Aktivität aufgrund des Subduktionsprozesses verursacht wird. Diese Interpretation steht im Einklang mit geochemischen Untersuchungen, die einen magmatischen Ursprung der Fluide aus der Panabungan-Heißwasserquelle annehmen.

Ca. 2 km süd-westlich vom Tarutung-Becken wird ein flacher leitfähige Körper in einer Tiefe von 0,5-2 km angezeigt, der unter kalten Quellen in der Nähe des inaktiven Vulkans Martimbang liegt. Dieser Leiter wird als andesitisches Material interpretiert, das mineralisch durch hohe Temperaturen aufgrund der Magma Intrusion des Martimbang verändert wurde. Geochemische und geophysikalische Studien, einschließlich MT, unterstützen nicht die Hypothese, dass die Wärmequelle des Sipoholon Geothermie-Systems direkt mit dem inaktiven Vulkan Martimbang in Beziehung steht.

Eine flache leitfähige Anomalie wird auch unter dem Tarutung-Becken sichtbar. Dieser flache Leiter wird als Lockersedimente vulkanischen Ursprungs (Quaternary Toba Tuff) interpretiert. Im westlichsten Teil des Untersuchungsgebietes, erstrecktsich ein Bereich hohen Widerstands, der Permischen Graniten entspricht. Dieser mit hohen Körperwiderstand wird als Westgrenze des Sipoholon Geothermie-Systems interpretiert.

Zusammenfassend zeigen die Leitfähigkeitsmodelle aus dieser Studie bisher unbekannte Fluidwege des nicht vulkanischen Geothermie-Systems Sipoholon. Diese Interpretation ist konsistent mit hohen Porosität der Gesteinsproben an der Oberfläche und der Verteilung von niedriger Vp und hoher Vp/Vs, welche rund um die heißen Panabungan Quellen auftretten. In Kombination mit anderen geowissenschaftlichen Disziplinen, bietet die MT ein sehr leistungsfähiges Werkzeug für Geothermie wegen ihrer Sensitivität gegenüber heißen salzhaltigen Fluiden als Zonen hoher Leitfähigkeit.

Abstrak

Sistem panas bumi Sipoholon terletak di sekitar lembah Tarutung, bagian dari sistem patahan Sumatra. Delapan belas (18) mata air panas di sekitar Sipoholon mengindikasikan adanya fluida panas di bawah permukaan. Fluida panas di dalam pori batuan menaikkan nilai kondutifitas. Sehingga, model konduktivitas listrik dapat dianalisa berdasarkan hubungan antara resistivitas dengan porositas, konduktivitas fluida, dan suhu.

Penelitian tentang magnetotellurik (MT) ini menghasilkan peta distribusi konduktivitas bawah permukaan di daerah Sipoholon, yang dapat diinterpretasi sebagai unit batuan, termasuk kemungkinan jalan fluida di bawah permukaan. Tujuan utama penelitian ini adalah untuk mengembangkan model konseptual sistem panas bumi Sipoholon berdasarkan distribusi konduktivitas bawah permukaan. Bersama dengan penelitian lain, seperti penelitian geologi, geokimia, dan seismologi; hasil penelitian MT menyajikan pemahaman konprehensif tentang sistem panas bumi Sipoholon, terutama mengenai reservoar dan sumber panasnya.

Hasil pemodelan dua dimensi (2-D) dan tiga dimensi (3-D) dari data MT menunjukkan sebuah anomali konduktif vertikal yang terletak sekitar 6 km ke arah timur dari lembah Tarutung. Anomali konduktif ini berada di dekat lokasi patahan Panabungan dan lokasi mata air panas Panabungan. Pada kedalaman kurang dari 3 km, anomali konduktif tersebut disebabkan oleh pergerakan air meteorik dan air magmatik dari bawah ke atas permukaan. Pada kedalaman 1 km sampai 2 km, anomali konduktif ini menunjukkan resistivitas 2 Ωm, yang menunjukkan lokasi reservoar.

Di bawah reservoar, konduktor vertikal ini diinterpretasikan sebagai sirkulasi fluida panas yang memanaskan reservoar. Sirkulasi fluida panas tersebut dapat disebabkan oleh pergerakan air magmatik yang berhubungan dengan proses subduksi, namun bukan berupa pergerakan magma atau dapur magma. Interpretasi ini sesuai dengan hasil penelitian geokimia terhadap sampel air dari mata air panas Panabungan yang mengindikasikan fluida magmatik.

Sekitar 2 km ke arah barat daya dari lembah Tarutung, sebuah anomali konduktif dangkal muncul

pada kedalaman 0.5-2 km, di bawah lokasi mata air panas, di dekat lokasi gunung Martimbang. Konduktor dangkal ini diinterpretasikan sebagai material Andesitik yang teralterasi oleh suhu tinggi ketika intrusi magma Martimbang terjadi. Penelitian geofisika dan geokimia, termasuk MT, tidak menemukan indikasi bahwa Martimbang merupakan sumber panas dangkal dari sistem panas bumi Sipoholon.

Anomali konduktor dangkal lain yang muncul berada di bawah lembah Tarutung, yang diinterpretasikan sebagai sedimen lepas dari batuan vulkanik, termasuk Tuff muda Toba. Di daerah barat dari lokasi penelitian terdapat anomali resistivitas tinggi yang terletak di sekitar lokasi batuan granit berumur Permian. Resistor ini diinterpretasikan sebagai batas barat dari sistem panas bumi Sipoholon.

Hasil pemodelan menunjukkan jalan fluida panas bawah permukaan dari sistem panas bumi Sipoholon yang terdapat di sekitar lokasi mata air panas Panabungan. Interpretasi ini sesuai dengan porositas tinggi dan distribusi Vp rendah dan Vp/Vs tinggi yang terdapat di sekitar lokasi patahan Panabungan. Bersamaan dengan penelitian lain, MT sangat berguna untuk eksplorasi panas bumi karena MT sensitif memetakan fluida panas sebagai zona konduktivitas tinggi.

Acknowledgements

This study is a great experience and would not have been possible without the support of many people. First and foremost, I would like to express my gratitude to Dr. Gerard Muñoz, who was abundantly helpful, offered invaluable discussions, advice and guidance. For a huge amount of hours he spent to improve my English.

I wish to express my sincere gratitude to PD. Dr. Oliver Ritter, my principal supervisor, for his support and guidance from the first to the last level, which enabled me to develop an understanding of the subject. I am heartily thankful for providing me an opportunity to do this project work and for all knowledge, help and discussion during my study.

I am grateful to the Center for Geological Resources (PSDG) Bandung for providing the December 2010 MT data. It gave me a unique opportunity to plan the July 2011 field campaign. Some of the data were used on the 2-D inversion. My special thanks to Muhammad Kholid, staff of the geothermal research group of the PSDG.

I would like to show my appreciation to Dr. Naser Meqbel for all his help with the parallel computations of Mod3DEM, for providing the 3-D Grid software and for invaluable discussions on the 3-D inversion results.

I owe my gratitude to Ute Weckmann for a number of suggestions and helps during my study. I would like to give special thanks to all my awesome office-mates; Dr. Kristina Tietze for the proof reading and the MATLAB script, Dr. Dirk Brandlein also for the MATLAB script and Jaime Araya for sharing literatures and discussions.

I am indebted to my many of my present and former colleagues in the Geo-Electromagnetics working group (MT-AG) at GFZ and at Free University Berlin (Dr. Heinrich Brasse) for creating such an inspiring and friendly working atmosphere as well as all invaluable discussions during MT-AG meeting. I would like to acknowledge those who provided helpful feedback on earlier versions of this thesis, i.e. Jaime Araya, Reinhard Klose, Dr. Alexander Grayver. I would like

to thank to Walja Korolevski, who helped me polishing up the German Kurzfassung.

I am grateful to the International Center for Geothermal Research (ICGR). The Indonesia geothermal project meeting and the others international geothermal conferences gave me a great opportunity to meet and to discuss with many great geothermal scientists. My special thanks to Prof. Inga Moeck, Prof. Ernst Huenges, Prof. David Bruhn, Dr. Kemal Erbas and Dr. Fiorenza Deon.

I would like to thank to Dr. Mochammad Nukman for geological and geochemical results, for discussions during this study, particularly during Saturday lunch times. I also want to thank to Dr. Muksin for seismological results.

Danke vielmals, terimakasih banyak, thank you very much to the Sipoholon MT fieldwork Team. Manfred Schüler, Dr. Gerard Muñoz, Sissy Kütter, Stefan Rettig, Muhammad Faizal Zakaria, Muhammad Gunadi, Muhammad Kholid and Toni Rahadinata, who helped me collecting the magnetotelluric data in Sipoholon.

I want to thank to Dr. Michael Cugialy for his suggestions during the last step of my study. I would like to thank to Guntur Utomo for his patience and helps. I would like to show my deepest gratitude to my sister, my father and my mother for their supports, encouragements and continuous prayer, but no words of thanks are enough.

Sintia W. Niasari

Contents

Chapter 1

Introduction

The western part of Indonesia is formed by subduction of the Australian oceanic plate under the Eurasian continental plate. This subduction system has resulted in an active volcanic arc along Sumatra, Java and Celebes islands. Along this volcanic arc, there are more than 200 locations that can be considered as potential geothermal fields (Hochstein and Sudarman, 2008). These geothermal fields are associated with geothermal surface manifestations, such as hot springs, fumaroles, travertine deposits, etc. (Hochstein and Sudarman, 2008). Based on geo-thermometer data, the total geothermal resources of Indonesia have been estimated as 27 GW (Darma et al., 2010; Munandar and Widodo, 2013). As of 2009, only 20 volcanic geothermal fields have been drilled, confirming a total of proven resources up to 2 GW (Darma et al., 2010). There is a lot of unused geothermal potential in Indonesia, particularly the non-volcanic fields.

A geothermal system is a localized geological setting where the Earth's thermal energy can be used directly, e.g. spa, agricultural heating or indirectly for electric power generation (Williams et al., 2011). Geothermal systems can be classified as volcanic and non-volcanic geothermal systems. In Indonesia, volcanic geothermal systems are typically hosted by Quaternary volcanic rocks and associated with shallow igneous intrusions as the heat sources (Hochstein and Sudarman, 2008). Figure 1.1 shows a conceptual model of a volcanic geothermal system, consisting of a magmatic intrusion as heat source, a reservoir rock, a clay cap, a fault system, geothermal manifestations (such as a hot spring and a fumarole), and rainfall as recharge water. A shallow magmatic intrusive body heats up the cold water in the reservoir rocks bordered by impermeable rocks or faults. Then, thermal buoyancy causes the water to flow upward through permeable faults.

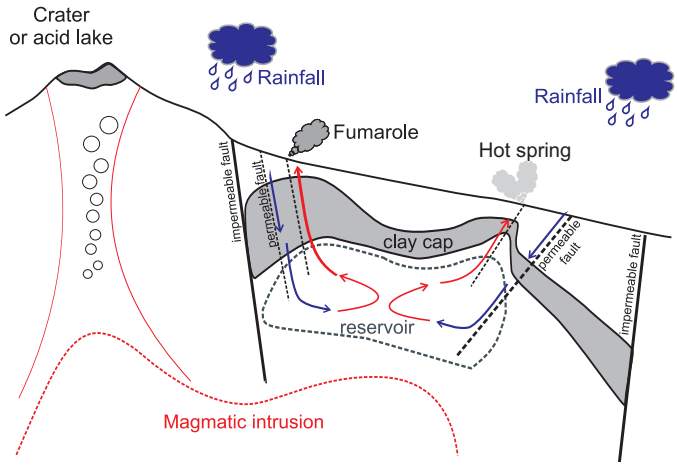

Figure 1.1: Conceptual model of a volcanic geothermal system. The cold meteoric water flows into reservoir rocks through permeable faults. A shallow magmatic intrusive body heats up the cold water in the reservoir rocks. Both impermeable clay cap and faults are needed for optimal thermal insulation of the reservoir. Then, thermal buoyancy causes the water flow upward through permeable faults as surface thermal manifestations, such as hot springs (modified from Cumming, 2009; Williams et al., 2011).

Non-volcanic geothermal systems usually show a more complex character. It is difficult to construct a conceptual model for a whole range of non-volcanic geothermal systems (Muñoz, 2013). Tamanyu and Sakaguchi (2003) simplify the classification of non-volcanic geothermal systems for Japan into two types of areas. The first type of geothermal areas occurs in sedimentary basins with deep-seated hot water resources. These deep-seated sedimentary basin systems contain hot interstitial fluids, commonly brine, locked in deep sedimentary rocks and are under lithostatic pressure from the overlying sediments. An example of these systems is the Groß Schönebeck test site in Germany (Muñoz et al., 2010). The second type of geothermal areas occurs in rough topography or mountain areas which can be associated with deep water circulation along faults or intrusive bodies (Tamanyu and Sakaguchi, 2003). Infiltrated meteoric water is collected within permeable zones and then heated up by a hot deep water circulation which is in contact with a heat source (Tamanyu and Sakaguchi, 2003).

In a geothermal system, bulk electrical conductivity of geothermal rocks, such as the reservoir rocks, depend on alteration mineral type (if any), porosity, fluid conductivity, and temperature (Caldwell et al., 1986; Ussher et al., 2000; Flovenz et al., 2005). Particular alteration minerals, such as illite and chloride, correspond to high resistivity, while other minerals, such as smectite and zeolite, correspond to low resistivity. High salinity of fluids in geothermal reservoirs increase fluid conductivity resulting an increase of the bulk conductivity of geothermal reservoirs

(Caldwell et al., 1986). Together with this, increased temperature (up to $350\,^{\circ}\mathrm{C}$) brings in higher bulk conductivity (Flovenz et al., 2005). Hence, a geophysical method which is suitable to image electrically conductive zone such as magnetotellurics (MT), is used widely for geothermal exploration (Manzella et al., 2010).

Magnetotellurics is a passive electromagnetic method which uses electric and magnetic fields variations of natural origin (Vozoff, 1990). The relation between electric and magnetic fields as a function of period is related to the subsurface electrical conductivity distribution (the inverse of electric conductivity is electric resistivity $\rho = 1/\sigma$) (Tikhonov, 1950; Cagniard, 1953). This method is able to image the subsurface resistivity from several tens of meters to hundreds of kilometers depth, depending on the survey set up, the conductivity of the survey area, and the period of the signals (e.g. Berktold, 1983; Manzella et al., 2010).

An example of the MT application for non-volcanic geothermal exploration is the subsurface resistivity mapping of the Soultz-sous-Forêts geothermal field, France (Geiermann and Schill, 2010). The geothermal field has been well studied for 20 years and has been producing 1.5 MW since June 2008 (Giroud et al., 2012). The reservoir of the Soultz-sous-Forêts field is located in a low permeable granite but has high heat flow (Geiermann and Schill, 2010). The authors have mapped a resistive zone corresponding to low permeable granite and a conductive anomaly coinciding with the location of permeable normal faults (Geiermann and Schill, 2010). A production well was drilled down to a depth of 3.6 km through sub-vertical faults and a shallow reservoir at 1.8 km (Giroud et al., 2012). This depth is in good agreement with the depth of the conductive anomaly imaged from MT, i.e. a depth of 2 km.

The Sipoholon geothermal field is characterized by 18 hot springs and 5 travertine deposits. A few of the hot springs are already used for bathing (or spa) and the travertine deposits are mined. The geothermal field is located inside and outside of the Tarutung basin, which is part of the NW-SE Sumatra fault system. The Tarutung basin is a pull-apart basin bounded by high angle normal faults and is part of a negative flower structure (Katili, 1975; Bellier and Sebrier, 1995). A negative flower structure is a set of parallel normal and vertical strike-slip faults due to trans-tensional stress regime. Nukman (2014) speculates that these faults merge with the Sumatra fault beneath the Tarutung basin.

Most of the hot springs in the Sipoholon area coincide with the location of high angle normal faults, including the northern and southern boundary faults of the Tarutung basin (Nukman, 2014). The northern boundary fault of the basin exhibits up to 40 cm wide open fractures and is located close to the Ria-ria hot spring (Nukman and Moeck, 2013). The southern boundary fault of the Tarutung basin is also situated close to a hot spring (Nukman, 2014).

Approximately 5 km to the east of the Tarutung basin, the Panabungan (PNB) hot spring occurs close to a NW-SE high angle normal fault, which is parallel to the Sumatra fault direction (Nukman and Moeck, 2013). Based on structural geology study, Nukman and Moeck (2013) suggest that the eastern side of the Tarutung Basin is controlled by extensional regime, indicated by NW-SE active extensional fractures, e.g. the PNB fault. Additionally, from geochemical analyses, the hot springs in the eastern side of the Tarutung Basin, i.e. the PNB and the Ria-ria hot springs, indicate magmatic water origin Nukman (2014). Hence, the author suggests that these extensional fractures act as fluid path ways.

Around the Ria-ria hot spring, low magnetic and Bouguer anomalies are imaged (Situmorang, 2005; Djudjun, 2005). These anomalies are interpreted as hydrothermal alteration zones due to hot fluids along the normal fault close to the Ria-ria hot spring. Similarly, low Vp and high Vp/Vs anomalies are mapped beneath the Ria-ria and the PNB hot springs (Muksin et al., 2013). The authors interpret the anomalies as high fluid content in porous media.

The Sipoholon geothermal field is located between two inactive volcanoes (the Imun volcano to the north of the Tarutung basin and the Martimbang volcano to the south of the Tarutung basin). Martimbang has been proposed as the heat source for the Sipoholon geothermal field (Hasan et al., 2005). However, the existing geophysical and geochemical data do not fully support this hypothesis (Djudjun, 2005; Situmorang, 2005; Nukman and Moeck, 2013; Muksin et al., 2013). Djudjun (2005) and Situmorang (2005) do not find any indication of a geothermal heat source, i.e. high magnetic and Bouguer anomalies, beneath the inactive Martimbang volcano.

Typical surface manifestations of volcanic systems in Indonesia (e.g. fumaroles, acid surface alteration) are absent in the Sipoholon area (Hochstein and Sudarman, 1993, 2008). Hence, the authors identify the Sipoholon geothermal system as a non-volcanic system. However, it is still unknown how this geothermal system works. Particularly, the heat source of this geothermal system is still debated.

This study presents the MT application for exploration of the non-volcanic Sipoholon geothermal field. The study area is in a populated region where high-voltage networks exist, generating electromagnetic noise which affects the natural signals. This means that filtering and remote reference techniques are needed to improve data quality before inversion of the MT data.

2-D and 3-D inversions were performed to image the electrical conductivity distribution in the Sipoholon area. This includes a number of tests using different parameters, i.e. smoothing value, data weighting, etc. The main aim of this study is to derive a conceptual model of the Sipoholon geothermal system, which is based on the conductivity distribution combined with the results of other geological, geochemical and geophysical studies.

Chapter 2

Magnetotelluric Method for Geothermal Exploration

The magnetotelluric (MT) method has been used for geothermal exploration since 1970s. For example, Lubimova et al. (1972) imaged high electric conductivity zones at 22-23.5 km depths using magnetotelluric sounding around the Baikal Lake. This conductor corresponds to a high heat flow anomaly and was interpreted as a heat source related to Baikal rift zone (Lubimova et al., 1972). Nowadays, the MT method is used widely in geothermal exploration (e.g Anderson et al., 2000). The MT inversion models represent the subsurface conductivity distribution which correlates to the various parts of the geothermal system (e.g Ussher et al., 2000; Manzella et al., 2010; Muñoz, 2013). For example, a conductive anomaly, which is a favorable target for magnetotelluric imaging, correspond to a shallow permeable and fluid-saturated reservoir of the Travale geothermal field in Italy (Manzella et al., 2010).

2.1 Geothermal system overview

"A geothermal system is any zone where portions of the Earth's thermal energy may be extracted and transported to a point of use" (Williams et al., 2011). Figure 2.1 displays a general geothermal system conceptual model, consisting of a heat source, a reservoir, fluid paths, rainfall as recharge water, and impermeable rocks (e.g. a clay cap) as borders. The heat source is the only geothermal element that has to be natural, while the other elements can be artificial (called EGS - Enhanced Geothermal System). The heat source of a geothermal system warms up the fluid in the permeable reservoir rocks. The permeability of the reservoir rocks can be natural or

can be created by permeability enhancement of the reservoir rocks. The recharge water and the fluid paths also can be natural, e.g. rain water or sea water flow in the permeable faults, or it can be artificial, e.g. by fluid injection in wells. Impermeable rocks or faults border a geothermal system, so that the hot water circulation is confined to the reservoir zone.

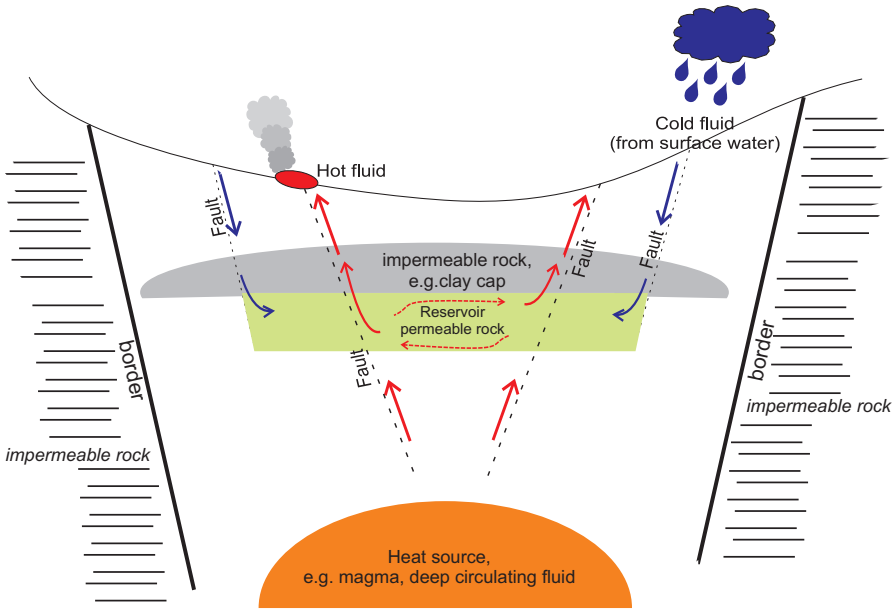

Figure 2.1: General geothermal system conceptual model. Cold meteoric water flows into reservoir rocks through permeable faults. The heat source heats up the fluid in the reservoir. And then, the hot fluids flow upward along permeable faults into the surface as geothermal manifestation, such as hot springs (modified from Berktold, 1983).

Heat source

Based on the type of the heat source, geothermal systems can be classified as volcanic or non-volcanic geothermal system (Hochstein and Sudarman, 1993). For a volcanic geothermal system, especially in Indonesia, the heat source is a shallow hot intrusion which is associated with an active or recent volcano (Hochstein and Sudarman, 1993). Typical surface manifestations are high temperature fumaroles, a vent around a volcano from which hot steam is emitted. The hot steam emitted at surface can have temperatures $\geq 100\,^{\circ}\mathrm{C}$.

The heat source for non-volcanic geothermal system can be a geothermal gradient in sedimentary rocks, deep water circulation, or an old granitic intrusion. The normal average geothermal gradient is about $3\,^{\circ}\mathrm{C}/100$ m (Fridleifsson et al., 2008). If we assume that the annual average surface temperature is $15\,^{\circ}\mathrm{C}$, the temperature at 3 km depth is $105\,^{\circ}\mathrm{C}$. The Kamikita geothermal system is an example of a geothermal system having a geothermal gradient in sedimentary rocks,

while the Izura hot spring, in Tohoku, Japan is an example of a geothermal system with deep water circulation along permeable fault zone (Tamanyu and Sakaguchi, 2003). The Noto Peninsula geothermal system, Japan is an example of a geothermal system with a heat source from an old granitic intrusion (Umeda et al., 2009). The old granitic intrusion warms up fluids in the reservoir through radiation of Th, U, and K from the granite.

Reservoir

In the geothermal reservoir, hot fluids are accumulated in permeable rocks. The hot fluid accumulation can be dominated by liquid ($\geq 60\%$ water), by vapor ($\geq 60\%$ vapor), or be a mixed system (50% water and 50% vapor). The vapor dominated reservoirs are generally associated with volcanic geothermal systems and high reservoir temperatures ($\geq 200\,^{\circ}\mathrm{C}$), while liquid dominated reservoirs can be correlated with either low or high temperature reservoirs (Williams et al., 2011).

Geothermal classification based on reservoir temperatures originated from the 1980s for assessment and providing a framework for the exploitation method of the geothermal resources. Hochstein (1988) classified low temperature geothermal reservoirs with T$\leq 125\,^{\circ}\mathrm{C}$ as a lower temperature limit for electric generation. Later, Lund and Bloomquist (2012) scaled down the lower limit of the reservoir temperature to $100\,^{\circ}\mathrm{C}$ as a result of technology development of power plant, such as the separators, the turbines, etc.

Permeability structures

Fractures or faults can act as fluid paths both for the cold water inflow from the surface to the reservoir (recharges) and for the hot water up-flow to the surface, e.g. as hot springs or geysers (see Figure 2.1). These structures are important for geothermal exploration because they indicate the possible location of hot fluid accumulation in permeable areas. Hot springs are found commonly in fault intersections where active fracturing creates permeable pathways (Curewitz and Karson, 1997). When two faults or more interact, stress is concentrated on the fault plane intersection. This concentrating stresses propagate fracturing that maintains the porosity and permeability. The hydrothermal cycle keeps on going - the cold fluids flow into the reservoir, the fluids are heated up in the reservoir, the hot fluids flow up to the surface.

Fractures or faults create the secondary porosity due to dissolution or fracturing processes. The secondary porosity produces more pore space for fluid conduits. As mentioned before, in EGS where the primary porosity is low, permeability enhancement is used to create secondary porosity to increase the bulk porosity.

Spatial extend

The spatial extend of a geothermal system are usually bordered by impermeable rocks, mineral alteration zone or sealed faults (Berktold, 1983; Cumming, 2009). Mineral alteration is the change from a primary mineral to a secondary mineral due to temperature, pressure, or chemical condition changes. An example of this mineral alteration is smectite. In a geothermal system, a smectite layer is commonly referred as the clay cap. Smectite is an alteration product of volcanic rocks and is characterized for its fine grain size, low permeability, and high water absorption (Vrolijk, 1990). Smectites are distributed horizontally and follow the temperature distribution (Cathelineau et al., 1983). Smectite occurrences follow horizontally the isotherm $70 - 200\,^{\circ}\mathrm{C}$ (Ussher et al., 2000). These clay caps prevent the fluid flow and keep the fluid accumulated in the reservoir (see Figure 2.1).

In contrast with smectite, silica precipitates on open space fractures or along vertical faults. This silica precipitation creates a sealed fault or impermeable zone. As a result, the fluid flow is prevented due to decreasing porosity and permeability along faults (Curewitz and Karson, 1997).

Recharge water

The geothermal recharge water is the cold water from the Earth's surface which flows into the reservoir. Mostly, the recharge water is of meteoric origin. However, there is also artificial recharge through injection wells using sea water or other type of fluids. This geothermal system element is important for keeping the cycle or maintaining the geothermal field "renewable".

2.2 Electrical conductivity of rocks

Electrical conductivity (σ) or electrical resistivity (ρ=1/σ) describes the transport of electric charges in materials. There have been a number of studies of the electrical conductivity of rocks since the 1940s (e.g Archie, 1942). Those studies are important to understand the properties and the mechanism of the electrical conductivity.

Caldwell et al. (1986) categorize the conduction mechanisms in the earth into three types: metallic conduction, electronic conduction and ionic conduction. Metallic conduction occurs due to the mobility of free electrons in pure metals, which are very rare in the crust (Karato and Wang, 2013). Electronic conduction occurs in minerals. The charge carriers in electronic conduction are electrons. A typical silicate minerals in dry condition, such as olivine (Fe_2SiO_4 or Mg_2SiO_4), is an example in which the conduction is mainly due to the migration of electrons (Karato and Wang, 2013).

The other electrical conductivity mechanism is ionic conduction, when the electric charges are carried by ions. This mechanism occurs when hydrogen (water or fluids) is present because the high mobility of hydrogen ions (Karato and Wang, 2013). If the rock pores are filled by fluids, such as in geothermal area, ionic conduction mechanism dominates the conduction mechanism in the rocks (Hersir and Arnason, 2012). This ionic mechanism can be divided into three types (see Figure 2.2).

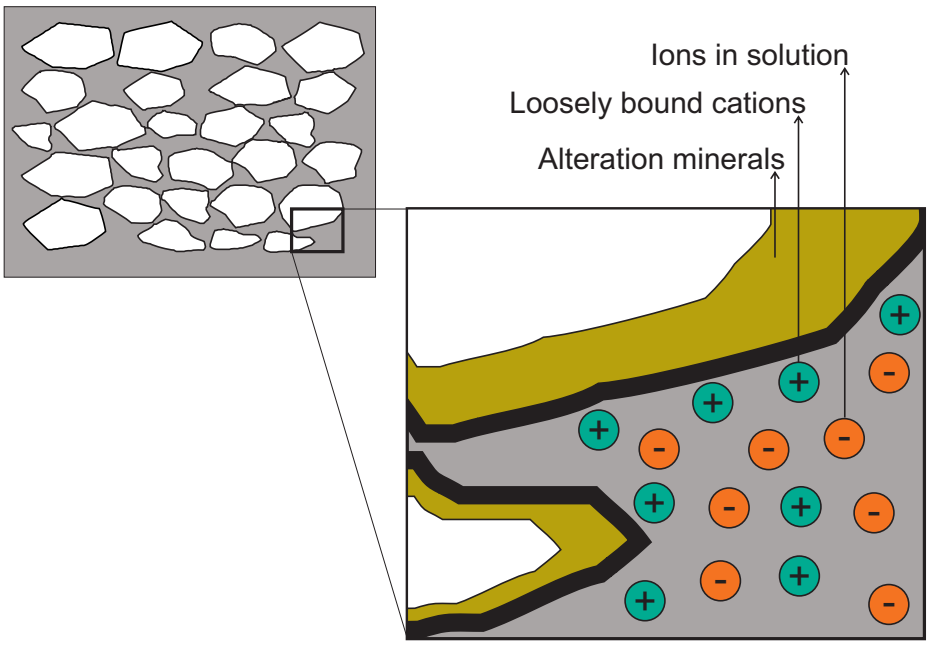

Figure 2.2: A typical sedimentary rock consists of pores (grey) and mineral grains (white). In geothermal area, pores are filled by saline fluids. The ionic conduction mechanisms can be due to pore fluid conduction, surface conduction, or mineral conduction (modified from Hersir and Arnason, 2012).

- **Pore fluid conduction**
  Pore fluid conduction is the conduction by dissolved ions in the pore fluid (Hersir and Arnason, 2012andKarato and Wang, 2013). The bulk electrical conductivity of rock increases when the rock pores are filled by fluid, due to the mobility of ions (Karato and Wang, 2013). Increasing salinity promotes higher conductivity because of the enhancement of ion mobility (Ussher et al., 2000).

- **Surface conduction**
  Surface conduction is due to the absorbed ions on the pore surface. Alteration mineral

rocks contain negative charges in the clay particles, which causes an excess of cations in the clay surfaces (Flovenz et al., 2005). The number of the negative charges is commonly called the cation exchange capacity (CEC). An example of mineral alteration that has high CEC is smectite. Smectite has a CEC of 1.5 meq/g. Thus, in smectite, this surface conduction dominates the conductivity mechanism (Flovenz et al., 2005).

– **Mineral conduction**
Mineral conduction occurs by ion transport within the mineral. The chemical composition of minerals determines the value of the conductivity (Karato and Wang, 2013). Minerals formed by the cations Al^{3+}, Mg^{2+} are characterized by high resistivity, whereas minerals containing the cations K^{+}, Na^{+}, such as mineral halite (NaCl) have small resistivity.

The bulk electrical resistivity of a porous (sedimentary) rock (ρ) in oil and gas reservoirs is a function of pore fluid resistivity (ρ_w), porosity (ϕ), and water saturation (S_w) :

$$\rho = a\ \rho_w\ \phi^{-m}\ S_w^{-n} \tag{2.1}$$

where *a* and *n* are constants which depend on the porosity type (Archie, 1942). The exponent *m* is commonly called cementation factor which depends on the degree of formation compaction and lithology (Archie, 1942). *m* had been found empirically to a range 1.8 - 2.0 for consolidated sandstone, while the cementation factor of unconsolidated sandstone was 1.2 (Archie, 1942). The equation represents the resistivity of sandstones under ideal conditions, such as uniform sand.

Electrical resistivity of rocks in geothermal system

In a geothermal environment, the rock resistivities differs from the oil reservoir described by Archie (1942) (e.g Caldwell et al., 1986; Ussher et al., 2000). Variables which affect the resistivity of rocks in geothermal system are not only the porosity, water resistivity, and water saturation, but also the temperature, salinity, and alteration minerals (if any). When clays are present, Archie's equation will underestimate the bulk resistivity of rocks (Caldwell et al., 1986).

Caldwell et al. (1986) performed laboratory resistivity measurements of core samples taken from geothermal fields in New Zealand and Philippines. The authors find that the amount of alteration minerals, commonly called clay minerals, strongly influence the bulk conductivity. Increasing 10% clay content in the rock samples decreases the conductivity by one order of magnitude (Caldwell et al., 1986). Thus, a modification of Archie's law can be written as:

$$\rho = a\ \rho_w\ \phi^{-m} S_w^{-n}\ (1 + KC\rho_w)^{-1} \tag{2.2}$$

where K is constant depends on the type of the clay mineral and C is the proportion of the clay minerals in the matrix (Caldwell et al., 1986). Some minerals, such as smectite, montmorilonite, and zeolite, have high K value (≥ 100), indicating loosely bound cations (Ussher et al., 2000). Thus, these minerals have low resistivity because the cations can move easily. Other minerals, such as illite and chlorite, have low K value (≤ 50), due to strong crystal ion bounds.

An inverse exponential dependence of resistivity with temperature is:

$$\rho = \rho_0 \, e^{\varepsilon/RT} \tag{2.3}$$

where ρ_0 is resistivity at initial (room) temperature, ε is activation energy, R is Boltzman's constant, and T is temperature ($^\circ$K) (e.g Caldwell et al., 1986; Llera et al., 1990; Ussher et al., 2000). ε is an empirical parameter wherein some resistivity measurements of a sample at a range of temperatures is needed.

At temperatures $\leq 200\,^\circ$C, the fluid resistivity decreases with increasing temperature, because of the enhanced ion mobility (Llera et al., 1990). On the other hand, at temperatures $\geq 300\,^\circ$C, increasing temperature of the water results in dissociated ions that increase the fluid resistivity (Quist and Marshall, 1968). Thus, in vapor dominated geothermal systems, such as Lardarello which has reservoir temperature between $300 - 350\,^\circ$C, the reservoirs do not correspond to low resistivity. However, Caldwell et al. (1986) find that in geothermal rocks conductivity, temperature was a lesser factor compare to the clay content, the fluid conductivity and porosity.

The clay alteration types associate with temperature (e.g Caldwell et al., 1986; Ussher et al., 2000). Particular clay minerals are only formed in certain temperature ranges. Zeolites and smectite are formed at low temperatures ($\leq 200\,^\circ$C), chlorite is formed at temperatures of $220 - 250\,^\circ$C, and epidote is formed at even higher temperatures ($260 - 300\,^\circ$C) (Ussher et al., 2000). The smectite or zeolites layers correlate with lower electrical resistivity compared to chlorites which have been confirmed by resistivity well logs and MT inversion models (Ussher et al., 2000). These smectite low resistivity layers are often interpreted as clay cap covering the geothermal reservoir zone (Hersir and Arnason, 2012).

After the clay content, the second factor affecting the conductivity in geothermal rocks is a combination of the fluid conductivity and porosity (Caldwell et al., 1986). Several laboratory measurements show that increasing one magnitude in porosity (such as increasing porosity (ϕ) from 0.02 to 0.2) resulting approximately one magnitude higher of bulk conductivity (e.g Caldwell et al., 1986; Ussher et al., 2000; Hersir and Arnason, 2012). When the fluids have high salinity, it causes higher fluids electrical conductivity because of enhanced ion mobility (e.g Ucok et al.,

1980; Caldwell et al., 1986). Increasing one magnitude of salinity (such as from 10^5 to 10^6 ppm NaCl) yields one magnitude higher of the fluid conductivity (Ucok et al., 1980), which resulting almost one magnitude higher of the bulk conductivity (Hersir and Arnason, 2012).

Hence, in low to moderate temperature geothermal systems, mixture of (relatively) hot and saline fluids in permeable host rocks result high conductivity. These high conductivity anomalies can be imaged with magnetotellurics (e.g. Manzella et al., 2010; Muñoz, 2013).

2.3 Magnetotelluric basic theory

Magnetotellurics (MT) is an electromagnetic method which uses naturally occurring electromagnetic (EM) field variations as sources (Tikhonov, 1950; Cagniard, 1953). The frequency range of the natural electromagnetic fields are generally between 10^{-4} Hz to 10^4 Hz (Vozoff, 1990). The natural signals at frequency above 1 Hz originate from the global lightning discharges, while the natural signals at frequency below 1 Hz come from the complex interaction between Earth's magnetic field and solar plasma (Vozoff, 1990). These natural signals have low energies between 0.1 and 10 Hz. This frequency band, between 0.1 and 10 Hz, is commonly called dead band.

From the point of view of Maxwell equations, the horizontal electric and magnetic fields are related to each other Tikhonov (1950) and Cagniard (1953). They found that the impedance *Z*, which is the ratio of electric (**E**) and magnetic (**H**) fields, correlates to the electrical resistivity (ρ) of the Earth's. When a plane wave vertically incident on the Earth's surface, the electric (**E**) and magnetic (**H**) fields are perpendicular and are constant in direction Tikhonov (1950) and Cagniard (1953). Hence:

$$Z = \frac{E_x}{H_y} = -\frac{E_y}{H_x} \tag{2.4}$$

where x and y directed northwards and eastwards respectively.

The resistivity of the subsurface and the phase can be written as:

$$\rho = \frac{|Z|^2}{\omega \mu_0} \tag{2.5}$$

$$\phi(\omega) = \arctan \frac{Im\,[Z]}{Re\,[Z]} \tag{2.6}$$

where $\omega = 2\pi f$, μ_0 is the magnetic permittivity.

One-Dimensional Earth

In the initial studies of Tikhonov (1950) and Cagniard (1953), it was assumed that the Earth is a one dimensional uniformly. *E/H* is independent of the direction of the coordinate axes (Vozoff, 1990). In 1D-case (see Figure 2.3), the diagonal elements of the impedance tensor are zero, while the off-diagonal elements are of the same amplitude, but with an opposed sign. In this case, the impedance *Z* can be written as:

$$\begin{bmatrix} E_x \\ E_y \end{bmatrix} = \begin{bmatrix} 0 & Z_{1D} \\ -Z_{1D} & 0 \end{bmatrix} \begin{bmatrix} H_x \\ H_y \end{bmatrix} \tag{2.7}$$

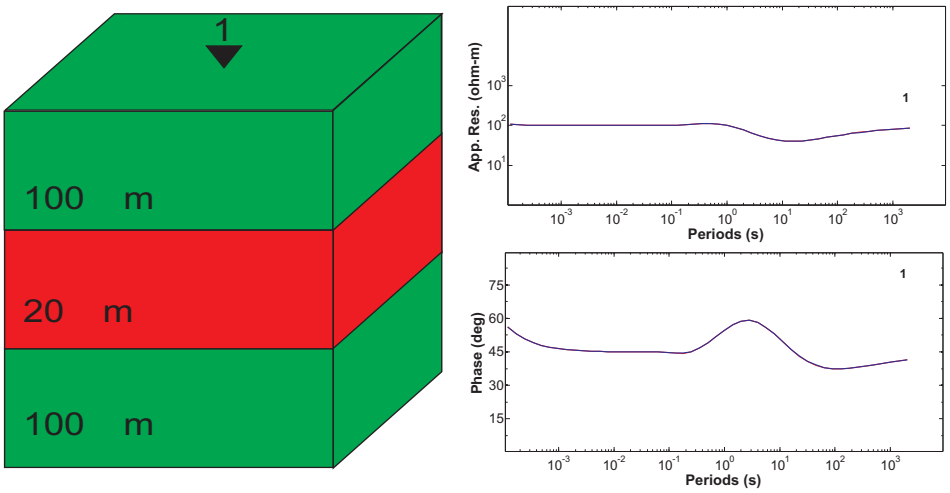

Figure 2.3: a). Left: a 1-D model, e.g. a conductive sedimentary layer between two resistive layers. b) Right: apparent resistivity and phase curves of site 1 from forward modelling response.

Two-Dimensional Earth

In the 2-D case (see Figure 2.4), the complexity increases. There are lateral conductivity interfaces in only one direction, the impedance *Z* can be written as:

$$\begin{bmatrix} E_x \\ E_y \end{bmatrix} = \begin{bmatrix} 0 & Z_{\parallel} \\ Z_{\perp} & 0 \end{bmatrix} \begin{bmatrix} H_x \\ H_y \end{bmatrix} \tag{2.8}$$

but only if the x or y direction aligned along the lateral conductivity interfaces. In this case, the total electromagnetic fields split into two independent modes, TE and TM (see Figure 2.4). In the TE (transverse electric) mode, the telluric current flows along the structure, while in the TM (transverse magnetic) mode, the electric field perpendicular to the strike.

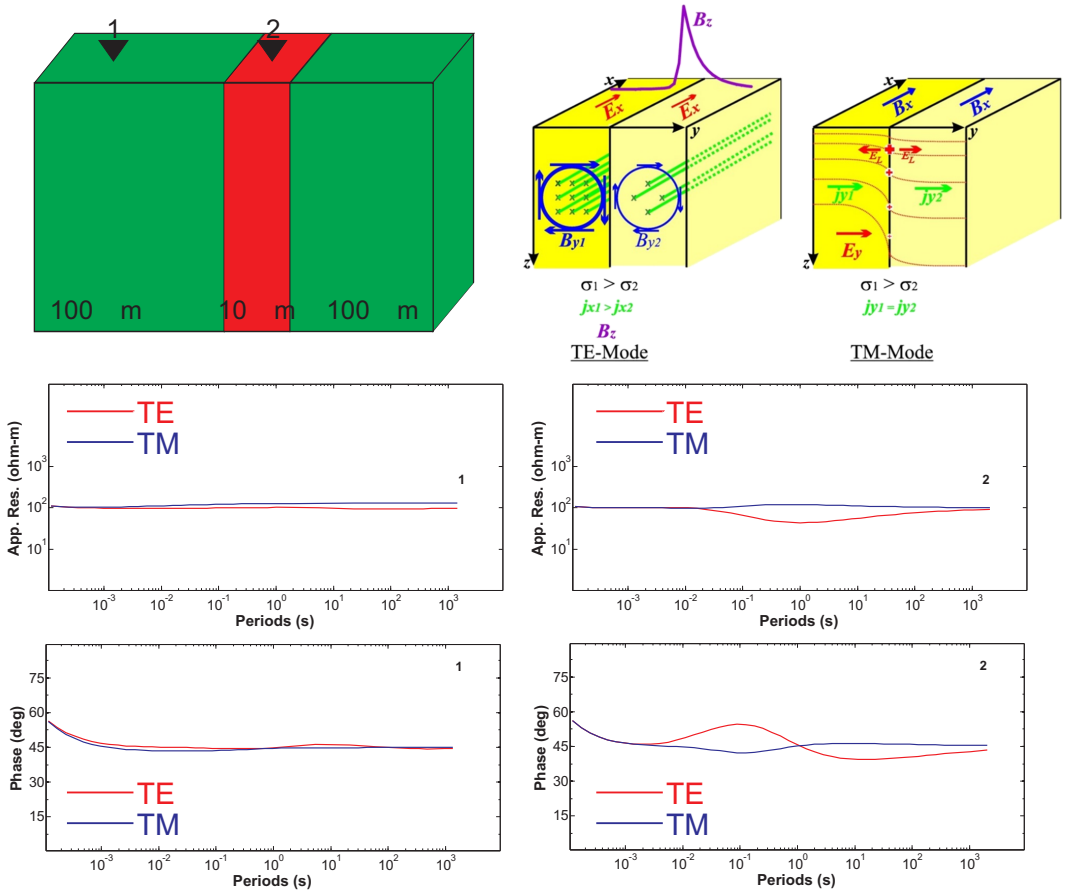

Figure 2.4: a). Upper left: a 2-D model, e.g. a conductive vertical deep fault. b). Upper right: Schematic of 2-D model of TE and TM modes (from O. Ritter (Pers. Comm.) and Hoffmann-Rothe (2002)). c). Below: apparent resistivity, phase, and VTFs curves of site 1 and 2 from forward modelling responses of 2-D model.

In TE mode, there are no boundary charges (see Figure 2.4). In TM mode, there are boundary charges on the sides of the lateral conductivity interfaces. Thus, close to the lateral conductivity interfaces, the 2-D TE and TM apparent resistivity and phase curves are different over the whole frequency range. On the other hand, away from the lateral conductivity interfaces, the 2-D TE and TM responses are quite similar.

As mentioned before, in 2D case, $Z_{xx} = Z_{yy} = 0$ is only fulfilled if the x'- or y'- axes of the measuring coordinate system are aligned with the direction of the regional 2-D structure. However, the direction of the regional 2-D structure is not always aligned with the geographical coordinates, where x-direction is northward, and y-direction is eastward. Following Bahr (1988), in any measurement (x,y) coordinate system, the measured impedance tensor (Z') can be rewritten as:

$$Z' = RAZ^r R^T \tag{2.9}$$

where R is a clockwise rotation matrix, AZ^r is the impedance tensor in the coordinate system, and the superscript T is transpose of matrix R.

These columns of the impedance tensor Z can be referred to telluric vectors, which can be represented as an ellipse (Bahr, 1988). Becken and Burkhardt (2004) showed that in the presence of a regional 2-D structure, the telluric vectors are linearly polarized (the minor axis of the ellipse is zero), but only if the impedance tensor is rotated to an angle which is parallel or perpendicular to the strike of the 2-D structure. Hence, one can rotate the impedance tensor until the minor axes of the telluric vectors are zero or close to zero and determine the strike angle over a number of periods and sites simultaneously. When these assumptions are fulfilled, 2-D inversion and interpretation can be performed.

Three-Dimensional Earth

In the 3-D case, charge accumulations at surfaces depends on shape, depth, and conductivities of the 3-D bodies. The EM fields do not decouple into TE and TM modes (Vozoff, 1990). Horizontal electric ($\vec{E}$) and magnetic ($\vec{H}$) fields are not orthogonal, thus:

$$E_x(\omega) = Z_{xx}(\omega)H_x(\omega) + Z_{xy}(\omega)H_y(\omega) \tag{2.10}$$

$$E_y(\omega) = Z_{yx}(\omega)H_x(\omega) + Z_{yy}(\omega)H_y(\omega) \tag{2.11}$$

The relationships between E and H at each frequency can be written as:

$$\begin{bmatrix} E_x \\ E_y \end{bmatrix} = \begin{bmatrix} Z_{xx} & Z_{xy} \\ Z_{yx} & Z_{yy} \end{bmatrix} \begin{bmatrix} H_x \\ H_y \end{bmatrix} \tag{2.12}$$

Vertical magnetic transfer functions

Beside the impedance, additional geo-electrical information comes from the vertical magnetic transfer functions (VTFs) (Berdichevsky and Dmitriev, 2008). VTFs relates the vertical component of the magnetic field (H_z) to its horizontal components (H_x, H_y) as:

$$H_z(\omega) = T_x(\omega)H_x(\omega) + T_y(\omega)H_y(\omega) \tag{2.13}$$

where z indicates vertical direction downwards.

The VTFs are complex numbers and frequency dependent. Hence, the VTFs can be displayed as an induction arrows of real $\vec{P}$ and imaginary $\vec{Q}$ part of T_x and T_y, for certain period:

$$\vec{P} = Re\,[T_x]\,\hat{x} + Re\,[T_y]\,\hat{y} \tag{2.14}$$

$$\vec{Q} = Im\,[T_x]\,\hat{x} + Im\,[T_y]\,\hat{y} \tag{2.15}$$

$\hat{x}$ and $\hat{y}$ denote the unit vectors in x and y direction, respectively.

In the Wiese convention (Wiese, 1962), which is used in this study, the real induction vectors *Re* **T** tend to point away from conductors. Furthermore, the induction arrows tend to be perpendicular to the geo-electric strike. Thus, the induction arrows can be used to clarify the strike direction. Note, the strike direction determined from impedance is 90 °C non-unique.

Chapter 3

Magnetotelluric study of the Sipoholon Geothermal Field

Along the Sumatra fault, there are more than 20 locations, which can be considered as potential geothermal fields (Hochstein and Sudarman, 1993). Four of these prospects are in the North Sumatra Province (Hochstein and Sudarman, 1993). Three of four prospects are volcanic geothermal system, the Sibayak, the Sarulla, and the Pusuk bukit (Hochstein and Sudarman, 2008). As of 2012, one of the Sibayak wells has been producing 12 MWe (Munandar and Widodo, 2013). Between 1994 and 1998, in the Sarulla geothermal field, thirteen wells had been drilled to a maximum depth of about 2.3 km found a maximum temperature of $310\,^{\circ}\mathrm{C}$ (Hochstein and Sudarman, 2008). However, the Sarulla geothermal field has a corrosion problem due to high acidity of the geothermal reservoir fluids. As of 2008, the Pusuk Bukit geothermal field located close to the Toba lake had not been drilled yet (Hochstein and Sudarman, 2008).

Under the framework of the Project of Sustainability concepts for the exploitation of geothermal reservoirs in Indonesia funded by BMBF, the Sipoholon geothermal field was chosen as a study area. There are three reasons: 1. this geothermal field is a green field, a geothermal field where there is no exploration well yet; 2. how this geothermal system works is still debatable; and 3. the Sipoholon geothermal field is classified as a non-volcanic geothermal system, which is in the contrary of the other three geothermal systems in the North Sumatra Province.

3.1 Geological background

The Sumatra island is located in an active continental margin where the Australian oceanic plate is subducted beneath the Eurasian continental plate (see Figure 3.1). This subduction zone continues moving slowly since the Cretaceous ($\pm$ 146 Ma) from the North-east to its present location (Katili, 1975). The subduction zone is oblique and results in strike slip deformation along 1650 km with dilatational stepovers between fault segments (Sieh and Natawidjaja, 2000). The fault segments along the Sumatra Fault System are the result of subduction rate differentiation in the north and in the south of Sumatra (Sieh and Natawidjaja, 2000). An example of these dilatational stepovers is the Tarutung basin, characterised by a collapsed zone controlled by boundary faults (Bellier and Sebrier, 1995).

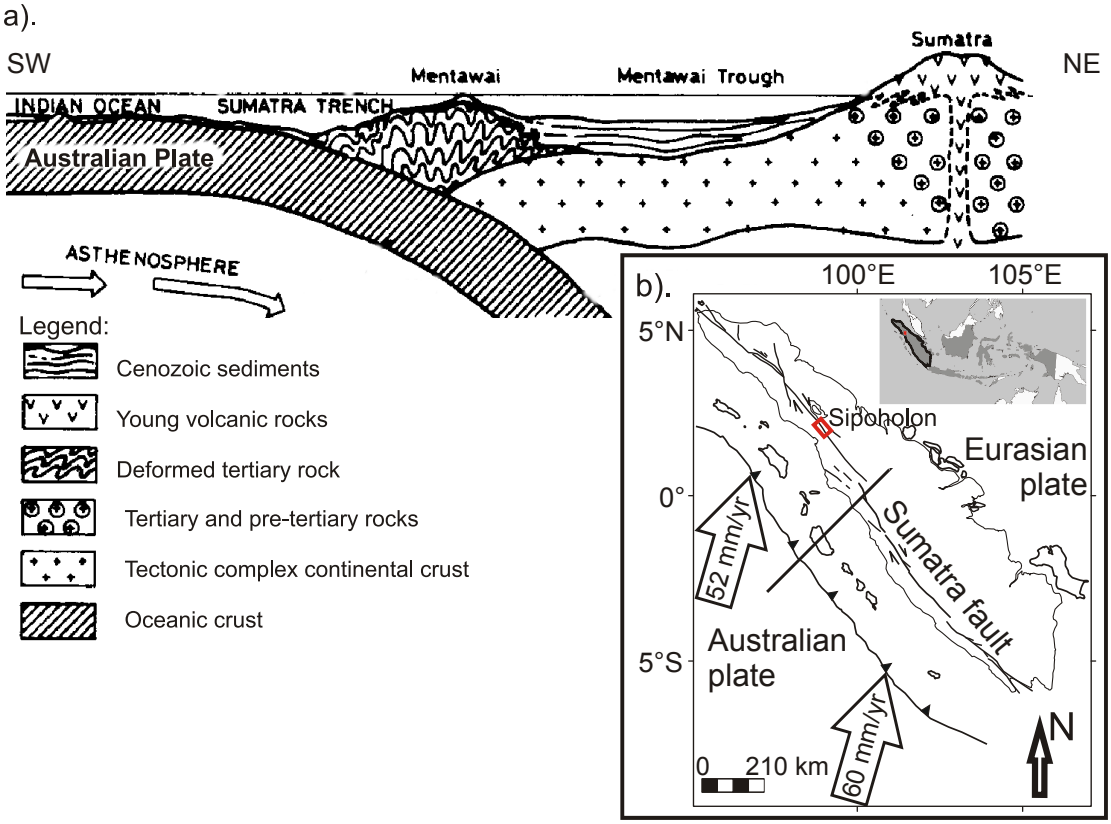

Figure 3.1: a. Schematic section across Sumatra showing the oceanic crust, the Mentawai trough, and Sumatra volcanic arc (Katili, 1975); b. Map of Sumatra showing the subduction zone and motion of the plate (indicated by arrows) (Sieh and Natawidjaja, 2000).

3.1.1 Geological structure

The Tarutung basin is bound by high angle normal faults to the NW and to the SE (see Figure 3.2) (Bellier and Sebrier, 1995; Nukman and Moeck, 2013). Another high angle normal fault is located further to the east of the Tarutung basin and coincides with the Panabungan hot spring (Nukman and Moeck, 2013). Close to the Pianor hot spring (see Figure 3.2), around 5 km to the south of the Tarutung basin, a N-S normal fault located in the travertine deposits is accompanied by 100 cm open fractures (Nukman and Moeck, 2013).

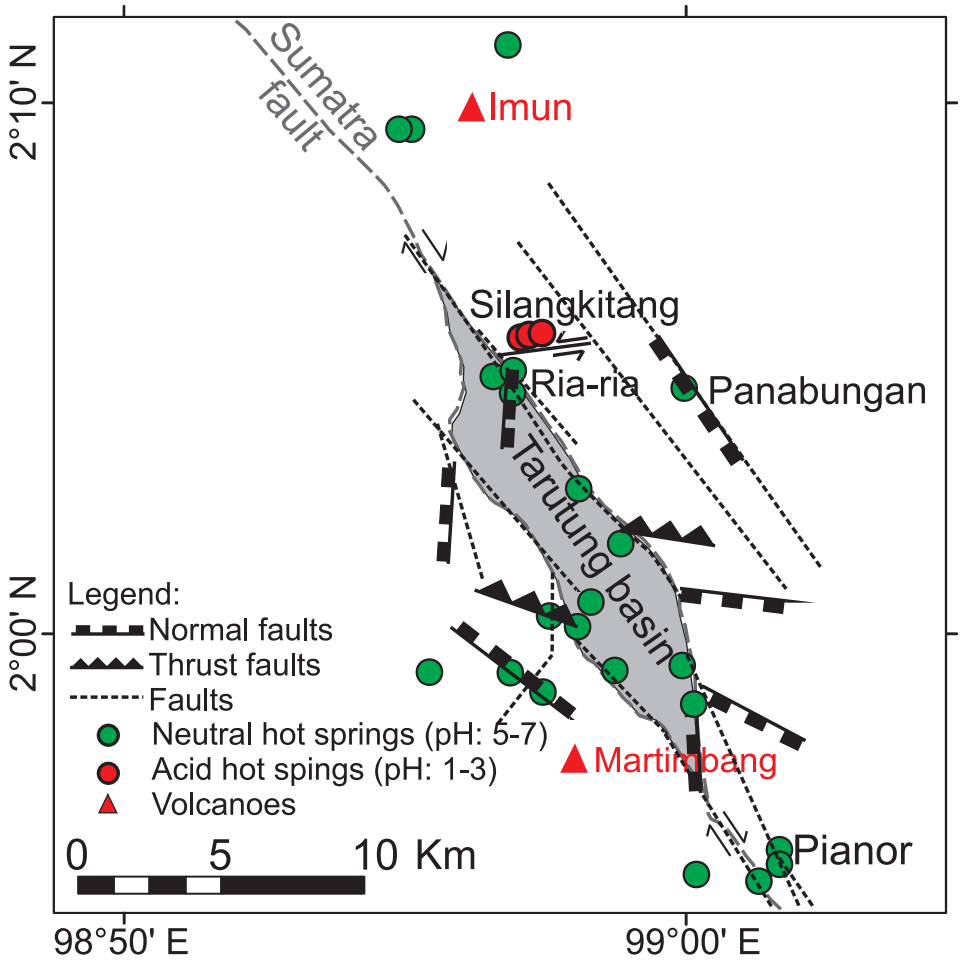

Figure 3.2: Location of hot springs (circles), inactive volcanic summits (red triangles), faults and Tarutung basin. Red circles indicate the Silangkitang acidic hot springs which are close to a sealed sinistral fault. Grey area indicates the distribution of the alluvium deposits in the Tarutung basin (modified from Nukman and Moeck (2013)).

Besides normal faults, there is a sinistral Silangkitang fault with E-W direction, dipping 88 ° NNW (Figure 3.2). This sinistral fault is an impermeable fault due to quartz sand filled and acts as a fluid barrier (Nukman and Moeck, 2013). The Silangkitang fault separates the acidic Silangkitang hot springs to the north from the neutral Ria-ria hot springs to the south (Nukman and Moeck, 2013).

Nukman and Moeck (2013) mapped a caldera like feature from SRTM (Shuttle Radar Topography Mission) interpretation in the eastern part of the study area around the Panabungan (PNB) hot spring. A caldera like feature indicates that there is a possibility of crustal intrusion or a volcanic activity in the past, which could act as the heat source of the geothermal system. This hypothesis is based on the study of Hochstein and Sudarman (1993) interpreting the heat source of the 30 geothermal systems along the active Sumatra arc being related to volcanic activity.

3.1.2 Stratigraphy

The study area consists of two continental fragments or terranes, the Western and the Eastern terranes separated by the Sumatra fault (Metcalfe, 1983; Barber and Crow, 2003; Nukman and Moeck, 2013). These continental fragments have a distinctive stratigraphy, particularly between Carboniferous age ($\pm$350 Ma) and Miocene ($\pm$23 Ma). The Tarutung basin (indicated as grey colour in Figure 3.3), located between the western and the eastern terranes, begun to develop in the middle Miocene (13 Ma).

Western terrane

The oldest rocks in the Western terrane are Carboniferous phyllitic slates consisting of oceanic assemblages (Barber and Crow, 2003). These rocks were intruded by granites in Permian time ($\pm$270 Ma) (Barber and Crow, 2003; Nukman and Moeck, 2013). The Sunda Arc volcanism, taking place since Miocene, resulted in andesitic rocks over most of the Western terrane. As the magmatism continued, local outcrops of Pleistocene ($\pm$2.6 Ma) andesite exist around the Martimbang inactive volcano. The youngest rocks in this area are the Quaternary Toba tuffs.

Eastern terrane

Basement of the Eastern terrane are Carboniferous limestones and wackes (Metcalfe, 1983). Miocene andesites are also present in this area. Pleistocene dacitic rocks occur around the Imun (inactive) volcano (Aldiss et al., 1983). Most of this area is covered by Quaternary Toba tuff, but the youngest stratigraphic units are massive Quaternary travertine deposits (Figure 3.4) which are exposed only at the eastern margin of Tarutung basin (Nukman and Moeck, 2013).

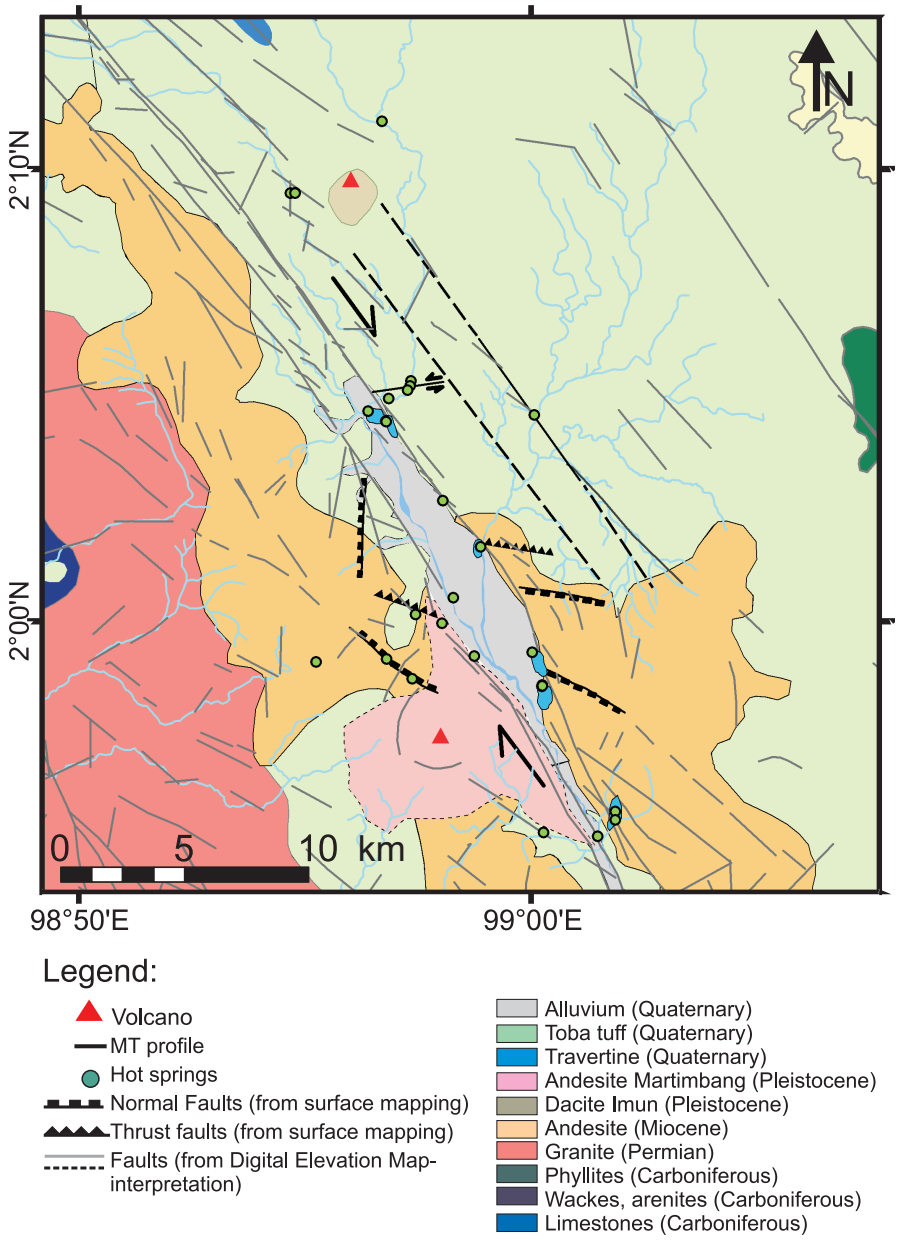

Figure 3.3: Surface geological map of the Sipoholon area showing the distribution of lithologies, faults, hot springs, and inactive volcanoes. Quaternary tuff covers most of the study area. Light brown colour is an area of Miocene andesite, which is underlain by Permian granite (modified from Nukman and Moeck, 2013).

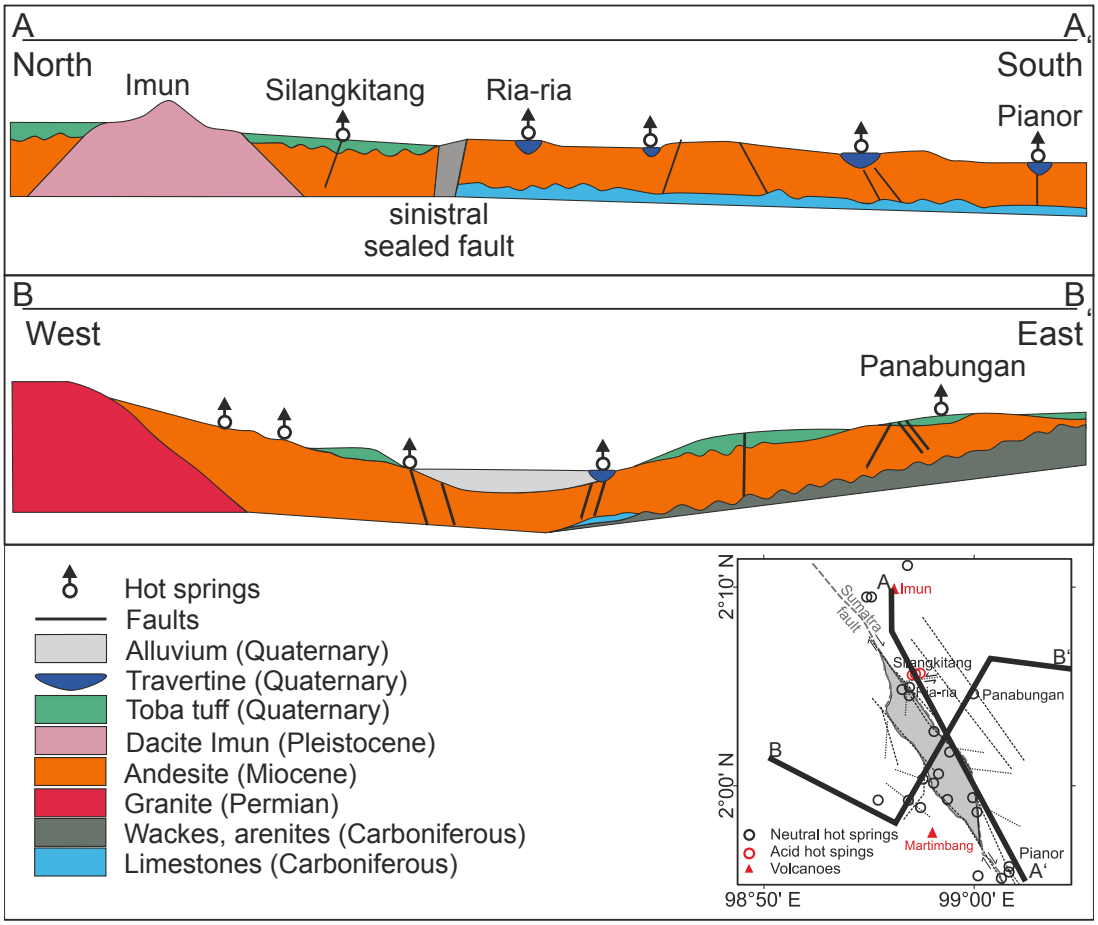

Figure 3.4: Geological cross section (unscaled) of the Sipoholon area, showing the distribution of Carboniferous to Quaternary rocks. The schematic N-S cross section (A-A') shows the travertines deposited to the south of a sealed fault. According to the E-W cross-section (B-B'), Carboniferous limestones and the travertines are only present in the eastern margin of the Tarutung basin (modified from Nukman and Moeck, 2013; Nukman, 2014).

3.1.3 Geothermal Manifestations

Geothermal manifestations (such as hot springs, travertines, fumaroles, and mud pools) indicate water flow from depth to the surface. In the study area, there are two kind of geothermal surface manifestations: hot springs and travetine deposits. There are a total of 18 hot springs located inside and outside of the Tarutung basin (see Figure 3.3). All springs occur on or close to surface traces of faults. The highest water temperature ($62\,^{\circ}\mathrm{C}$) was measured at the Ria-ria hot spring during the rainy season (Nukman and Moeck, 2013). The hot springs on the eastern area of the Tarutung basin are controlled by an extensional regime (Nukman and Moeck, 2013).

Travertines

There are six travertine deposits (see Figure 3.3), all of them located in the eastern margin of the Tarutung basin. Travertine is formed by precipitation of carbonate minerals from a supersaturated alkaline solution in ground and surface waters, and/or geothermally heated hot-springs. Travertine is an indicator that fluids must have had sufficient time to react with the carbonate rocks along a permeable zone from the depth to the surface (Hochstein and Sudarman, 1993). One of the sources of these carbonate rocks are the Carboniferous limestones, which form part of the basement of the eastern area (see Figure 3.3) (Nukman and Moeck, 2013). Thus, these travertine deposits only occur in the eastern margin of the Tarutung basin.

Neutral hot springs

Most of the springs in the Tarutung region have a neutral pH, such as the Ria-ria hot spring which is located in a large travertine terrace (Hochstein and Sudarman, 1993). Hot springs, which are located in the western area of the basin, also have neutral pH (Nukman and Moeck, 2013). There are some hot springs which are located close to the Imun and Martimbang inactive volcanoes (Nukman and Moeck, 2013). The most interesting geothermal manifestation is Panabungan hot spring, with the following characteristics:

- It has the largest discharge of water (50 kg/s, Hochstein and Sudarman, 2008) with high chloride contents and without travertine deposits (Nukman and Moeck, 2013).
- It has low δ^{18}O and high Mg content (Ardiwinata et al., 2005; Nukman and Moeck, 2013), indicating that the water contains magmatic waters from depth mixed with surface waters.
- Its location coincides with a permeable normal fault zone (Nukman and Moeck, 2013).

Acidic cold springs

The Silangkitang cold springs have acid pH ($1.2 - 2.3$) with temperatures between $22 - 28\,^{\circ}\mathrm{C}$. These cold springs occur close to a sinistral sealed fault and have significant gas bubbles (Nuk-

man and Moeck, 2013). However, based on geo-thermometry studies, Ellis and Mahon (1982) suggested that acid sulphate water is due to leaching of acid sulphate water by the surrounding rocks. These results imply that the water from the acidic springs do not originate from a deep water source, but come from chemical reaction of surface water with the surrounding rocks.

3.1.4 Existing Geophysical Studies

Since 2005, a number of geophysical studies have been carried out in the Sipoholon area. Situmorang (2005) found negative magnetic anomalies around the Ria-ria hot spring and the Martimbang inactive volcano (see Figure 3.5). These low magnetic anomalies were interpreted as alteration zones of Andesite (Situmorang, 2005).

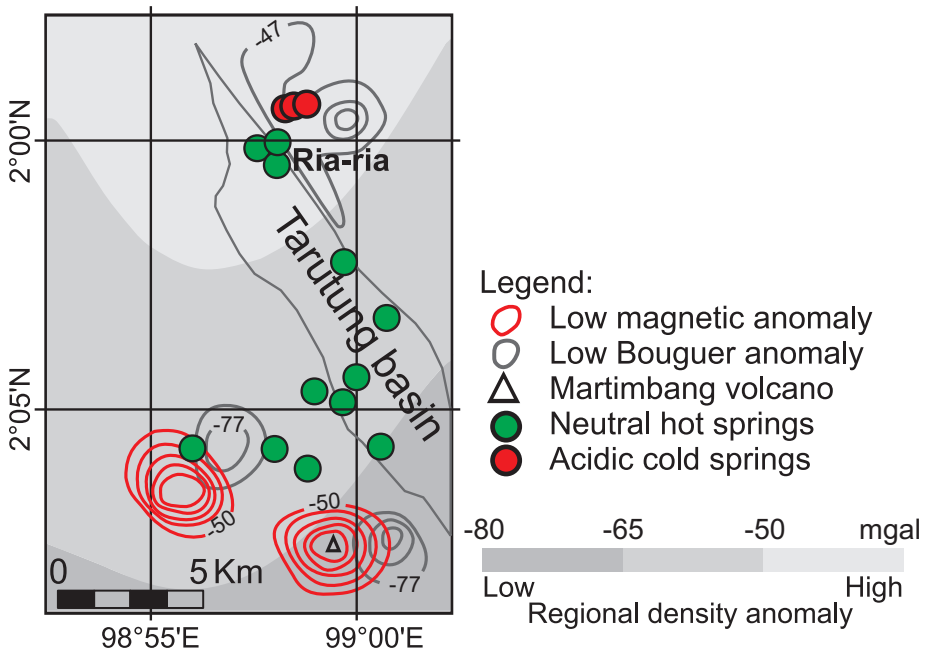

Figure 3.5: Magnetic and gravity anomalies map of the Sipoholon area. The background color shows second derivative regional density anomaly. The contour interval of Bouguer anomalies is 5 mgal. The contour interval of magnetic anomalies is 30 nT (modified from Situmorang, 2005; Djudjun, 2005).

Following Hersir and Bjornsson (1991), negative magnetic anomalies around geothermal manifestations, e.g. hot springs, are caused by decreasing magnetic susceptibility. This decreasing susceptibility is because of the mineral composition change due to hydrothermal alteration. On the other hand, positive magnetic anomalies are commonly caused by normal magnetization

of lavas. The magnetisation of the rocks take place when the rock solidifies. The magnetic moments point in similar directions, so that the material will have high magnetic susceptibility.

A second degree polynomial fitting of the measured Bouguer anomalies was selected to represent a simple regional trend (see the background colour of Figure 3.5). This regional trend map reveals the existence of higher density material in the North, which correspond to the Toba volcano, located 50 km northward from the Sipoholon (Djudjun, 2005). Figure 3.5 also shows that the lowest Bouguer anomaly presents beneath the Martimbang. However, the author does not give any explanation for this anomaly. This low Bouguer anomaly is in contrast to the higher Bouguer anomaly usually found for active or recent volcanoes (e.g Schiavone and Loddo, 2007).

Muksin et al. (2013) found a high Vp/Vs anomaly beneath the Panabungan hot spring (see Figure 3.6). This Vp/Vs anomaly is interpreted as high fluid content in porous media. Based on a laboratory experiments, P-wave velocities are more sensitive to fluids than S-wave velocities (Caricchi et al., 2008). P-wave velocities are higher in saturated rocks than in dry rocks. Thus, high Vp/Vs ratio give evidence for fluid content.

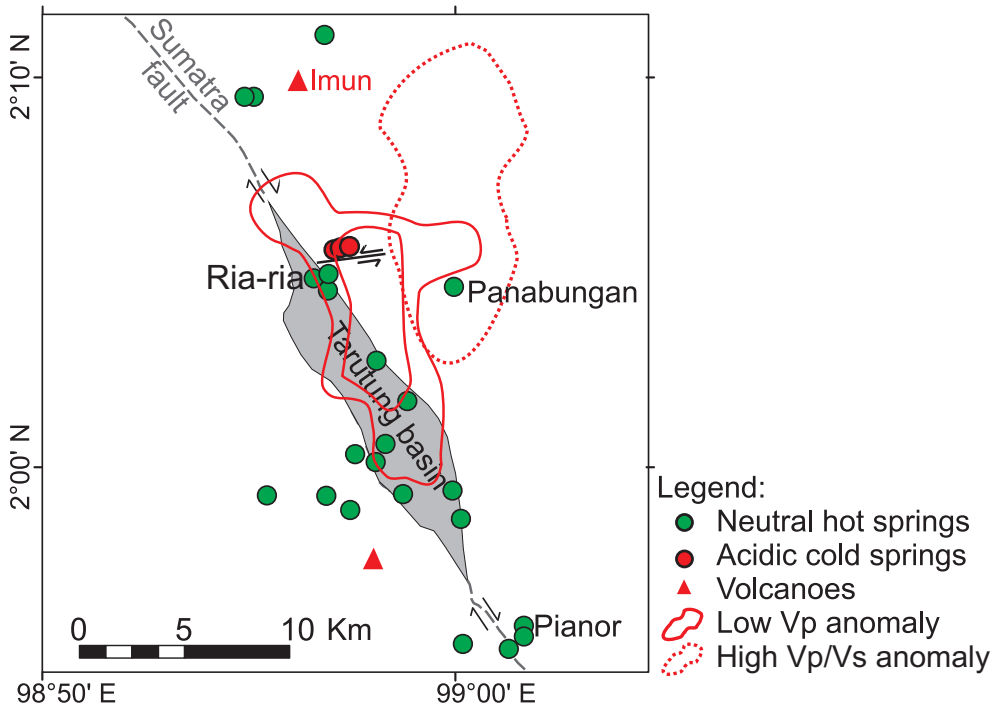

Figure 3.6: Simplified Vp and Vp/Vs anomalies of the Sipoholon area. This map shows a simplified contour map of low Vp (solid red lines) and high Vp/Vs ratio (dashed red lines) at a depth of 2 km. This high Vp/Vs anomaly coincides with the location of the Panabungan fault and hot spring (modified from Muksin et al., 2013).

However, the Vp/Vs anomalies were low beneath the Martimbang volcano (Muksin et al., 2013). Based on a laboratory experiments representing a magmatic reservoir, Vp and Vs decrease with increasing temperature (Caricchi et al., 2008). Thus, a shallow heat source, i.e. a magma chamber, is expected to show low Vp, low Vs, and high Vp/Vs ratio (e.g Caricchi et al., 2008; Koulakov et al., 2009).

3.2 Magnetotelluric measurements

This Magnetotelluric (MT) study is part of several geological, geophysical, and geochemical studies in the framework of the project "Sustainability concepts for exploitation of geothermal reservoirs in Indonesia". The main goal of the project is to derive a new comprehensive conceptual model of the Sipoholon geothermal field. The conceptual model should include the estimation of the possible reservoir location and the heat source mechanism.

There were two MT field campaigns, covering a total area of (23×25) km^2 between two inactive volcanoes in the North and in the South (see Figure 3.7). The MT array covers the hot springs and travertine locations, hence the fluid pathways of these geothermal manifestations could be revealed. MT data were recorded at 96 locations. All profiles were oriented perpendicular to the direction of the Sumatra fault.

3.2.1 Data acquisition

The first field campaign was conducted by the Center for Geological Resources Bandung in December 2010. The aims of this first field campaign were to find out the noise conditions in the study area and to help planning the second field campaign. The site-spacing was 2 km covering an area of (4×5) km^2, with a total survey time of 26 days for 26 MT sites. There was only one MT instrument used, so, no remote reference (RR) site was installed.

The instrument (Phoenix MTU-5A) recorded MT data in the frequency range of 0.003-320 Hz, although the data quality is rather low for frequencies below 1 Hz. Two horizontal coils measured the magnetic fields (H_x and H_y components). The horizontal electric fields (E_x and E_y) were measured by non-polarizable electrodes. All electrodes and coils were connected to ad Data Acquisition Unit (see Figure 3.8a). Acquisition setup and data files were stored on a CompactFlash card which was connected to the Data Acquisition Unit.

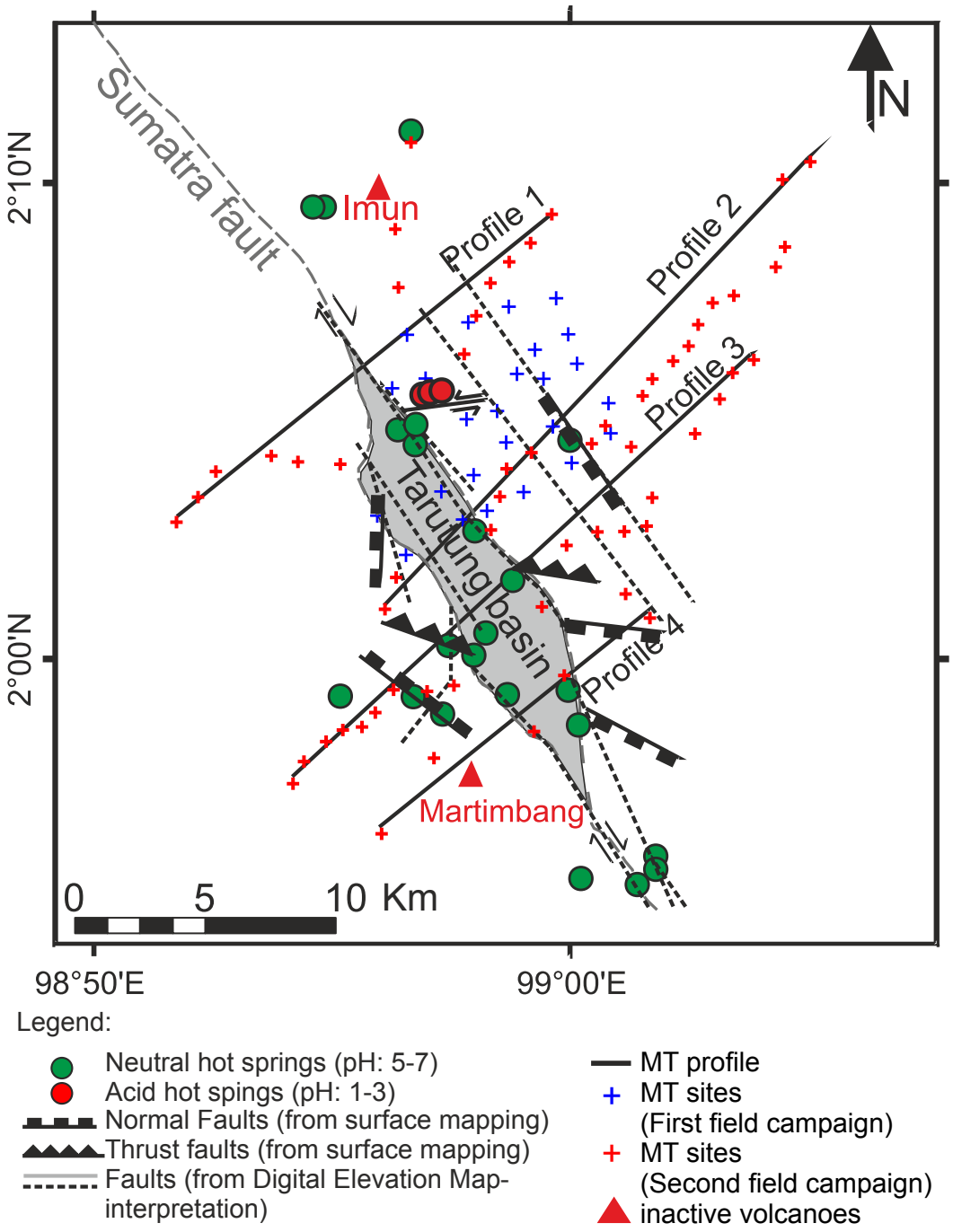

Figure 3.7: MT site distribution over the Sipoholon area. Red and blue crosses show the locations of the magnetotelluric sites. Profiles used in 2-D modelling are shown as black lines (1 to 4). Red triangles mark the location of the two inactive volcanoes (the andesitic Martimbang to the South and the dacitic Imun to the North) in the study area. Hot springs are shown as green dots, surface traces of faults as black and grey lines.

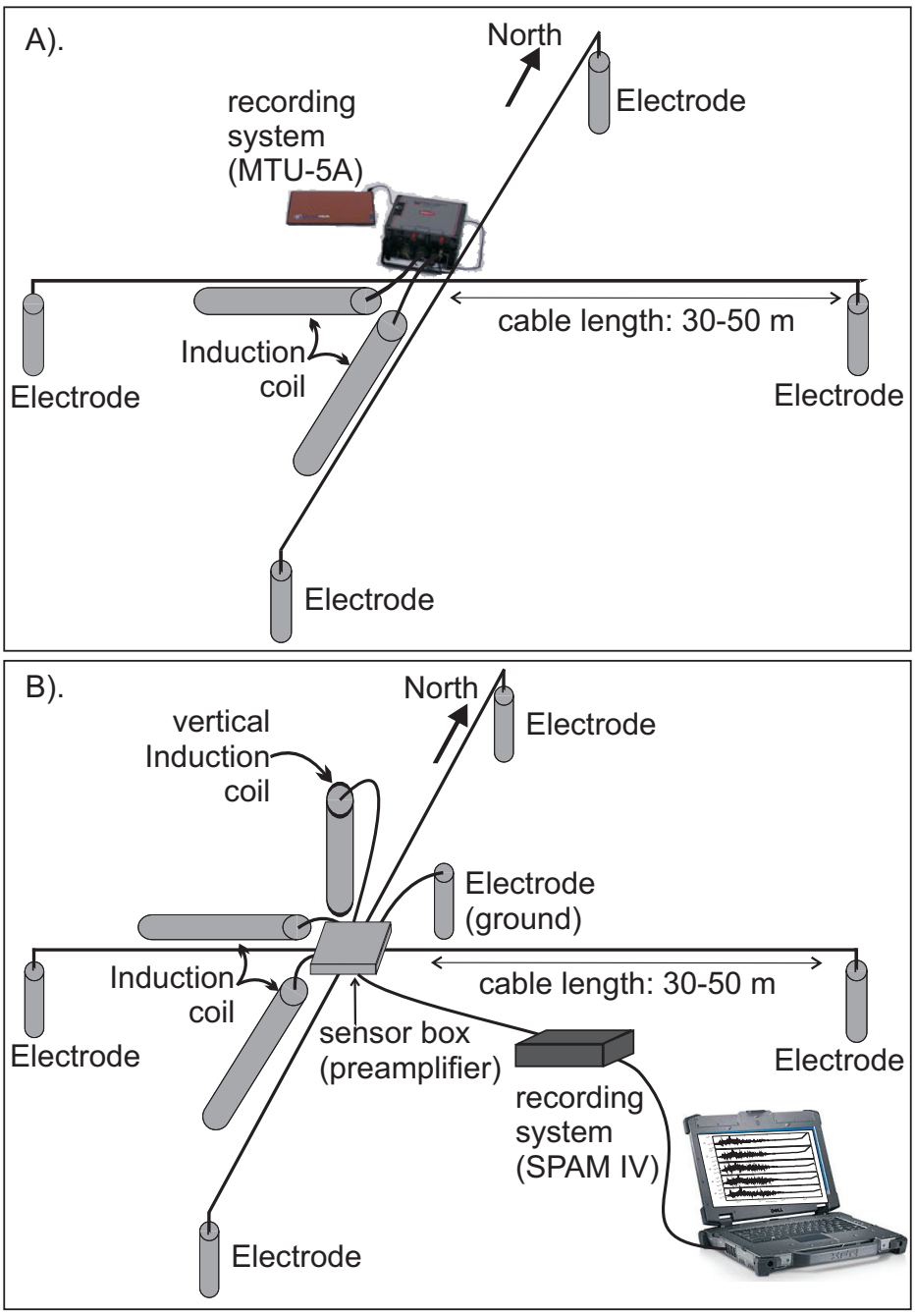

Figure 3.8: Schematic instrument set-a up of MT sites used for the field campaigns in December, 2010 (a) and July, 2011 (b). All sensors were aligned according the geomagnetic coordinate system. The first field campaign used MTU-5A data recording system and two coils only, while the second field campaign used data recording system of S.P.A.M. MkIV and three coils.

The second field campaign was conducted by GFZ in July 2011 using 12 MT instruments. The aim of this field campaign was to image the subsurface conductivity distribution of the Sipoholon area, including the possible fluid pathways beneath the hot springs. The spacing between sites was about 1 km covering an area of (23×25) km^2. However, some sites had more than 2 km spacing due to the presence of high voltage power lines and accessibility problems.

For the second field campaign, five components (E_x, E_y, H_x, H_y, and H_z) were measured at 70 MT sites with one additional RR site. The magnetic fields were measured using Metronix MFS06 and MF07 induction coils. Non-polarizable silver-silver chloride electrodes measured the horizontal electric fields. All sensors were connected to the sensor box which was linked to the S.P.A.M. (Short-Period Automatic Magnetotelluric) MkIV real-time MT systems provided by the Geophysical Instrument Pool Potsdam (see Figure 3.8b).

The S.P.A.M. MkIV recorded data in the frequency range 0.003 Hz to 10 kHz. The instruments used in the second field campaign recorded two types of time series. First, a time series was recorded for two minutes of data with sampling frequency of 25 kHz, and a time series was recorded for 30 minutes of data at 6,25 kHz sampling frequency. Second, time series were recorded continuously for three days, consisting of 10 minutes per-hour data at 500 Hz sampling frequency and continuous data at 50 Hz sampling frequency.

In both field campaigns, all sensors were aligned to the geomagnetic direction (x is parallel to the North-South direction and y is parallel to the East-West direction) (see Figure 3.8). The magnetic declination in the study area during the field campaigns is negligible ($0.5\,^\circ$). Therefore, geomagnetic directions were assumed equal to the geographic directions.

3.2.2 Data processing

The data from the first field campaign were processed by PSDG and provided as EDI spectra. These EDI spectra were obtained from the automatic processing scheme of SSMT 2000 in the instruments. In the following, the processing of the data obtained by GFZ in 2011 is described.

Data were processed using the robust processing algorithms of the EMERALD software package, based on the assumption of magnetic source field homogeneity and spatial coherency (Ritter et al., 1998; Weckmann et al., 2005; Krings, 2007; Chen, 2008). However, the assumption that the horizontal magnetic field components are free of noise, is not always fulfilled. The study area is densely populated and is surrounded by high voltage power lines and hydro power plants. All of the MT data contain high frequency noise due to high voltage power lines, particularly site 315 (Figure 3.9) which was set up 300 m away from an electric transformation station.

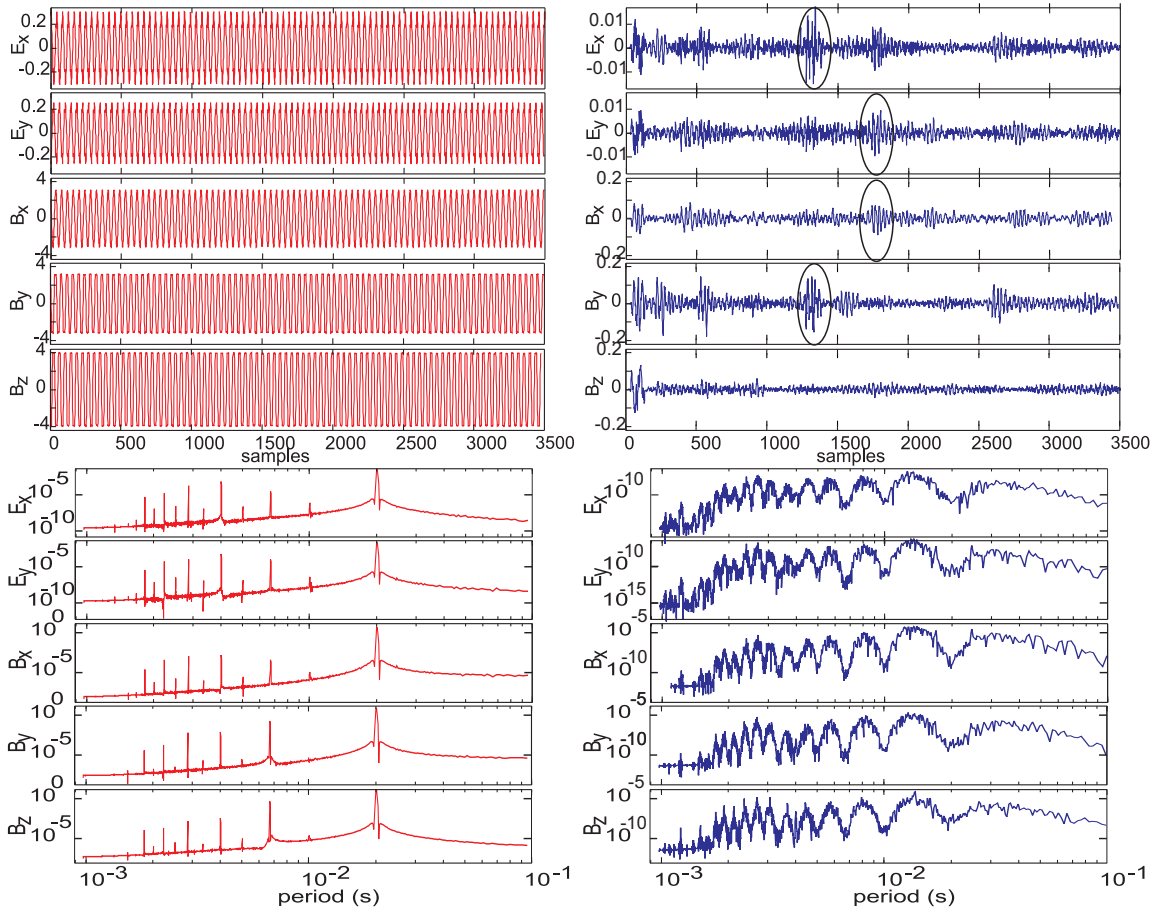

Figure 3.9: a). Left: Time series of station 315 which is contaminated by power line in the time domain (upper left) and frequency domain (lower left). In frequency domain, the peak of noise are in frequencies 50 Hz, 100 Hz, 149 Hz, 199 Hz, 249 Hz, 299 Hz, 348.5 Hz, 398 Hz, 448 Hz, 498 Hz, and 547 Hz. b). Right: Time series of station 315 after delay line filtering. Black ellipses show the exemplary signals of Ey & Bx and Ex & By which were uncovered after the filtering.

Figure 3.9 shows the typical high frequency noise at 50 Hz and the corresponding harmonics at site 315. This high frequency noise due to power lines is a common problem for MT data in densely populated areas. Figure 3.9a shows a typical time series for all Sipoholon MT data. This 50 Hz signal was filtered out using delay line filter (Chen, 2008). After delay line filtering, Figure 3.9b show EM signals which were enclosed by the noise before. Delay line filtering was performed to all data, to improve the data above 50 Hz.

After removing the 50 Hz and harmonics noise at all MT sites, there was still noise present in the high frequency data because some of the distorting signals appear at slightly shifted frequencies, e.g. 149.5 Hz, 199 Hz. This shift might be caused by technical imperfection of electric power system, such as sudden step changes of the power line source current, etc. (Szarka, 1988). MT sites which was set up closer to the high voltage power lines, were more affected than the MT sites which were set up further away from the power lines. For example, at site 315, the noise at frequencies 50 Hz, 149 Hz, and 249 Hz have to be filtered out (Figure 3.10).

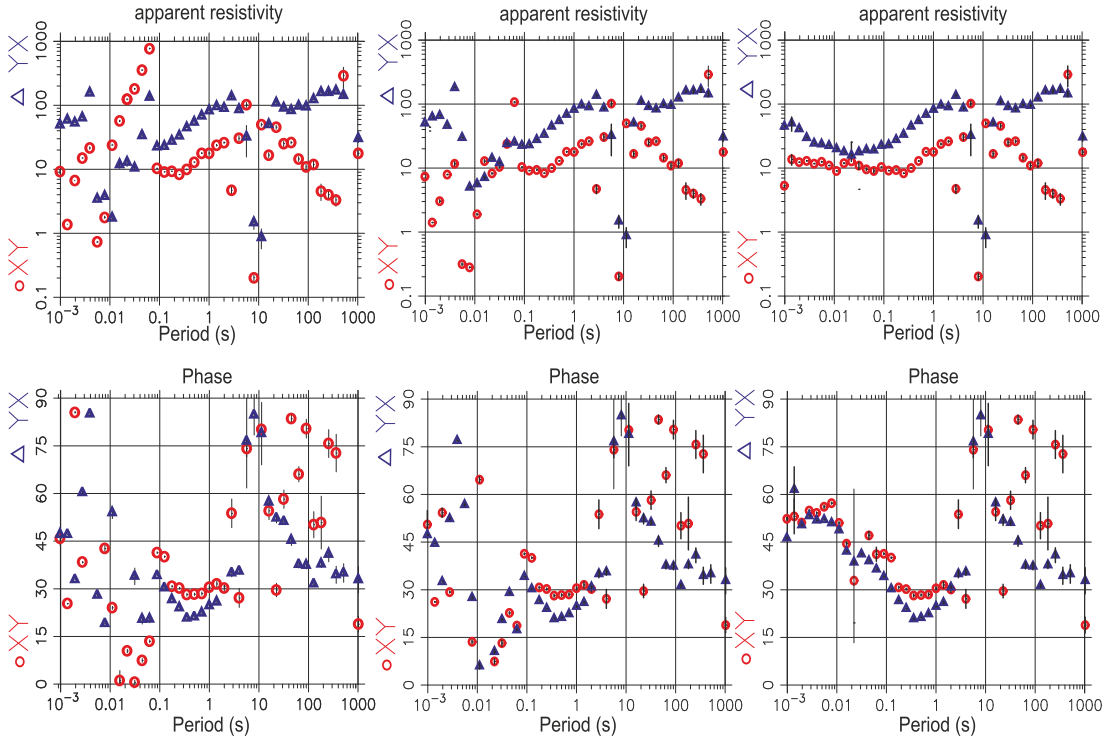

Figure 3.10: Apparent resistivity and phase curves of site 315, before delay line filtering (left), after delay line filtering for 50 Hz and the harmonics (middle), and after successive delay line filtering of 49 Hz, 50 Hz, 149 Hz, and 249 Hz (right).

Figure 3.10 shows that the successive delay line filter improved the high frequency data above

50 Hz even for the site 315. Figure 3.10 also reveals that removing the 50 Hz and harmonics only is not enough to improve the high frequency data due to shifted frequencies. The summary and details of the frequencies which have been filtered out are shown in appendix E.

In parallel to single site processing, including filtering which was explained before, remote reference processing was performed. Unfortunately, the signal to noise ratio of the data in the dead band (0.1-10 Hz) is lower after the RR technique was applied, especially in the phase curve (see Figure 3.11).

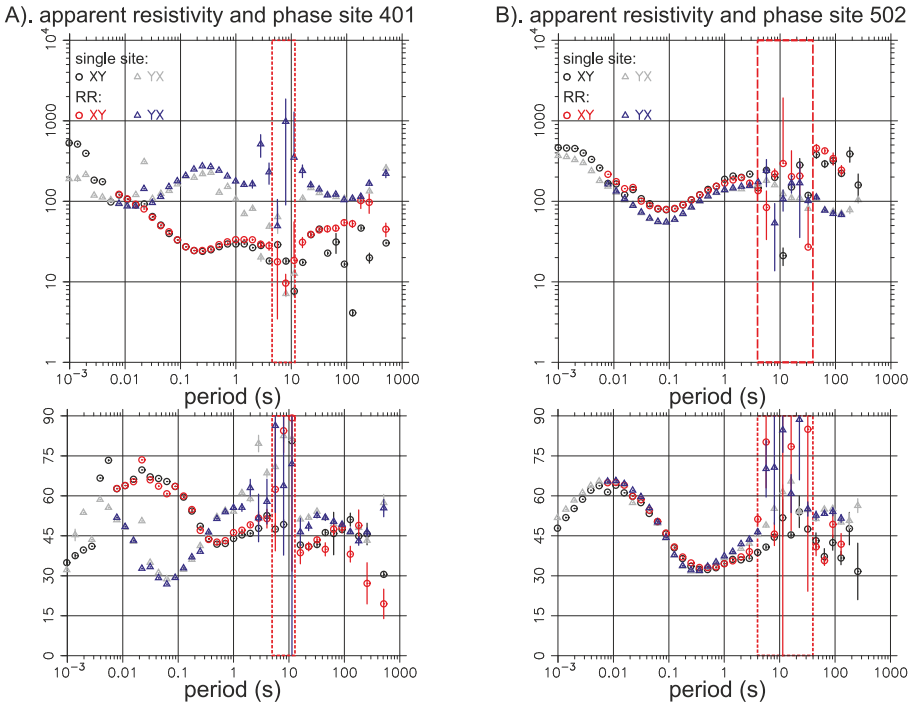

Figure 3.11: The apparent resistivity and phase of site: A) 401 and B) 502. Black circles and grey triangles indicate data points of single site processing, i.e. before delay line filter. Red circles and blue triangles denote data points from remote reference processing. Red dashed outline indicates the frequency range where the RR data contains coherent noise.

The study area is densely populated with high voltage power line and big power plants in the whole Sumatra island. There is a 50 MW hydraulic power plant at a distance of 30 km to the SW of Sipoholon. Additionally, there is also a 440 MW hydraulic power plant at a distance of 50 km to the north east from Sipoholon. It was therefore impossible to find a good location for RR site. The other possible reason for this phenomenon is low signal strength, because the low solar activity around 2011 (http://www.swpc.noaa.gov/SolarCycle/index.html). As a result, noise in the dead band is even more severe after RR technique was applied.

Thus, for each site, there were two processing steps. The first is single site processing, including successive delay line filter to improve the data quality in high frequency. The second is RR processing to improve data quality in low frequency. An EDI file for each site was created from a combination of data from single site and remote reference processing. Four exemplary curves of sites 101, 116, 323, and 403 which were set up close to power line are displayed in Figure 3.12. Unfortunately, strongly scattered data in the band between 2-20 s indicate the presence of strong coherent noise which cannot be suppressed efficiently by the processing. These outliers data were then manually removed prior to the data analysis and the inversion (grey circles in Figure 3.12).

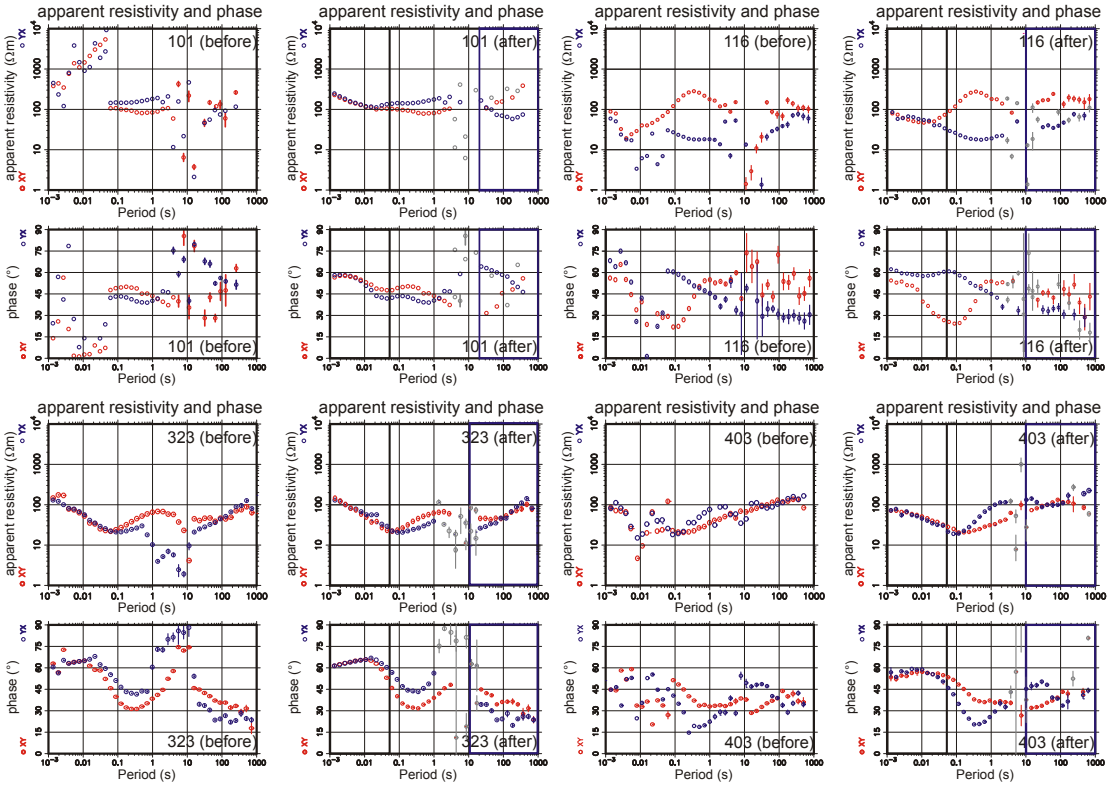

Figure 3.12: The apparent resistivity and phase of site 101, 116, 323, and 403, before (left) and after (right) delay line filtering and remote reference processing was applied. Delay-line filtering improves the high frequency part of the curve (> 49 Hz) (black rectangles), while the remote reference technique improves the low frequency data (blue rectangles). The outliers data were manually removed before the data analysis and the inversion (grey circles).

3.2.3 Data analysis

The Sipoholon MT data set have been assumed having a regional 2-D structure due to its geological setting (see Section 3.1). In order to verify this assumption, if the data are suitable for 2-D inversion approach, impedance tensor analysis should be done. The data analysis was performed using two techniques: the magnetotelluric phase tensor (simply called as phase tensor by Caldwell et al. (2004)) and the magnetotelluric ellipticity criterion by Becken and Burkhardt (2004). Additionally, real induction arrows, derived from horizontal and vertical magnetic field, were also analysed. The real induction arrows, pointing away from conductors (Wiese convention, Wiese (1962)), can contributes to confirm the geo-electric strike direction (Caldwell et al., 2004).

Magnetotelluric phase tensor

Following Caldwell et al. (2004), the phase tensor ($\mathbf{\Phi}$) is the ratio of real ($\mathbf{X}$) and imaginary ($\mathbf{Y}$) parts of the complex impedance tensor ($\mathbf{Z}$),

$\mathbf{\Phi} = \mathbf{X}^{-1}\mathbf{Y}$,

where

$\mathbf{Z} = \mathbf{X} + i\mathbf{Y}$.

In a Cartesian coordinate system (x,y), the phase tensor ($\mathbf{\Phi}$) has a matrix from:

$$\mathbf{\Phi} = \begin{bmatrix} \Phi_{xx} & \Phi_{xy} \\ \Phi_{yx} & \Phi_{yy} \end{bmatrix}. \tag{3.1}$$

The phase tensor ($\mathbf{\Phi}$) can be illustrated as an ellipse, which consisted of minimum (Φ_{min}) and maximum (Φ_{max}) principal axes and skew angle (β) (Caldwell et al., 2004). To notify, the skew angle (β) is commonly displayed as color filling of the ellipses and is defined by the equation:

$$\beta = \frac{1}{2} tan^{-1} \left(\frac{\Phi_{xy} - \Phi_{yx}}{\Phi_{xx} + \Phi_{yy}} \right). \tag{3.2}$$

The properties of the phase tensor ellipses express the dimensionality of the data (Caldwell et al., 2004). If the conductivity structure varies only with depth (i.e. 1-D case), the phase tensor is characterized by a unit circle (Figure 3.13a). In 2-D case, the phase tensor is graphically drawn as an ellipse (Figure 3.13b). The maximum principal axis of the phase tensor ellipse is parallel or perpendicular to the regional 2-D strike.

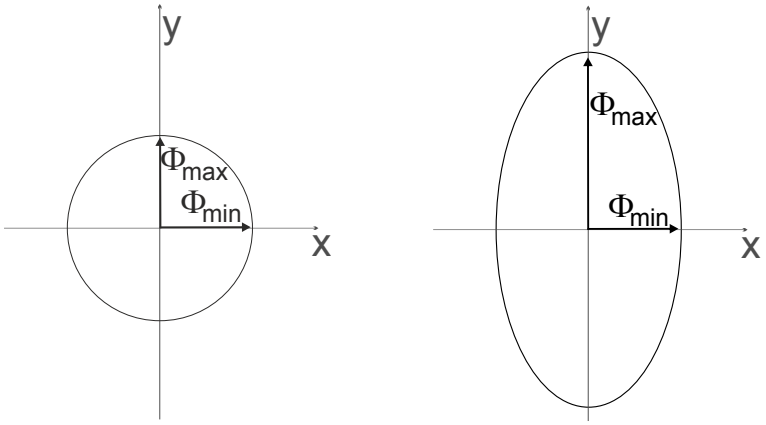

(a) 1-D case: $\Phi_{min} = \Phi_{max}$ (b) 2-D case: $\Phi_{min} \neq \Phi_{max}$

Figure 3.13: Schematic illustration of the phase phase tensor ellipses properties in 1-D and 2-D cases, in a coordinate system (x,y), modified from Caldwell et al. (2004) and Booker (2013). β is zero for both 1-D and 2-D cases.

If the conductivity structure is 3-D, the phase tensor is non-symmetric ($\beta \neq 0$, Caldwell et al. (2004)). In this case, the skew angle (β), indicating an angle from the maximum principal axis, exhibits a large value, i.e. > 3° (Figure 3.14b) or $\beta < -3^\circ$ (Figure 3.14c). Another indication of a 3-D structure is a rapid lateral change of the principal axes direction between sites.

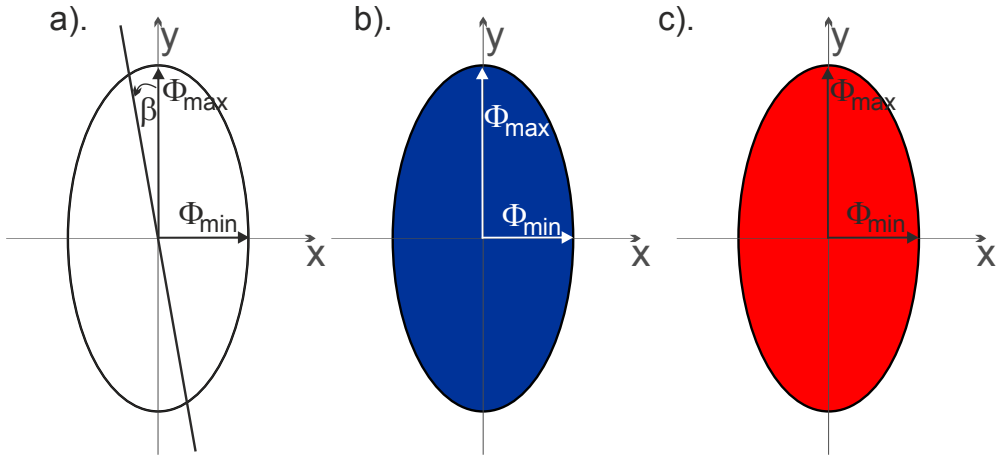

Figure 3.14: Schematic illustration of the phase phase tensor ellipses properties in 3-D case, in a coordinate system (x,y), modified from Caldwell et al. (2004). The skew angle (β), being an angle from the maximum principal axis of the phase tensor ellipse (a), is commonly displayed as color filling of the ellipses. In this study, positive high skew angle ($\beta > 3^\circ$) denotes by dark blue ellipse (b), while negative high skew angle ($\beta < -3^\circ$) indicates by red ellipse (c).

Plotting the phase tensor ellipses, overlaid with the real induction vectors, is widely used (Caldwell et al., 2004; Booker, 2013). This map simply shows the dimensionality of the data and gives additional information about the preferred direction of the induction current flow. For 1-D and 2-D cases, the real induction vectors are parallel to one of the principal axes of the ellipse. In 3-D case, the real induction vectors are not aligned with any of the principal axes of the ellipse.

The phase tensor ellipse of the Sipoholon data are drawn for short, intermediate and long periods. At short periods (i.e. 0.0078 s and 0.0156 s, correspond to shallow depths), most of the sites show 1-D character, as indicated by circular phase tensors and small skew angles ($-3^\circ < \beta < 3^\circ$, Figure 3.15). Most of the real induction vectors are point away from the Tarutung basin (TB) and are aligned with the maximum principal axes, particularly in the eastern part of the TB.

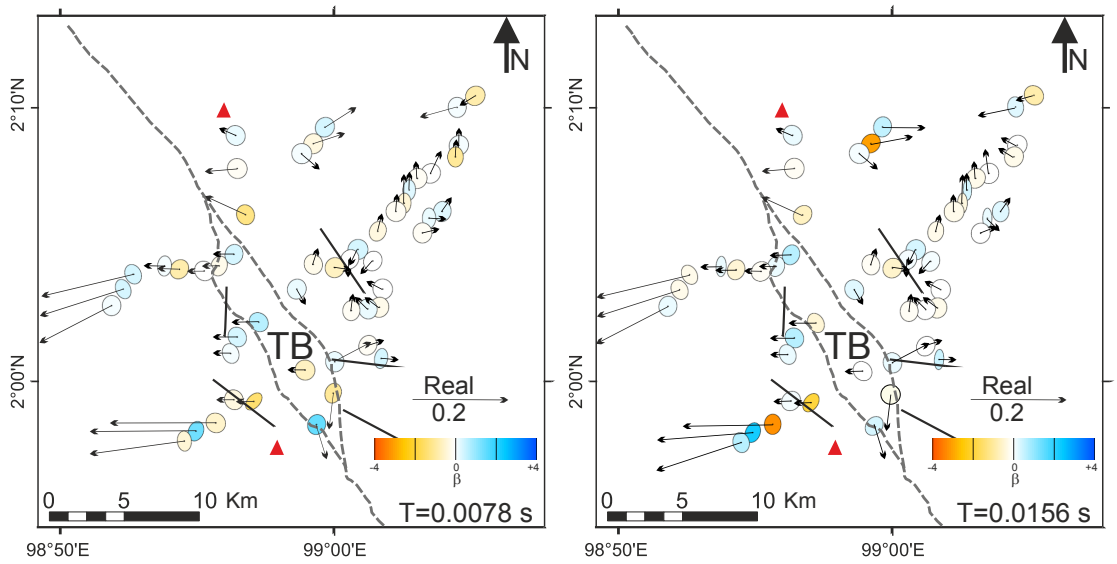

Figure 3.15: Observed phase tensor ellipses and real induction vectors at periods of 0.0078 s and 0.0156 s. The ellipses are normalized with Φ_{max}. The ellipses' colours show the value of the skew angle β. Black lines indicate surface trace of normal faults. Dashed grey lines mark the Sumatra fault and the Tarutung basin. Induction vectors display stronger conductivity contrast in the western part of the Tarutung basin (TB) than in the eastern part. Most of the sites exhibit small values of β and show circular phase tensors, indicating a 1-D character.

At intermediate period (i.e. 1 s), most of the sites exhibit large value of the skew angle (i.e. $\beta > 3^\circ$ or $\beta < -3^\circ$ as indicated by blue or red colours in Figure 3.16). The lateral variation of the skew angle between sites is more complicated, particularly the sites to the east of the TB. The real induction vectors are not aligned with any of the principal axes of the phase tensor. This indicates asymmetric conductivity structure or a moderate 3-D character, particularly at some site close to normal faults (marked by black lines in Figure 3.16).

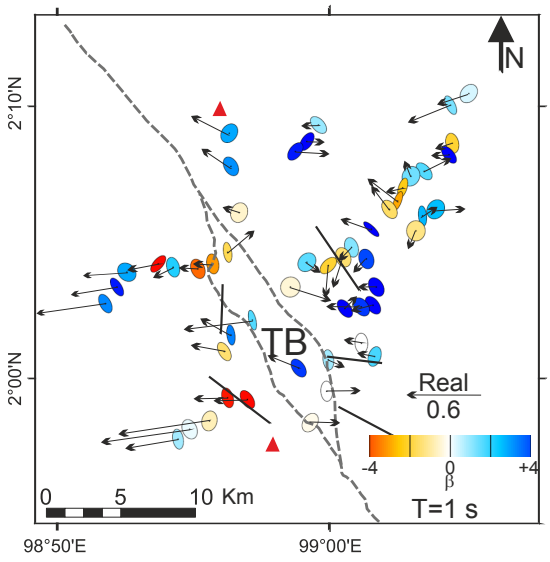

Figure 3.16: Observed phase tensor ellipses and real induction vectors at a period of 1 s. Labels are the same as Figure 3.15, except for magnitude scale of the real induction vector. Most of the sites close to the normal faults exhibit high values of β (as indicated by red or blue colours), indicating a 3-D character. Induction vectors display the strongest conductivity contrast (i.e. indicated by high magnitude) at this intermediate period than short or long periods. The induction vectors also display stronger conductivity contrast in the western part of the (TB) than in the eastern part.

At long periods (i.e. 128 s and 256 s, reflecting the deep structure), the lateral change of the principal axes direction between sites is less complicated than at a period 1 s. Most of the principal axes of the ellipses point to NW-SE and are perpendicular to the real induction vectors, particularly in the western part of the TB. This indicates that most of the data have 2-D character,

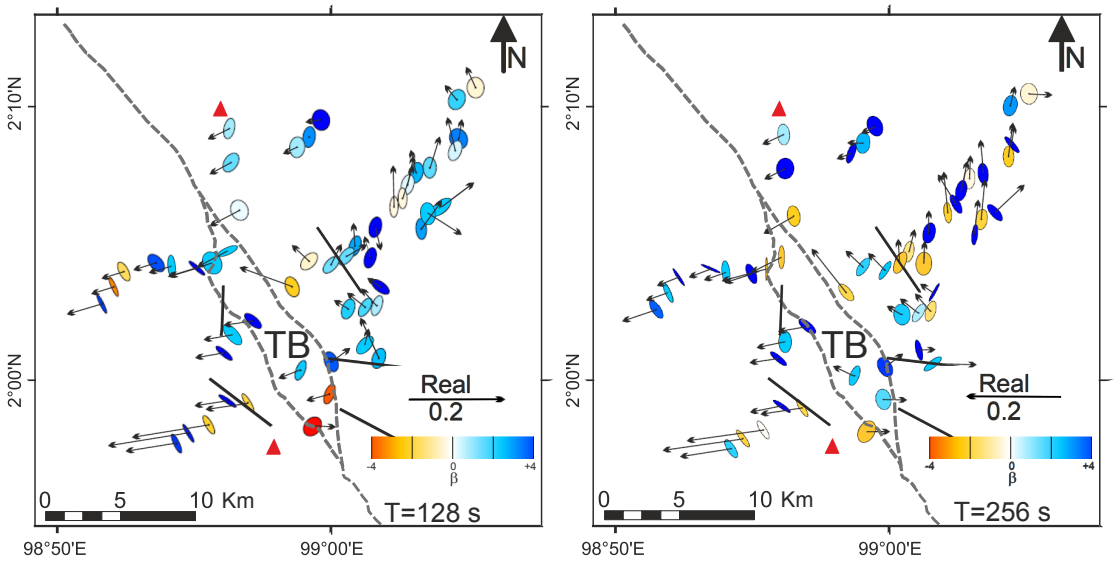

Figure 3.17: Observed phase tensor ellipses and real induction vectors at periods of 128 s and 256 s. The ellipses are normalized with Φ_{max}. Labels are the same as Figure 3.15. Most of the sites close exhibit small values skew angles ($-3 < \beta < 3$), indicating a 2-D character. Most of the real induction vectors point away from the basin, e.g. to the SW.

showing a direction of NW-SE, which is parallel to the Sumatra fault direction. However, the phase tensor method is limited for subsurface dimensionality analysis (Caldwell et al., 2004). This method does not show certainly the geo-electric strike direction of the Sipoholon MT data.

Magnetotelluric ellipticity criterion

In order to find the preferred geo-electric strike direction and to confirm the dimensionality of the data, the impedance tensors were analysed using the code from Becken and Burkhardt (2004). The authors show that the telluric vectors (eq. 2.8) are linearly polarized (the minor axis of the ellipse is zero) only if the impedance tensor is rotated to a coordinate system is parallel or perpendicular to the 2-D regional strike. Hence, one can rotate the impedance tensor until the minor axes of the telluric vectors are (close to) zero or exhibit small ellipticities.

The averages ellipticties at site 212, being representative for the Sipoholon data set, are $\varepsilon_x = -0.04 \pm 0.06$ and $\varepsilon_y = 0.02 \pm 0.17$ (Figure 3.18a). Following Becken and Burkhardt (2004), small ellipticities of the telluric vectors indicate 2-D regional structure. This means that the site 212 as well as most of the other sites show 2-D character. However, there is an exception between 1 s and 100 s, exhibiting higher ellipticities (> 0.02). This indicates that in this period range the data are displaying 3-D character, which is similar to the result of the phase tensor analysis at a period of 1 s (Figure 3.16).

Figure 3.18b displays the real imaginary parts of induction vector of site 212. At periods of 1-10 s, the real induction vector exhibits high magnitude, which occurs at all sites (Figure 3.16). The induction vector mostly point to the NE, as indicated by black arrows in Figure 3.18c. This NE direction is perpendicular to one of the geo-electric strike direction (gray colour) and to the NW-SE Sumatra fault.

Figure 3.19 shows the rose diagrams (circular histograms) of geo-electric strike angles (a-c) and induction vectors (d-e) for different period ranges for all sites. The rose diagrams at short periods (indicating shallow subsurface, Figure 3.19a) and for all periods (Figure 3.19c), exhibiting directions of N0 °W or N90 °W, do not show clear indication of any preferential strike direction. Strike directions are poorly defined if data are very noisy or if the subsurface is predominantly 1D for the respective induction volume.

Figure 3.19b displays a more obvious preferred direction, i.e. N36 °W and N54 °E (with a 90 ° ambiguity). At periods of 1-1000 s, the induction vectors point mostly to the W-SW. It should be noted that site 212, displaying NE direction of the induction vector, is located to the east of the TB. The other sites located to the west of the TB exhibit W-SW direction of the induction vector.

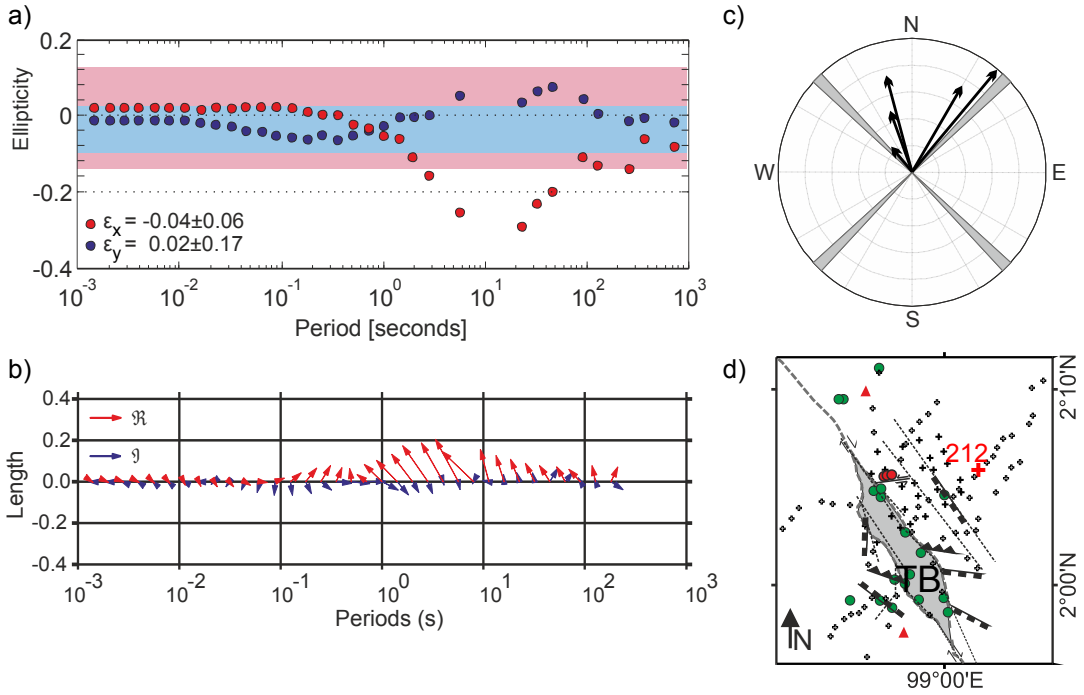

Figure 3.18: (a) Ellipticity of the telluric vectors (columns of the impedance tensor) for site 212. Most of the data show low ellipticities (< 0.02) indicating 2-D character, except at periods of 1-100 s displaying higher ellipticities (> 0.02) suggesting moderate 3-D character. (b) Real (red) and imaginary (blue) parts of induction vectors of site 212. The real induction vectors at periods of 1-10 s exhibit high magnitude, which occurs at all sites (see Figure 3.16). (c) Rose diagram of geo-electric strike direction (gray colour) resulted from the code of Becken and Burkhardt (2004) overlaid with the direction of real induction vector (black arrow). The geo-electric strike for all periods display NW-SE and NE-SW directions. Most of the real induction vectors exhibit N52 °E, resolving the 90 ° ambiguity of the strike. The real induction vectors point perpendicular to the geo-electric strike direction. (d) Location of site 212. Labels are the same as Figure 3.2.

The direction of the induction vector solves the $90\,^{\circ}$ ambiguity of TE- and TM-mode (see Section 2.3). The induction vector is perpendicular to the TE-mode (i.e. the geo-electric strike direction). Hence, a preferred geo-electric strike angle of N36 °W (indicated as solid black line in Figure 3.19b) is chosen. At long periods, this direction, i.e. N36 °W, is almost perpendicular to the real induction vector (Figure 3.19e).

Figure 3.19b also indicates that the data represent a 2-D structure at long periods. The preferred geo-electric strike (i.e. N36 °W) is consistent with the direction of the 1650 km long strike slip Sumatra fault ($\mathrm{N}40\,^{\circ} \pm 5$W by Genrich et al. (2000)). This NW-SE direction is also similar to average direction of the principal axes of the phase tensor ellipses (Figures 3.15, 3.16 and 3.17). This is also an indication that most of the data fulfill the assumption for 2-D inversion.

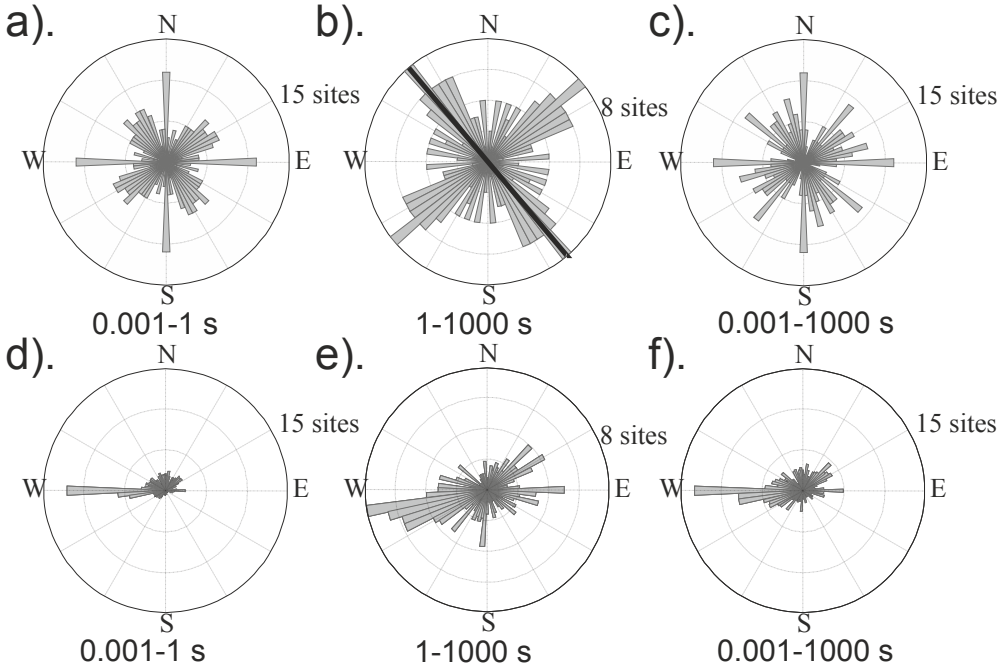

Figure 3.19: Top: Rose diagrams of the geo-electric strike directions obtained for short periods (0.001-1 s) (a), long periods (1-1000 s) (b), and all periods (0.001-1000 s) (c). These rose diagrams exhibit a direction of the ellipticities of telluric vectors. The solid black line indicates a strike direction of N36 °W. Bottom: Rose diagrams of the real induction vector directions for the same period range as a-c.

Chapter 4

2D and 3D Inversion Results

The impedance analysis of the Sipoholon data set shows that the data are compatible with a 2-D character and yield a strike direction of N36 °W. Additionally, most of the induction vectors point perpendicularly to this direction, which is also an indication of the mostly 2-D character of the data. The direction of N36 °W is similar to the Sumatra fault direction in this area. Hence, in this study, a 2D inversion was performed. A large number of models were inverted using different values of data weighting, global smoothing parameter (τ) and ratio of horizontal and vertical smoothing parameter (α). A 2D preferred model was selected according to the optimal values of the tested parameters (see Section 4.1).

Although the data set is compatible with a 2-D interpretation, some sites (particularly those close to fault systems) and periods indicate a possible 3-D character (see Figure 3.16). Additionally, in a 3-D inversion, it is possible to validate whether the conductive structures imaged from the 2-D inversion have some horizontal extent (along strike). A number of models were inverted using different data components and rotation angles. The 3-D inversion procedure is explained in the Section 4.2.

After a 3-D preferred model was chosen, the preferred models from the 2-D and 3-D inversion were compared. The interpretation of the conductivity structures are discussed in the last part of this chapter (Section 4.3), including the integration with other geophysical (seismic velocity, gravity and magnetic), geological and geochemical studies in the Sipoholon area.

4.1 2D Inversion

As mentioned before, most of the Sipoholon data display a 2-D character. Thus, 2-D inversion is considered to be a reasonable approach in this study. Following Rodi and Mackie (2001), an inverse problem can be described generally as:

$$\mathbf{d=F(m)}, \tag{4.1}$$

where **d** is a data vector, **F** is the forward operator symbolizing the governing equations of the MT modelling, and **m** is is a model vector. The data vector **d** contains observations of the apparent resistivity and phase (or impedances) and VTFs. In each iteration, the objective function $\Phi(\mathbf{m}, \tau)$ has to be minimized:

$$\Phi(\mathbf{m}, \tau) = \Phi_d + \tau\Phi_m \rightarrow min, \tag{4.2}$$

where τ is a regularisation parameter used to weight Φ_d and Φ_m. Φ_d is the data misfit functional, the functional of the misfit between the predicted and observed data. Φ_m is a model roughness functional.

The data misfit functional Φ_d is:

$$\Phi_d = (d - F(m))^T \mathbf{V}^{-1}(d - F(m)), \tag{4.3}$$

where **V** is the error variance matrix (Rodi and Mackie, 2001). In the WinGLink 2D inversion program, one can choose to use the observed data error or the error bound or the error floor to control Φ_d (Rodi and Mackie, 2001). In this study, the observed data errors were not used due to relatively different errors between short and long period data (short period data have small data errors, while long period data have large data errors). An error floor was chosen to give constant error for the whole period range used (0.001-1000 s), so that the short periods and long periods have similar weighting.

Φ_m is a weighted integral of the Laplacian squared of the model, which is controlled by α, a multiplication of horizontal to vertical smoothing (Rodi and Mackie, 2001). The regularization parameter τ represent "a trade-off" between Φ_d and Φ_m (Rodi and Mackie, 2001; Avdeev and Avdeeva, 2009). The choices of τ have a significant impact on the model result due to the ill-posed problems of the MT data inversion (e.g. Avdeev and Avdeeva, 2009).

The 2D inversion is performed along four NE-SW profiles (see Figure 3.7). The northernmost profile (profile 1) aims to detect the subsurface conductivity distribution beneath the Ria-ria hot

spring. Profile 2 was configured to reveal the conductivity distribution beneath the Panabungan hot spring located close to the vertical normal fault. Profile 3 was designed to image the conductivity beneath the Ugan springs cluster located in the flank of the inactive Martimbang volcano. Together with this, profile 4 was planned to verify whether a very low conductivity occurs beneath the Martimbang volcano.

Prior to the inversion, a mesh was generated using the mesh generator included in the WinGLink 2D inversion program (Rodi and Mackie, 2001). The number of cells and the size of each profile are displayed in Appendix A. Profile 2 is shown as an exemplary model result, but the other profiles were treated the same as profile 2. All profiles are cut down to 10 km depths only, except in Section 4.1.5.

All inversions used data from 0.001 s to 1000 s. The xy component rotated to -36 $^\circ$ corresponds to the TE mode and the rotated yx component to the TM mode. The inversion data set also consists of vertical magnetic transfer functions (VTFs) at most of the stations. The data were manually edited to remove data points with large scatter or large error bars.

Phase is not affected by galvanic distortion (Caldwell et al., 2004). Therefore, more weight is given to the phase. An error floor of 1.45 $^\circ$ (equivalent to a 5 % of ρ_a error) was used for both TE and TM phases for all 2-D inversions. The error floor of ρ TM was set to 10% for all 2-D inversions, because static shift in ρ TM curve can be partly accommodated by the inversion model (Becken et al., 2008). Different weightings of ρ_a-TE and VTFs data were analyzed and are described in Section 4.1.1.

A number of separate inversions using different τ and α values were performed (see Sections 4.1.2 and 4.1.3, respectively). This was followed by the preferred model inversions, including the sensitivity tests (Section 4.1.4). For all 2-D inversions, a uniform grid Laplacian was used for the regularization operator of the WinGLink 2-D inversion program. The minimizing integral of $\|\Delta(m)\|^2$ was selected as the regularization order in the WinGLink 2-D inversion program.

4.1.1 Data weighting

TE or TM or VTFs data have different sensitivities (e.g. Wannamaker et al., 1984; Berdichevsky and Dmitriev, 2008). The TE data are more sensitive to conductive features elongated along the strike direction (Wannamaker et al., 1984; Berdichevsky et al., 1998), while the TM data are more sensitive to resistive features (Berdichevsky and Dmitriev, 2008). The VTFs are more sensitive to lateral conductivity contrasts (Berdichevsky and Dmitriev, 2008).

Hence, separate inversions of the individual modes (TE-, TM-, and VTFs) were performed using different data weighting (as shown in the lower left corner of each panel in Figure 4.1). A homogeneous half space of 100 Ωm was used as the initial model. The smoothing parameters were kept the same so the inversion results were affected by the data weighting only.

The results of the TE-only inversion (left column of Figure 4.1) reveal a shallow conductive feature beneath the Tarutung basin (indicated by solid black lines in each figure). Two conductors also appear to the right (NE direction) from the Tarutung basin, beneath sites 216 and 208, as indicated by the red and green triangles, respectively. The conductor beneath site 216 shows a deeper vertical extent when the error floor of the ρTE increases.

Results of the TM-only (middle column of Figure 4.1) also display a shallow conductive feature beneath the Tarutung basin, but the conductor is shifted to the left (SW direction). Results of the TM-only inversion also reveal conductive features beneath sites 216 and 208. Both conductors are imaged more to the left (SW direction).

The inversion of VTFs-only (right column of Figure 4.1) shows the shallow conductor beneath the Tarutung basin. The inversion of VTFs-only also image the conductors beneath sites 216 and 208. However, most of the VTF data for T > 100 s were removed due to high error bars. Only some sites have VTFs data up to 512 s. Thus, the inversion of VTFs-only using three different absolute values of error floor show very similar results below 5 km depths.

To better image these resistive and conductive features, a joint inversion of TE-, TM-, and VTFs is more appropriate (Berdichevsky and Dmitriev, 2008). Thus, inversions of the combined-modes (TE-, TM-, and VTFs) were performed using different data weighting to determine their influences on the joint inversion results. First, an error floor of ρ TE was kept at 10% (left column of Figure 4.2) for three inversions using different error floors of VTFs (as indicated in the lower left corner in each panels). Second, a 100% error floor of ρ TE was used (right column of Figure 4.2) for three different inversions.

The comparison of the models (Figure 4.2) show several differences that reflect the influence of down weighting the ρ TE and weighting of VTFs. Figures 4.2a and c show a conductive structure beneath the Tarutung basin with a resistivity of 1 Ωm (as indicated by the red dashed rectangle). The other inverse models display more resistive values within the red dashed rectangle zone (Figures 4.2b and d). From the comparison of the global RMS misfit of each model, it is clearly seen that down weighting the ρ TE generates lower RMS, which means better data fit. Additionally, down weighting the ρ TE is needed to accommodate static shift.

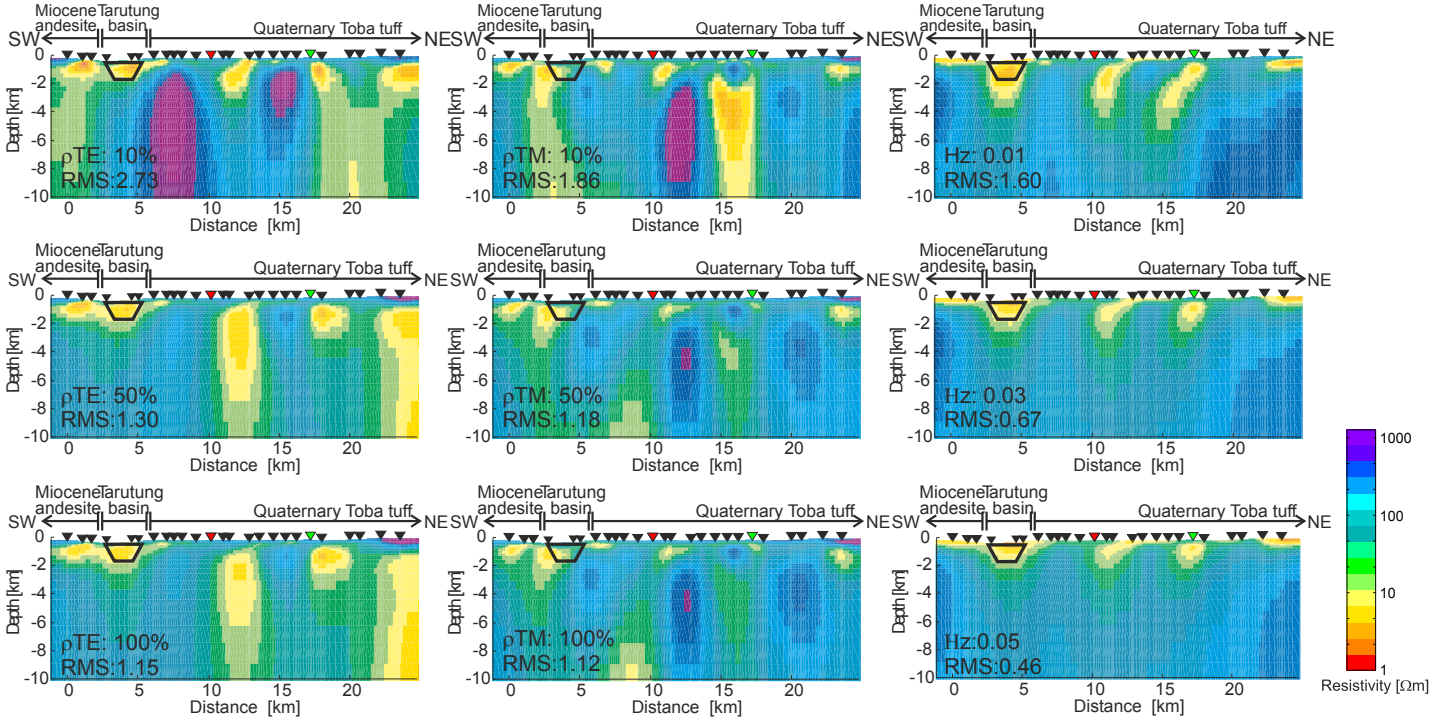

Figure 4.1: 2D inversion results for profile 2 using single component data: TE only (left column), TM only (middle column), VTFs only (right column). Each component used three different error floor settings, as written in the bottom left of each panel. The location of the stations (black triangles) and the main geological features (based on the geological map for Sipoholon, Figure 3.3) are shown on the top of each model. Red and green triangles indicate locations of sites 216 and 208, respectively. The solid black lines beneath the Tarutung basin indicate a shallow bowl-shaped conductive zone. For each column, higher error floor results in a reduction of the RMS values.

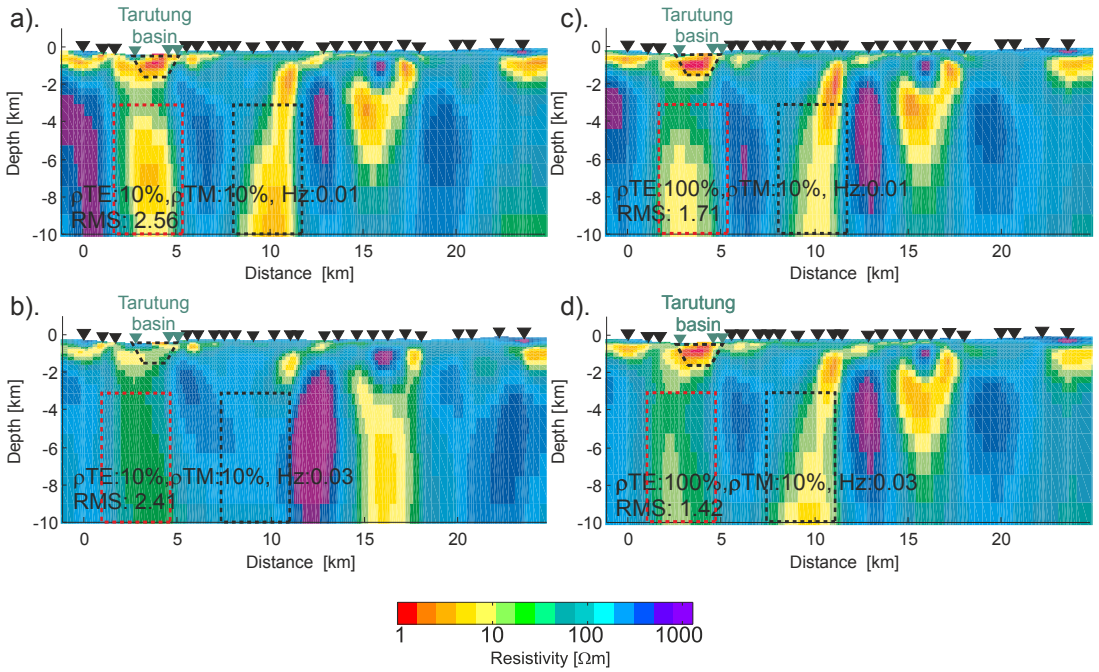

Figure 4.2: 2D inversion results for profile 2 using TE, TM and VTFs. Each model used different error floor settings, as mentioned in the bottom left of each panel. Legends are the same as in Figure 4.1. Left (a-b) and right (c-d) columns correspond to the results of the inversion using ρ TE error floor setting of 10% and 100%, respectively. First (a and c) and second (b and d) rows present the inversion results using 0.01 and 0.03 error floor settings of VTFs, respectively. The red rectangle marks an example of an artifact introduced by setting small error floors for the TE apparent resistivity (see Figure 4.1, TE apparent resistivity 10%). In this case, the inversion generates an extended good conductor (a and c) towards the eastern side of the model to fit the TE responses. The inversion using ρ TE error floor setting of 100% resulted in more resistive area (b and d). The black rectangle marks another area that shows different structures when a different error floor setting was used.

As mentioned before, V is a diagonal matrix with entries inversely proportional to the data errors φ_i for each data point $V = diag(1/\varphi_i)^2$ (equation 4.3). With a fixed 10 % error floor of ρ TE, which was used to give the same weighting over all data periods, the model response was calculated within this 10% of measured ρ TE. The model results, using 10% error floor of ρ TE, exhibit higher RMS misfits and introduce an artifact, such as a deep conductor, beneath the Tarutung basin (as indicated by the red dashed rectangles in Figure 4.2a). This is due to the fact that the ρ TE data, which are noisier, get more weight. Thus, the error floor of ρ TE was not set to 10%, but a 100% was used instead.

The models that used a constant error floor of 0.01 for the VTFs resulted in higher misfits

and higher conductivity on the structures beneath the Tarutung basin (as indicated by the red dashed rectangle in Figure 4.2a or c) and beneath the Panabungan hot spring (as indicated by the black dashed rectangle). A 0.03 error floor of VTFs resulted in a lower RMS misfit and less conductivity on the structures, particularly beneath the Tarutung basin (Figure 4.2b or d). Furthermore, regarding the sensitivity test (Section 4.1.5), the constraint inversion shows that the conductor beneath the PNB is not a continuous vertical conductor (such as indicated by the black dashed rectangle in Figure 4.2c) but rather two separate conductors (i.e. shallow and deeper parts). Thus, the VTFs error floor setting was set to 0.03.

4.1.2 Tau test

Tau (τ) (see equation 4.2) controls the relative weight of the data misfit Φ_d and the model roughness Φ_m (the model norm term penalizes strong resistivity contrasts between neighbouring cells) (e.g. Rodi and Mackie, 2001; Avdeev and Avdeeva, 2009). Thus, the appropriate choice of this parameter (τ) is important because the τ value significantly impacts on the model result (e.g. Avdeev and Avdeeva, 2009). In this study, the L-curve method, described by Hansen (2000), was used to represent the value of τ and the corresponding variations in Φ_d and Φ_m.

The L-curve is a plot of roughness (or regularized solution or Φ_m) and its data fit (Φ_d) (Hansen, 2000). This method gives a simple display showing the optimum trade-off between Φ_d and Φ_m at the corner point of the curve (Hansen, 2000). The corner of the L-curve is a maximum curvature of both Φ_d and Φ_m, where both model regularization and data misfit are balanced.

For each profile, 8 different tau values (logarithmically distributed from 0.1 to 300) were tested. Using the L-curve method, the variation of τ, data misfit Φ_d and the model roughness Φ_m were plotted for each profile (Figure 4.3). Increasing τ yields lower model roughness and higher RMS, and vice versa: low values of τ result in low RMS and high model roughness. τ = 3 is chosen as an optimal τ (the corner point of the L-curve as indicated by filled circle) for profiles 1 and 4. Profiles 2 and 3 show a value of 10 as the optimal τ.

Figure 4.4 shows the model results using four different τ values of profile 2. The tau values and the RMS are given on the left lower corner of each panel. A low value of τ, such as 0.1 or 1 (Figure 4.4a and b), yields low RMS misfit but a higher degree of roughness. This result is to be expected, considering that regularization allows neighbouring cells to have very different conductivity values. However, this kind of model used too small τ is over-fitting the data and introduces more structures which might be an artifact. An example of the artifact structure is a deep conductor beneath the Tarutung basin.

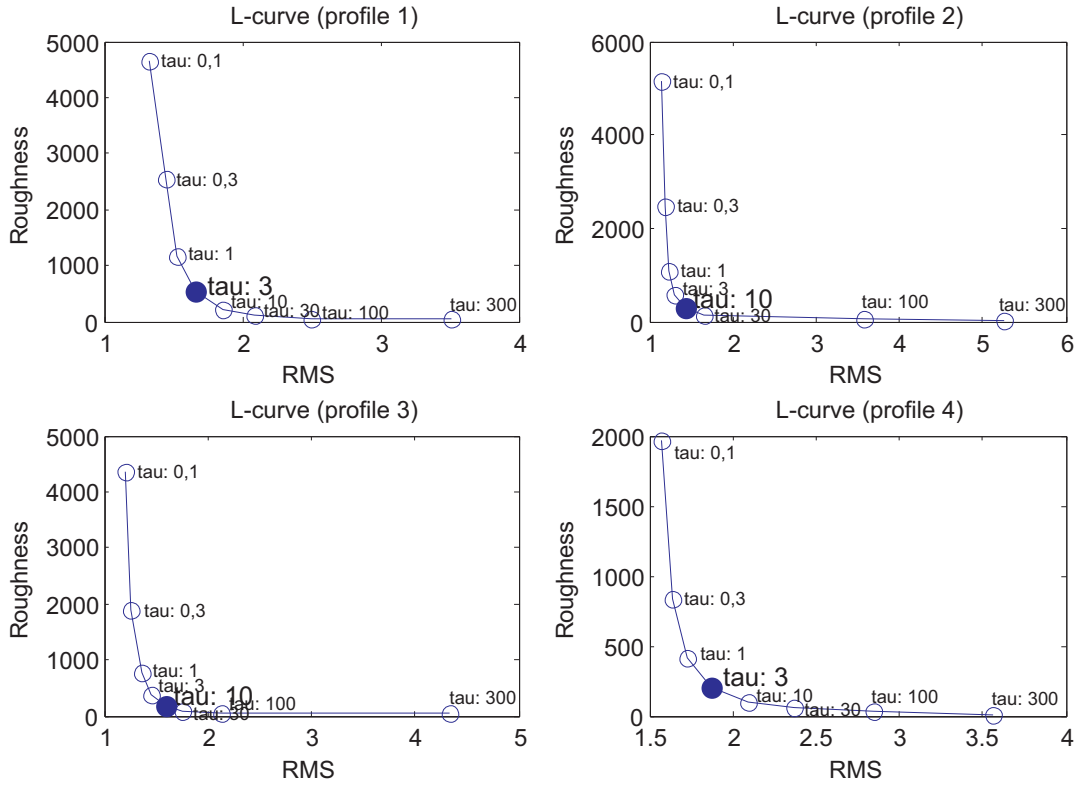

Figure 4.3: Plot of RMS misfit versus roughness (L-curve) for all profiles (profile locations are in Fig. 2). The open circles mark the RMS misfit and roughness values for a range of tau (0.1; 0.3; 1; 3; 10; 30; 100; and 300). The corner point of the curve (marked by the filled circle) represents an optimal trade-off between data misfit and model roughness. For example, the corner point of the curve for profile 2 corresponds to a value of $\tau = 10$ which represents a balance weighting of data misfit and model roughness at the same time.

Figure 4.4c displays the model result using $\tau = 10$ (the optimal τ value for profile 2 as indicated in the corner of L-curve (Figure 4.3)). This τ value represents the model which is not over-fitted nor under-fitted. The results show a shallow conductor beneath the Tarutung basin, but the deep conductor beneath the Tarutung basin does not appear in this model (Figure 4.4c).

Figure 4.4d, using $\tau = 100$, displays a minimum structure model (or lower degree of roughness). The model obtained with $\tau = 100$ is not representative, has very high RMS and shows almost no structure beneath 2 km depths.

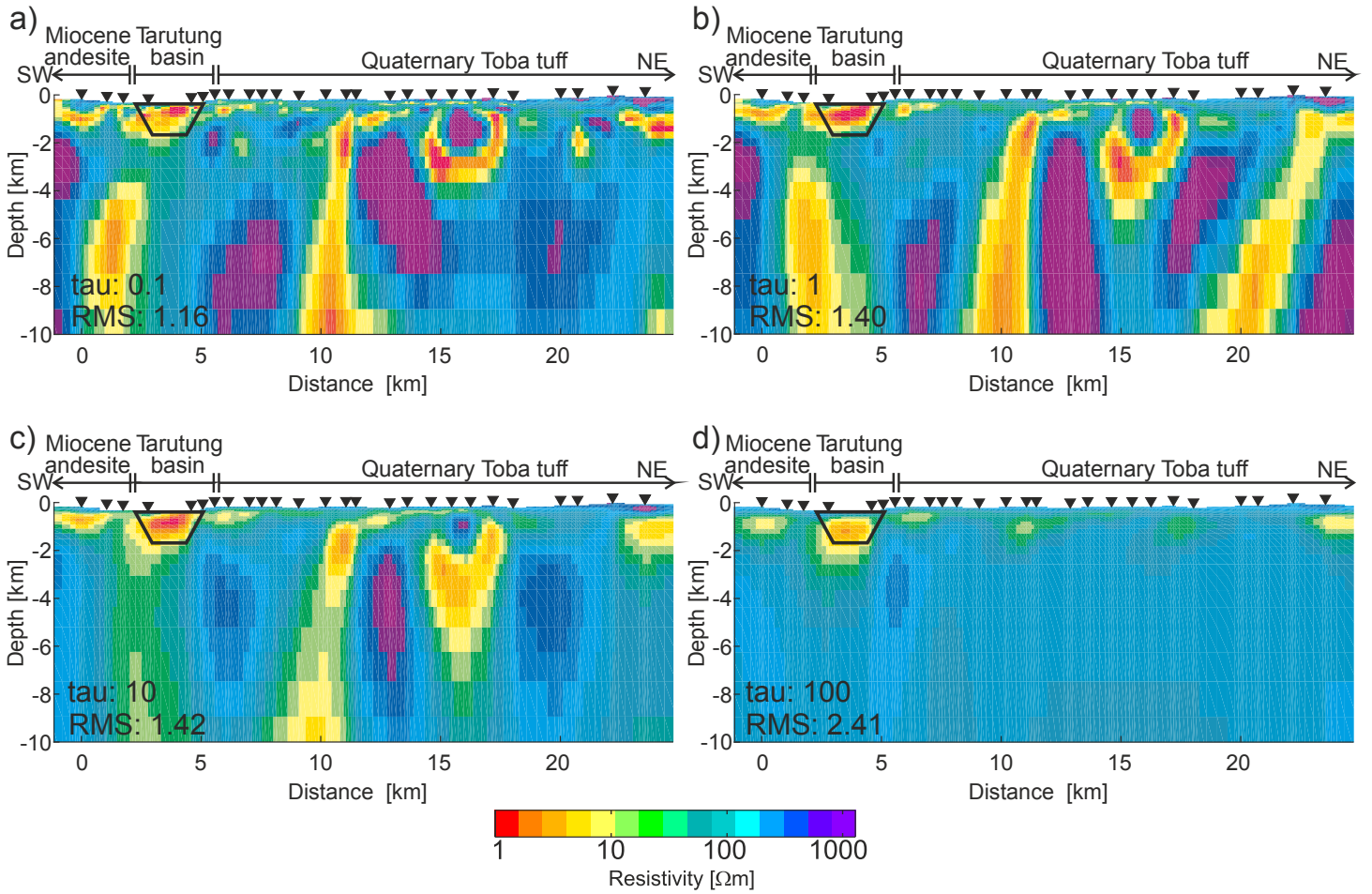

Figure 4.4: 2D inversion results for profile 2 using four different τ values. Legends are the same as in Figure 4.1. Very small tau values (such as τ = 0.1 in the upper left panel) resulted in very rough models, but small RMS misfit. High values of τ yield very smooth models, but high RMS misfit (such as τ = 100 in the lower right panel).

4.1.3 Alpha test

The mesh grid used in this study is not a uniform grid (see Appendix A) and is generated based on the frequency and the resistivity of homogeneous half-space. The cell size below an MT station is smaller than the cell size further away from the stations. The conductivity values of horizontal neighbouring cells depend on the ratio of the horizontal and vertical smoothing (α) (Rodi and Mackie, 2001). Thus, a number of inversions were run to determine the appropriate value of α.

The results indicate that the global RMS misfits are higher with increasing α value (Figure 4.5). The model result using α = 0.0 (Figure 4.5a) exhibits a model with oscillating conductivity values. Each neighbouring cell was allowed to have significantly different conductivity, resulting in over-fitted data that are clearly not reasonable geologically. On the other hand, α = 2.5 (Figure 4.5d) represents an extremely smooth model. Similar to high values of τ, high α values

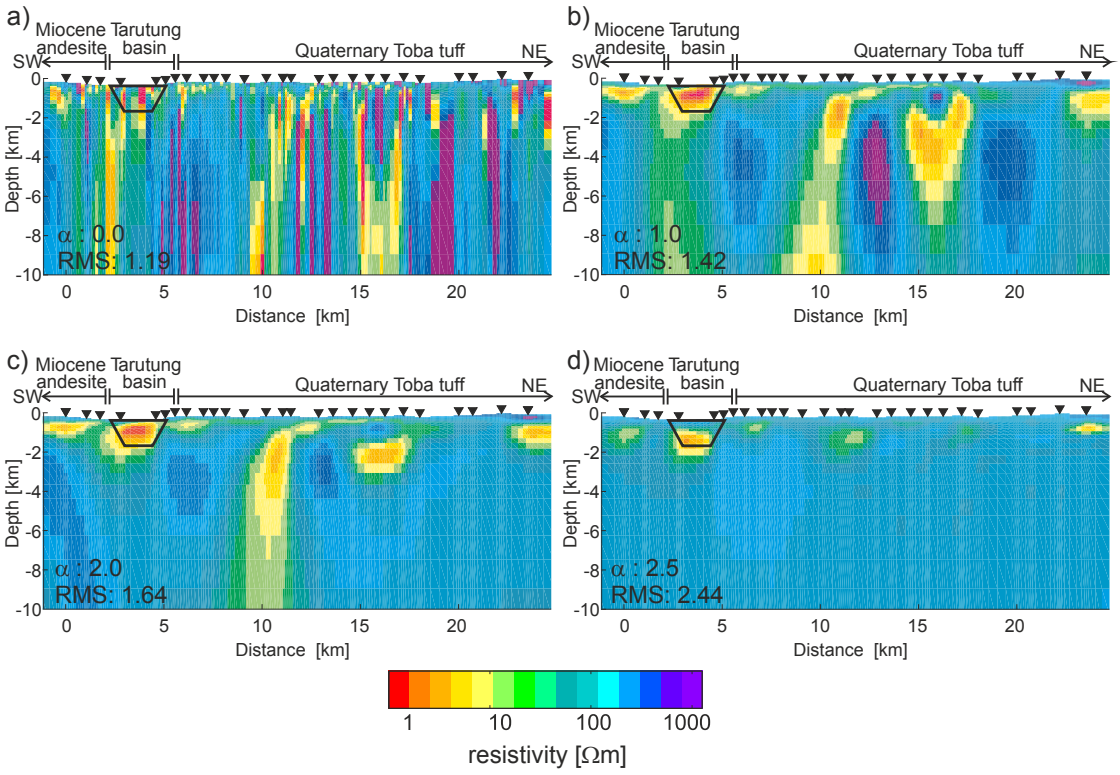

Figure 4.5: 2D inversion results for profile 2 using four different alpha (α). Legends are the same as in Figure 4.1. Similar to τ values, very small α values (such as α = 0.0 in the upper left panel) resulted in very rough models, while high values of α (such as α = 2.5 in the lower right panel) generate very smooth models.

generate models with under-fitted data, i.e. excess smoothness of the model beneath 2 km depths.

The significant differences between the model result using α = 1.0 (Figure 4.5b) and the model result using α = 2.0 (Figure 4.5c) are reflected by the structures beneath 3 km depths. The sensitivity test (Section 4.1.5) indicates that the conductor beneath the PNB extends at least until 20 km depth. This suggests that the model result using α = 2.0 might be under-fitting the data.

The models (Figure 4.5) suggest that the optimal value of α is 1.0. Similar to the optimal τ value, the optimal value of α represents the point minimizing misfit and model norm at the same time. The model features resulted from the inversion using this value (α = 1.0), which is consistent with the features resulted from the inversion test using τ = 10.

4.1.4 Preferred model

Table 4.1 summarized the optimum parameters (i.e. used for the preferred model inversion) resulted from some tests described previously (Sections 4.1.1-4.1.3). The preferred models are derived from joint inversion of (rotated) TE-, TM- and VTF data in the period range 0,001-1000 s. Resistive ($\geq$ 100 Ωm) and conductive ($\leq$ 10 Ωm) structures imaged in the preferred inversion model results are marked by R and C, respectively, in Figure 4.6.

Table 4.1: Parameters values used in the inversion for the preferred model inversion

Parameter	Values
α	1.0
β	1.0 $*$
τ	3.0 (profiles 1 & 4) 10.0 (profiles 2 & 3)
ρTE Error floor	100%
ρTM Error floor	10%
VTFs	0.03
φTE and TM Error floor	1.45 $^\circ$ $*$

$*$: selected based on Rodi and Mackie (2001); Gabas and Marcuello (2003); Becken et al. (2008).

The model for profile 1 reached a global RMS misfit of 1.72 (indicated in the lower left corner of the cross section). The model for profiles 2 and 3 reach a global RMS misfit of 1.43 and 1.70, respectively. Along profiles 1, 2 and 3, a conductive anomaly (C1) appears consistently beneath the Tarutung basin, showing a slightly different depth between profiles. The conductor C1 occurs between a high resistivity anomaly to the southwest (R1) and a resistor to the northeast (R2) (Figure 4.6).

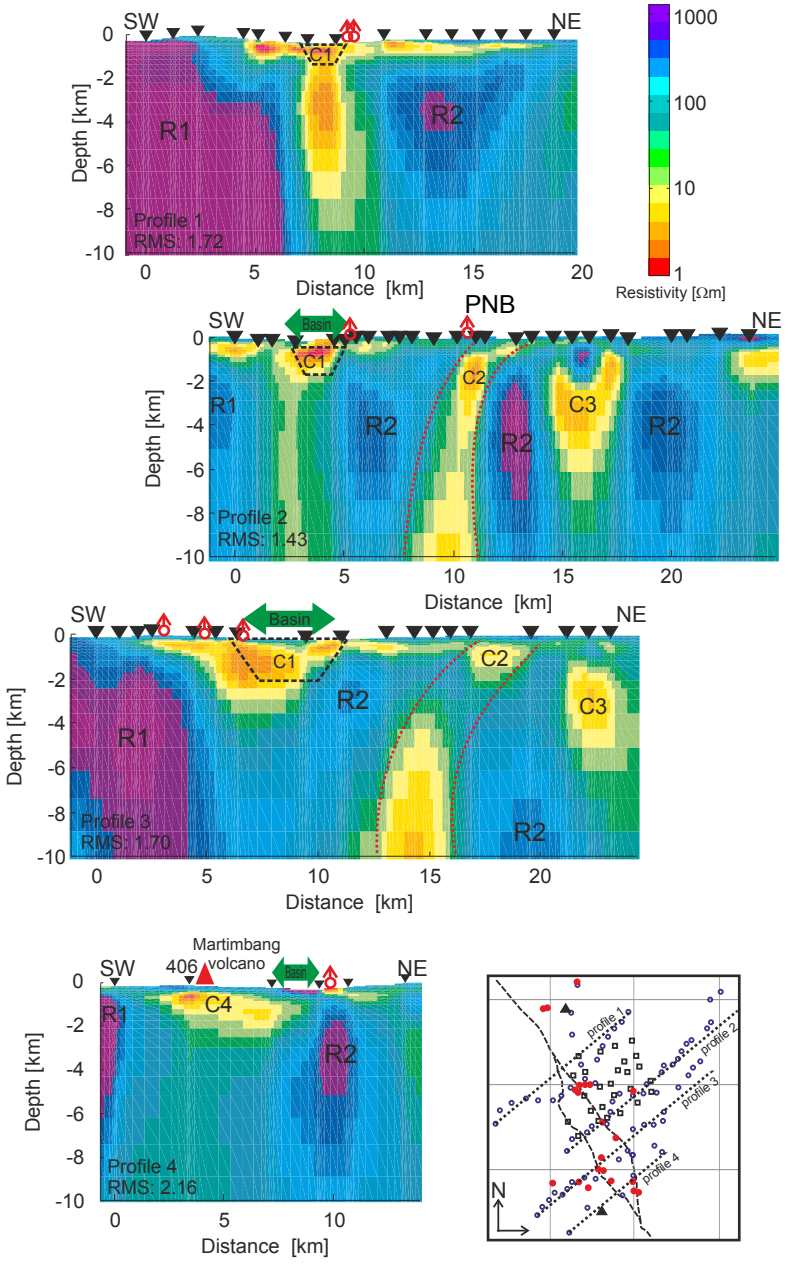

Figure 4.6: 2-D cross sections of four profiles. A deep reaching conductor is revealed along profiles 2 and 3, which coincides with the Panabungan hot spring and fault. The black triangles indicate MT stations. The red "circle & arrow" symbols indicate hot spring locations. Conductive features are labelled with C, resistive features with R. There is no vertical exaggeration on the resistivity models. Distances are in km (no vertical exaggeration). Lower-right: the direction of the profiles with respect to site location (modified from Nukman and Moeck, 2013).

The most striking structure imaged in the 2D inversion is the deep reaching conductive anomaly (C2). This conductor (C2) appears beneath the Panabungan (PNB) hot spring and normal fault zones. The resistivity of C2 reaches values of 3 Ωm at 2 km depth. This conductor C2 extends westward to the Sumatra fault. A thick conductive anomaly (C3) also appears 5 km to the east from conductor C2.

Profile 4 shows the highest RMS (2.16), mainly due to its poorer data quality and smaller number of sites. A shallow conductive body beneath the Martimbang volcano (C4) is imaged up to 3 km depth and was tested by excluding site 406 in a separate inversion. The test produces a similar model, i.e. the conductor C4 appears at a similar depth and resistivity.

Most of the data are well fitted, particularly the TM mode resistivity (Figure 4.7). Although the error floors for both TE and TM phase were set to 5 %, the TM mode phase show a better fit than the TE mode phase. Most VTF data are relatively well fitted, with exception of some sites (e.g. site 225).

The sites located in the west of the study area, site 118 and 120, which were set up above the Permian granite, show ascending resistive values, particularly the TM mode resistivity curves. These types of curves, displaying high resistive values of the ρ TM (> 10^3 Ωm), are typical curves for the sites in the westernmost part of the study are. Other sites, exhibiting ρ TM > 10^4 Ωm, are sites 233 and 234 (shown in Appendix B).

The sites in the eastern area, sites 217 and 219, which were set up above Quaternary Tuff, show similar curve behavior. The TM mode (resistivity and phase) are better fitted than the TE mode. Additionally, the TE mode exhibit better data fit in the short period than in the long period.

Site 225 was deployed above the Tarutung basin and exhibits low apparent resistivity values in both TE and TM modes, particularly between 0.1-1 s. Responses of the TE mode apparent resistivity show a vertical shifting over all periods. In contrast, the TM mode (resistivity and phase) are well fitted.

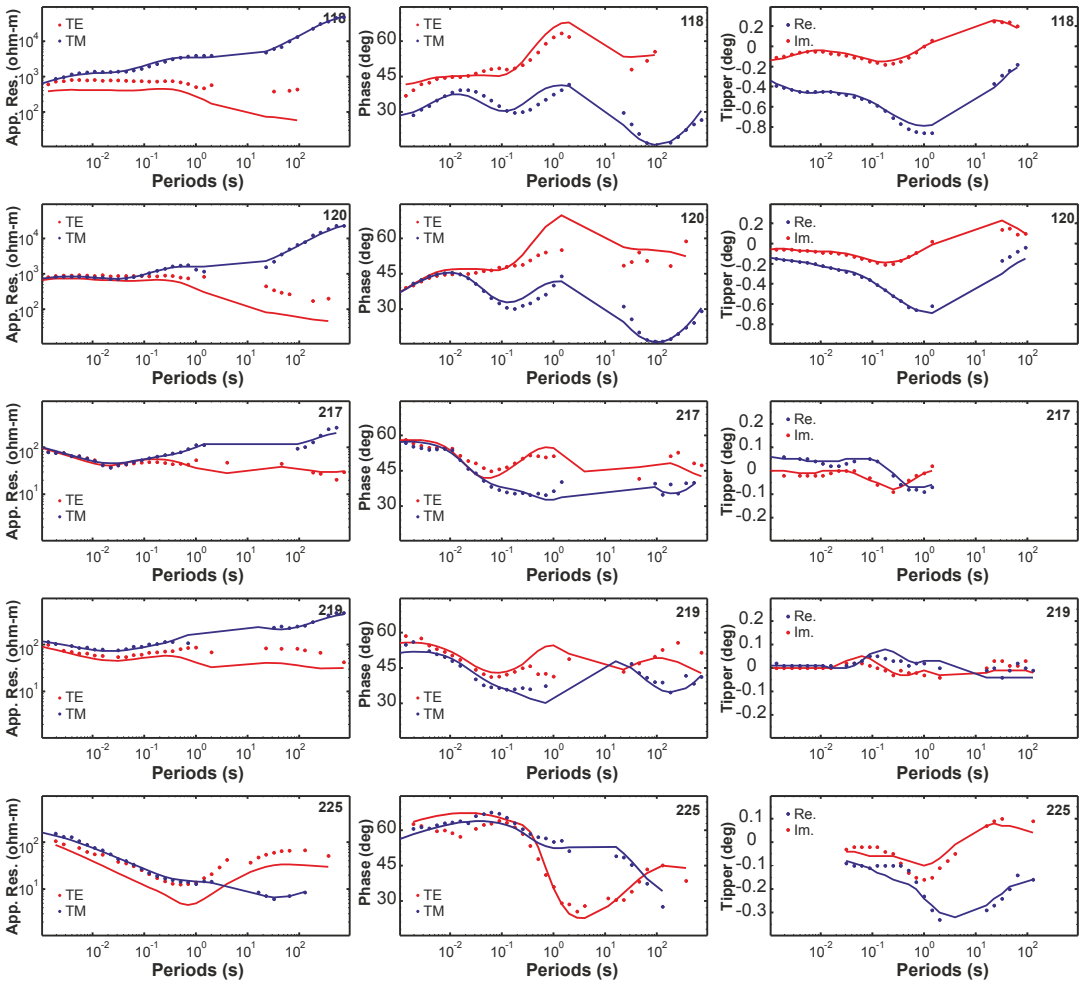

Figure 4.7: Measured data and 2-D responses at some exemplary sites which are displayed as apparent resistivity (left column), phase (middle column) and VTF (right column) curves. Dots are the field data. Lines are model responses. The resistivity and phase of the TM mode are better fitted than the TE mode, while real and imaginary components of VTFs are relatively well fitted. Measured data and 2-D responses of all sites are shown in Appendix E.

4.1.5 Sensitivity tests

The robustness of conductive features C2

To investigate the robustness of conductive feature C2, particularly the minimum depth extension, I performed a number of sensitivity tests. First, a 100 Ωm resistive half-space was inserted in the final inversion model of profile 2 (Figure 4.6 and Figure 4.8) at depths below 8 km. A new inversion with the deep resistive block being locked was started.

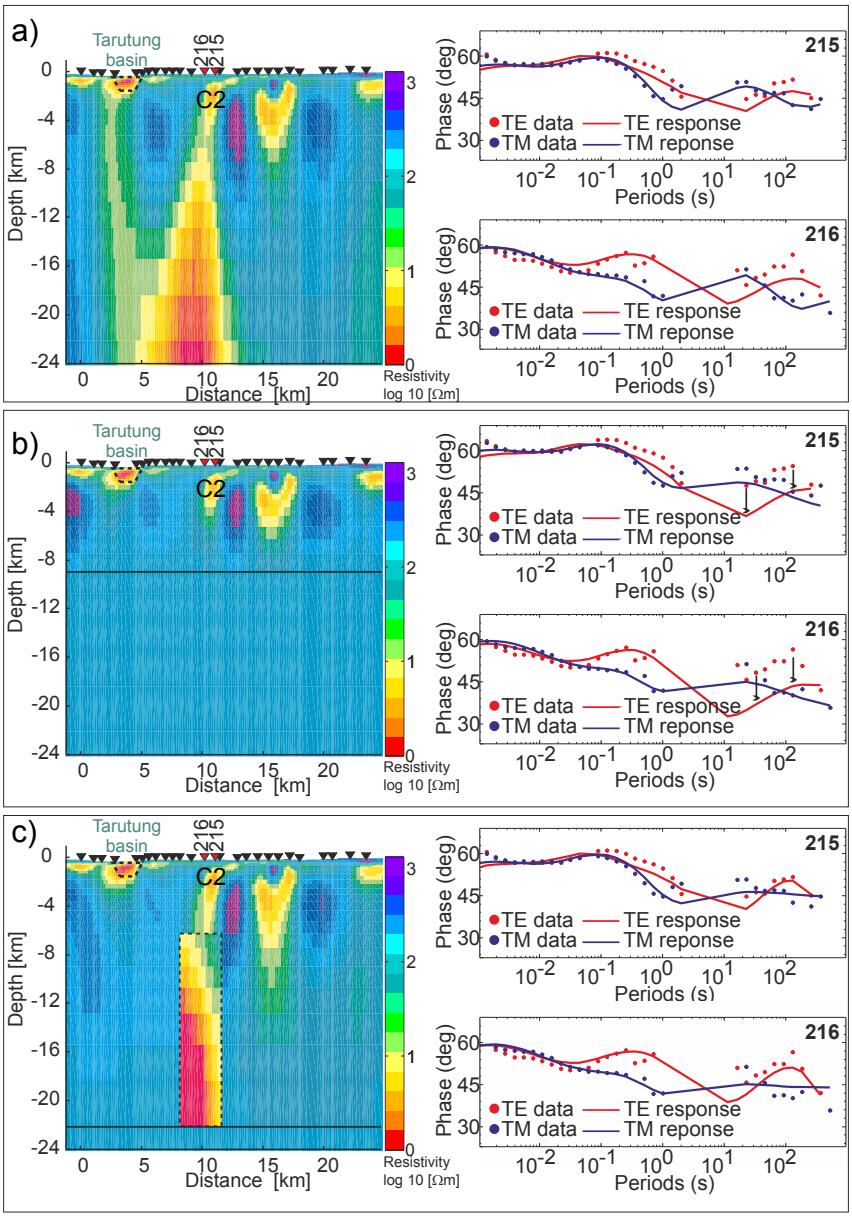

Figure 4.8: 2D resistivity model of profile 2 (see Figure 4.6 for location of the profile) and the phase curve responses of sites 215 and 216. a). Preferred inversion result of the profile 2 is the same as in Figure 4.6. b). A 100 Ωm half space at depths below 8 km was locked, so that only the upper part of the model could be altered by the inversion; the absence of the deep high conductivity feature causes a significant misfit at long periods, as indicated by black arrows. c). A constrained inversion with a 100 Ωm half space at depths below 8 km with a tear zone (dashed rectangle) was introduced in order to allow for strong resistivity contrasts. The model responses were close to the field data, which means that feature C2 is required by the data.

Some of the modelled sounding curves show a high data misfit, particularly long period data for sites near C2, such as site 215 (Figure 4.8b). The shallow part of C2 still appears, which indicates that the shallow conductor is required by the data, at least down to 4 km depth. The deeper part of C2 is not present in the constrained inversion, due to the influence of regularization. This constrained inversion model, however, does not fit the long period data (see Figure 4.8b).

For a second test, a 100 Ωm resistive half-space was inserted in the final inversion model of profile 2 (Figure 4.6) at depths below 8 km and along the conductor beneath the Panabungan hot spring. A new inversion with the deep resistive block locked below 22 km was started, but with a tear zone along the conductor beneath the Panabungan hot spring. The tear zone approach, included in the inversion code of Rodi and Mackie (2001) within the Winglink package, allows the user to define one or more regions of the model space where the regularization terms are calculated independent from each other, i.e. strong resistivity contrasts across the boundaries of the tear zones are not penalized by the regularization term.

In this scenario, the constrained inversion recovers a high conductivity region within the defined tear zone, representing the deeper part of C2 (see Figure 4.8c). The constrained inversion also shows that the upper and lower parts of C2 are separated by a region of moderate conductivity (Figure 4.8c). The modelled sounding curves were close to the field data, which are also similar to the responses of the preferred model (see Figure 4.8a). This implies that the deeper part of C2 is required by the data, and it is not an artifact conductor produced by inversion.

Data quality test

Some of the sites display data gaps up to one decade, mostly between 2 s and 20 s, due to the removal of noisier data (Section 3.2.2). Thus, a test was performed to examine the effect of data gaps in the inversion result.

The model responses of the inversion result of profile 2 (upper left panel in Figure 4.9) were used as synthetic data with the addition of 2 % random Gaussian noise. All data points in the dead band (1-10 s) were then removed from the synthetic data before another inversion was performed using 100 Ωm homogeneous half-space as a starting model.

All structures, such as shallow conductor beneath the Tarutung basin, are preserved, but show differences in the resistivity values of the conductive structures. The resistivity value of the shallow conductor beneath the Tarutung basin in the preferred model (upper left panel in Figure 4.9) reaches 1 Ωm, while the resistivity of this shallow conductor shows a resistivity of 5 - 10 Ωm. Furthermore, the deep reaching conductor C2 is still imaged. It suggests that the vertical conductor is a consistent and required feature despite of the data gap from 2 s to 20 s.

Examples of synthetic data and model responses are displayed (Figure 4.9), which are similar to the measured data and model responses in Figure 4.7. If the data at long periods are trustworthy, i.e. results of robust remote reference processing showing small error bars and low scatter, the 2-D inversion is capable of providing reliable models, even if data in-between (2-20 s) are missing.

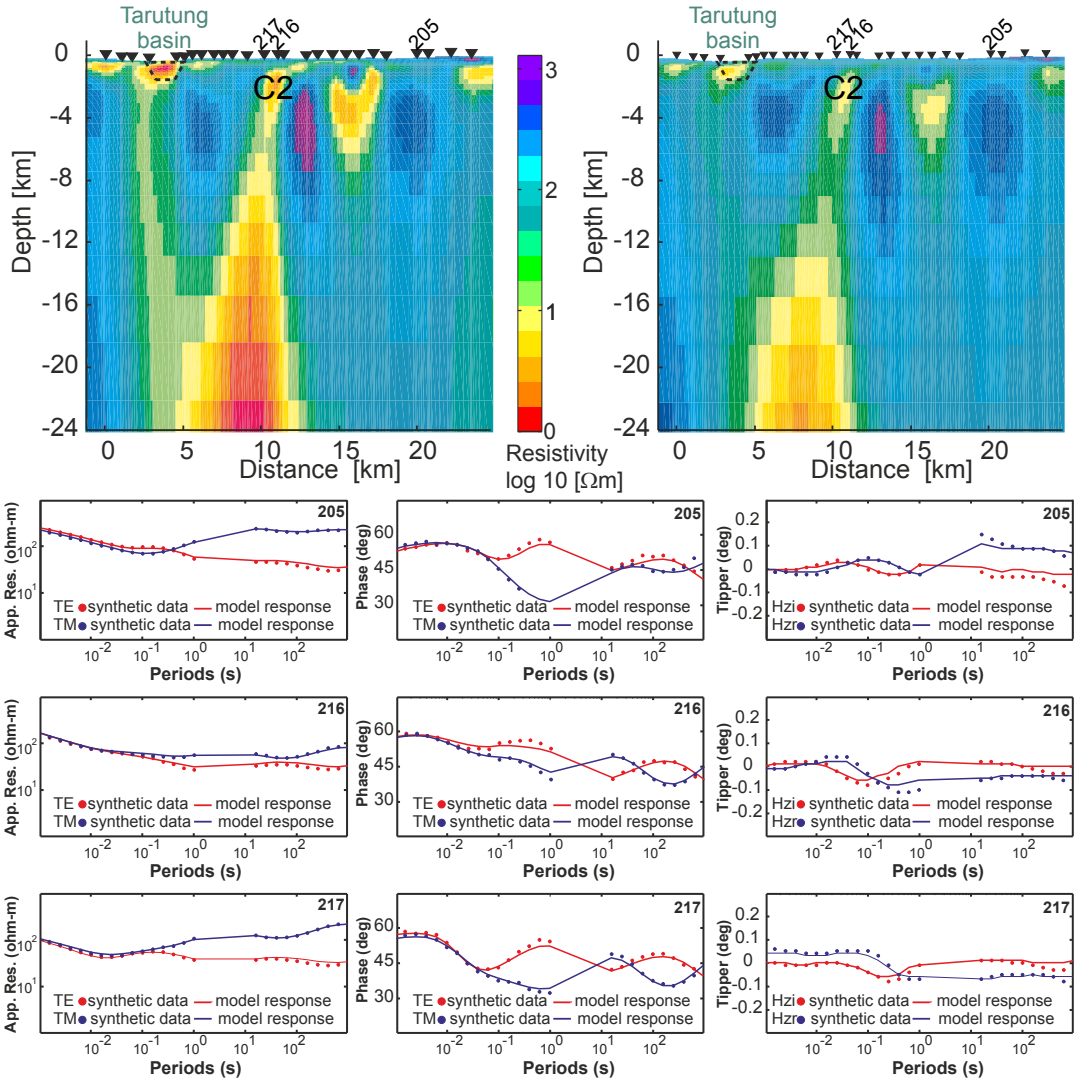

Figure 4.9: To mimic the effect of a data gap in the dead band (2 s - 20 s), the final model responses for profile 2 (see Figure 4.6) were used to generate synthetic data sets in which all data points in the period range 1 to 10 s were removed. The synthetic data were then inverted using the same parameters as for the preferred model, and the model in the right column was obtained. All major conductivity features are recovered with slightly different resistivity values.

4.2 3-D inversion

As mentioned before, some of the Sipoholon data display a 3-D character (see Section 3.2.3). Accordingly, 3-D inversion was carried out for the Sipoholon data set. The 3-D inversion results can provide further insight into the robustness of the structures and complement the 2-D inversion results. The results from 3-D inversion can also confirm whether the structures that resulted from 2-D inversion have off-profile limits or are connected between the profiles.

The Modular Electromagnetic Inversion system (ModEM, Kelbert et al., 2014, Egbert and Kelbert, 2012 and Meqbel, 2009) was applied to perform the 3-D inversion. MT data from 51 sites in the period range of 0.001-1000 s were inverted. A number of MT sites, i.e. 26 sites containing only impedance and 19 sites exhibiting very poor VTFs, were excluded from the 3-D inversion.

The 3-D Grid software package (Meqbel, 2014, Pers. Comm.) was used to configure a grid. The grid is divided into 80 $\times$ 80 $\times$ 40 cells (i.e. in x-, y- and z- directions, respectively). The total size of the grid is 200 km $\times$ 200 km $\times$ 367 km. The grid is comprised of core and padding cells (see Appendix B).

The core grid, containing the MT sites, consists of 60 $\times$ 60 cells with a horizontal size of 500 m $\times$ 500 m. The size of the padding cells increase horizontally by a factor of 1.5, starting from 500 m (in x- and y-directions). The vertical cell size increases by a factor of 1.2, starting from 500 m.

Similar to 2-D inversion (see Section 4.1), the observed data errors were not used in 3-D inversion of the Sipoholon MT data. The present study used an error floor of 5% of $|Z_{xy} * Z_{yx}|^{1/2}$ for off-diagonal impedance elements, 3% of $|Z_{xy} * Z_{yx}|^{1/2}$ for diagonal elements, and a constant value of 0.03 for VTFs. This choice is based on many other studies using the ModEM algorithm (e.g. Tietze and Ritter, 2013, which tested the influence of data weighting in data misfit).

Following Meqbel et al. (2014), it is important to select an optimal prior resistivity model that is near the average resistivity of the Sipoholon data. Two forward modelling tests for homogeneous half-spaces of 100 Ωm and 1000 Ωm resulted in starting misfits of 9 and 38, respectively. This indicates that a homogeneous half-space of 100 Ωm is closer to the average resistivity of the data. The inversion results at exemplary depths of both models are shown in appendix C, including data fit examples. It should be noted that the starting model does not take into account the Indian Oceanic. The trench is 250 km away from the study area (see Figure 3.1) and therefore outside of the defined grid.

In the 3-D inversion, the data and the model can be defined in a geographical coordinate system

or in a coordinate system aligned to particular geological strike of a study area. An example of the 3-D MT inversion using a geographical coordinate system is the resistivity study in the Rotokawa geothermal field, Taupo Volcanic Zone, New Zealand (Heise et al., 2008). In contrast, Wannamaker et al. (2013) rotated the data and the coordinate system to N40 °E for the inversion of the Dixie Valley MT data.

In this study, six separate inversions (see Table 4.2) were carried out to investigate the dependency of the inversion result on data component and grid rotation. All models used the same initial damping factor lambda $\lambda = 1$. The models also used the same starting model (and prior model, i.e. homogeneous half-space of 100 Ωm).

Table 4.2: Six different model schemes of the 3-D inversion used in this study.

Model's names	Data and grid rotation (deg)	Data sets
A	0	Full impedance
B	0	VTFs
C	0	Full impedance and VTFs
D	-36	Full impedance
E	-36	VTFs
F	-36	Full impedance and VTFs

The 3-D inversion of models A, B and C use a geographical coordinate system. The models D, E and F use a coordinate system which was rotated to N36 °W (i.e. the dominant strike direction, resulted from the impedance analysis, see Section 3.2.3). In the following Section, the term 'rotated data' applies to both the rotation of the data and the model grid. In order to make the visualization easier (i.e. to compare with the models A, B and C), the horizontal sections of model results D, E and F were rotated back to 0 °. Hence, 'up' points northward (see appendix D).

4.2.1 Analyses of inversion model results

The inversion result of models A, B and C (i.e. using the geographical coordinate system) are consistent with the inversion result of models D, E and F (i.e. using the rotated coordinate system), showing similar structures on each depth slice (Figures 4.10 and 4.11). This indicates that data rotation is not crucial for 3-D inversion of the Sipoholon MT data.

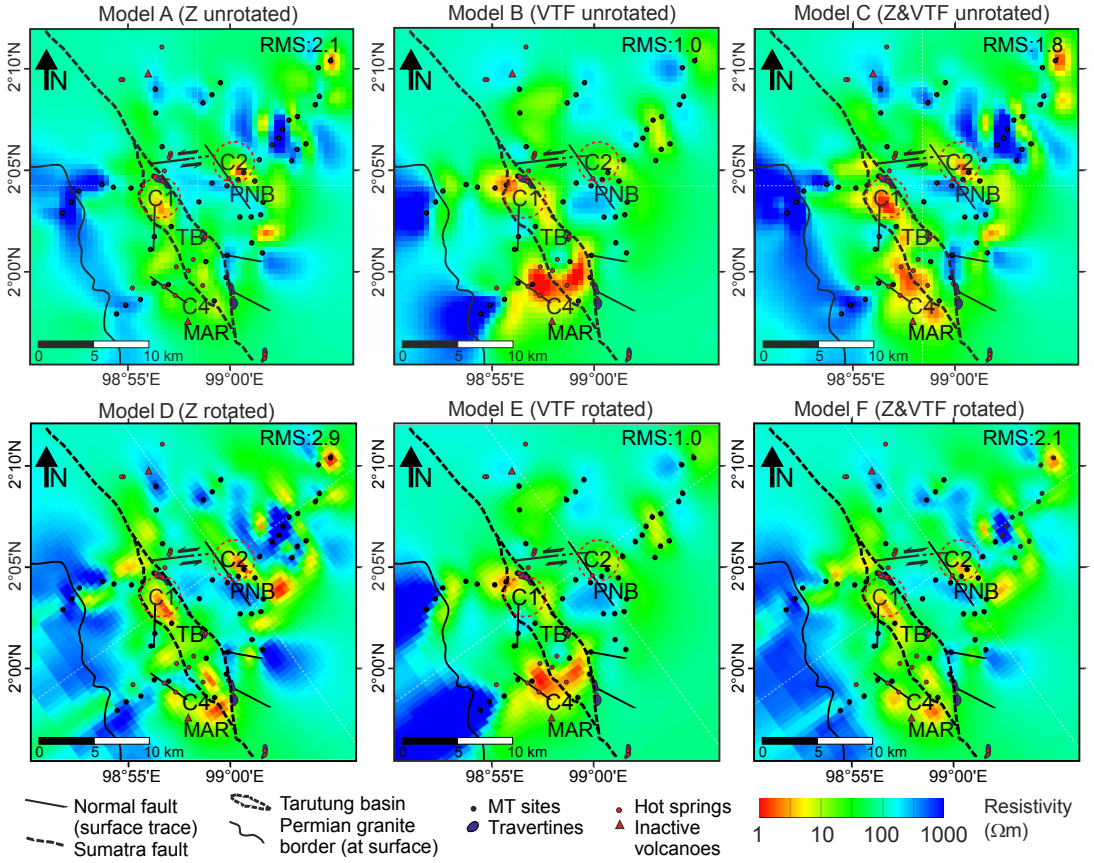

Figure 4.10: Horizontal sections at a depth of 1 km from six separate 3-D inversion results (see Table 4.2). Conductive structures are labelled with a "C". These conductive structures include a shallow conductor (C1), which corresponds spatially with the Tarutung basin (TB), and a conductor (C2), which appears to be close to the Panabungan (PNB) hot spring and the PNB normal fault. All models resulted in similar major structures but different resistivity values of the structures.

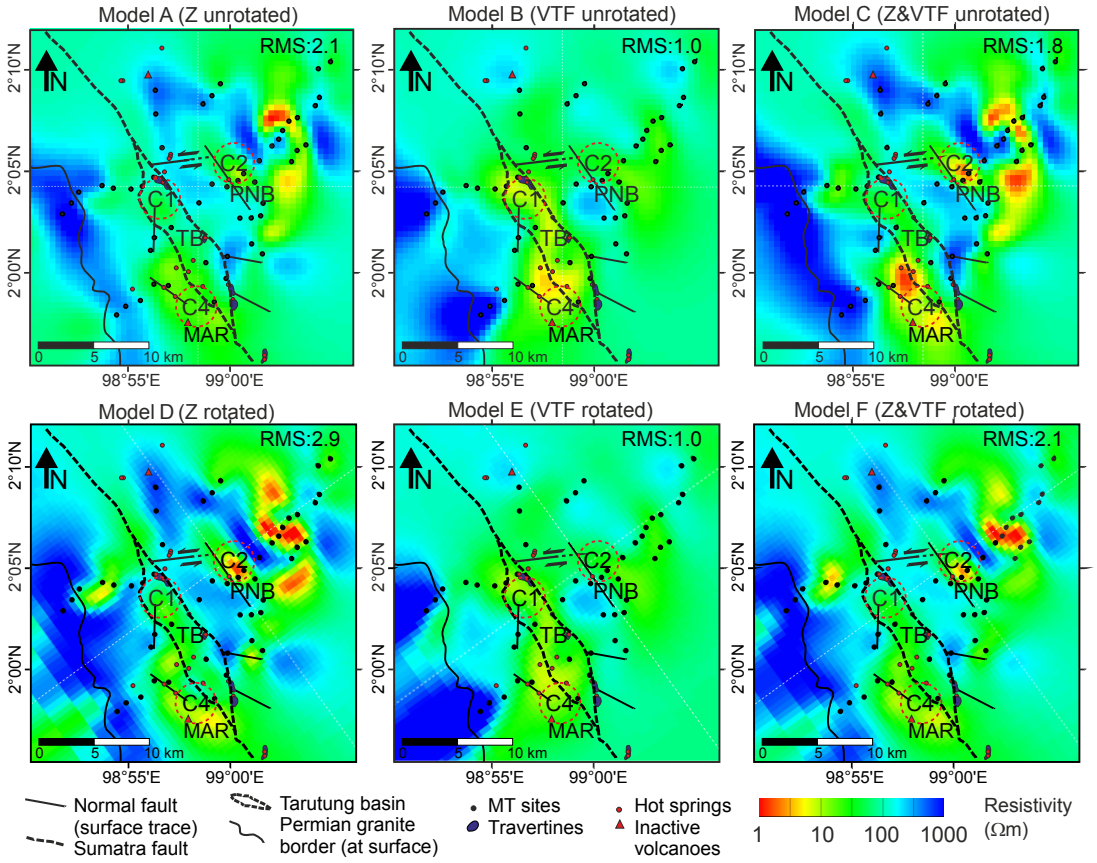

Figure 4.11: Horizontal sections at a depth of 2 km from six separate 3-D inversion results (see Table 4.2). Labels are the same as in Figure 4.10. The conductor C2 is clearly present in models C and D. This indicates that the data rotation gives similar effect with additional information brought by the (un-rotated) VTFs, particularly at long periods.

A shallow conductive anomaly (C1) is present beneath the TB at a depth of 1 km (Figure 4.10). A deep reaching conductive anomaly (C2, which includes the conductive anomaly C3 from 2-D inversion) is revealed and is located around the PNB hot spring and the PNB normal fault (Figures 4.10 and 4.11). Another shallow conductor (C4) is imaged beneath some hot springs, located to the north of the inactive Martimbang (MAR) volcano.

The difference between each model is the conductivity contrast. For example, at a depth of 2 km (Figure 4.11), the conductor C4 is image clearly in model C (using unrotated impedances and VTFs). The other models show less obvious conductivity contrast between the conductor C4 and its surrounding.

In the geographical coordinate system, it is expected that the conductors C1 and C4 exhibit lower resistivity (or higher conductivity, $\rho = 1/\sigma$) values in model C than in model A (Figure 4.10). Similarly, at a depth of 2 km, the conductor C2 displays lower resistivity values in model C than in model A (Figure 4.11). However, this is not the case for the rotated coordinate system. At a depth of 2 km, the conductor C2 shows higher resistivity values in model F (using rotated impedances and VTFs) than in model D (Figure 4.11).

Another difference between each model is the total misfit, as indicated in upper right corner of each panel in Figure 4.10 or 4.11. Model D (using rotated impedances) exhibits higher misfit than model A (using un-rotated impedances). Model F (using rotated impedances and VTFs) also displays higher misfit than model C (using un-rotated impedances and VTFs). The misfit differences can be seen more detail in the distribution of RMS misfit for all sites.

All sites exhibit higher impedance misfits in Figure 4.12a than in Figure 4.12d. Misfit of VTFs for model F is also higher than for model C than for model F (Figure 4.12g). It should be noted that Figures 4.12c and f show the total misfits, consisted of impedances and VTFs misfits (Figure 4.12g). As expected, impedances or VTFs are better fitted by themselves (Figure 4.12a or b as well as d or e) than by joint inversion (Figure 4.12g).

In terms of lateral misfit distributions between the MT sites located to the east of the TB and to the west, impedances misfit displays similarities (e.g. Figure 4.12a or d). In contrast, the VTFs misfit distributions show lower misfit for the MT sites located to the east of the TB (e.g. site 217) than the MT sites located to the west (e.g. site 120).

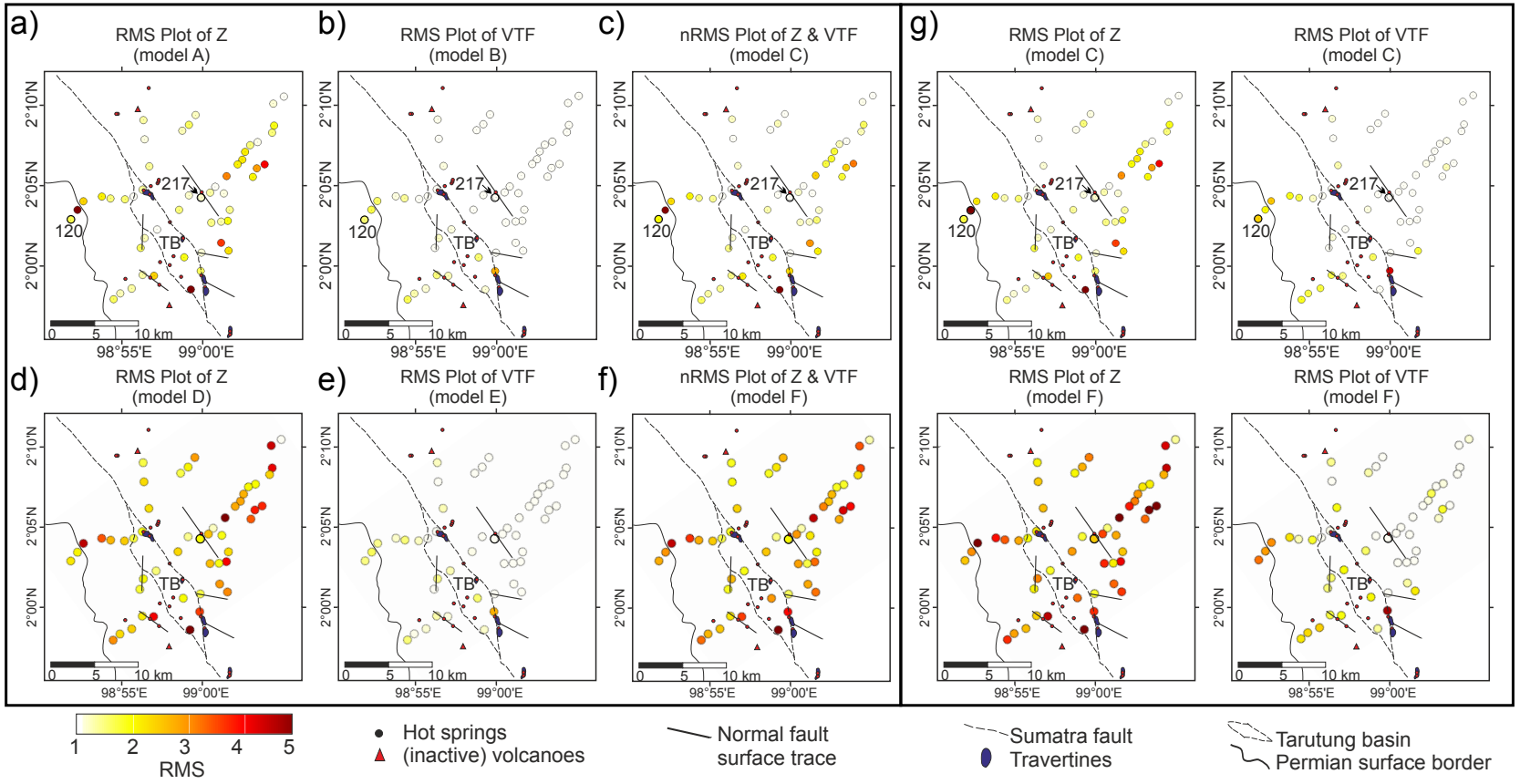

Figure 4.12: Distribution of RMS misfit for all sites and for all periods of models A-F. MT sites are marked by circles with color indicating the RMS misfit. This figure shows that the misfits of the rotated impedances (d) are higher than the un-rotated impedances misfits (a). The misfit of VTFs is similar between un-rotated (b) and rotated (e) models. To notify, the total misfits of models C and F consist of impedances and VTFs misfits (g).

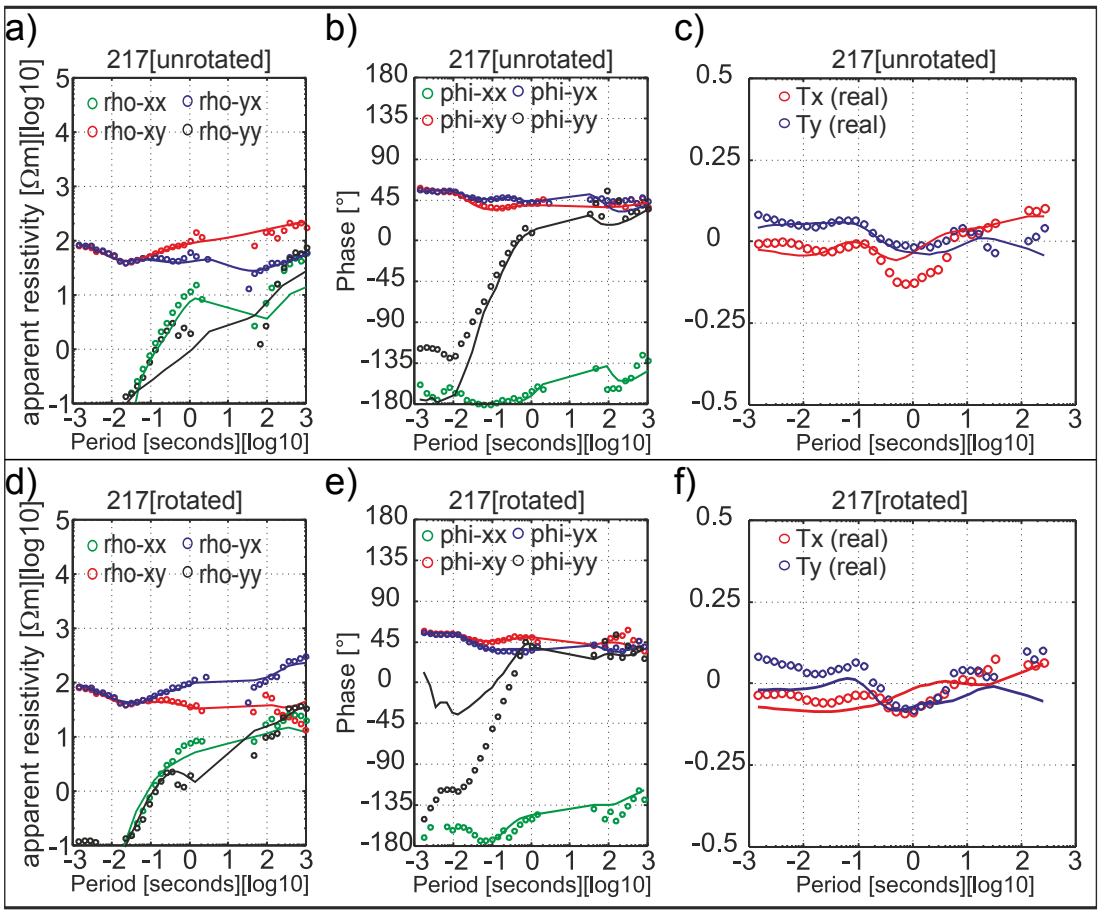

Figure 4.13: Upper row (a-c): Un-rotated data (circles) and model responses (solid lines) of site 217 from the inversion of model C (i.e. using un-rotated impedances and VTFs) shown in Figures 4.10 and 4.11. Lower row (d-f): data fits of site 217 for models F (i.e. using rotated impedances and VTFs). This figure shows that data rotation aligned to geo-electric strike direction resulted in a greater split of xy- and yx- components, as well as real Tx- and Ty-components. However, the MT sites in the eastern area of the TB display less pronounced of the separation between these components than the MT sites in the western area of the TB (see Figure 4.14).

The splitting between xy- and yx-components (i.e. at long periods) is bigger when the data are aligned with the geo-electric strike direction (i.e. -36 ° for the Sipoholon data). However, the inversion cannot fit these rotated data, as indicated by worse data fit after rotation (Figure 4.13d) than before rotation (Figure 4.13a). Similarly, real Ty-components also exhibits worse data fit after rotation (Figure 4.13f) than before rotation (Figure 4.13c).

Site 120 (see Figure 4.12 for the site location), displays bigger splitting of xy- and yx- components compared to site 217. It can be seen that real Tx- and Ty- components are not well fitted. It is likely that the inversion has difficulties to fit the rotated VTFs because of this big splitting of real Tx- and Ty- components, particularly at 1 s. However, this unfitted data is present only at sites located to the west of the TB and in the inversion result of model F (see Figure 4.12g).

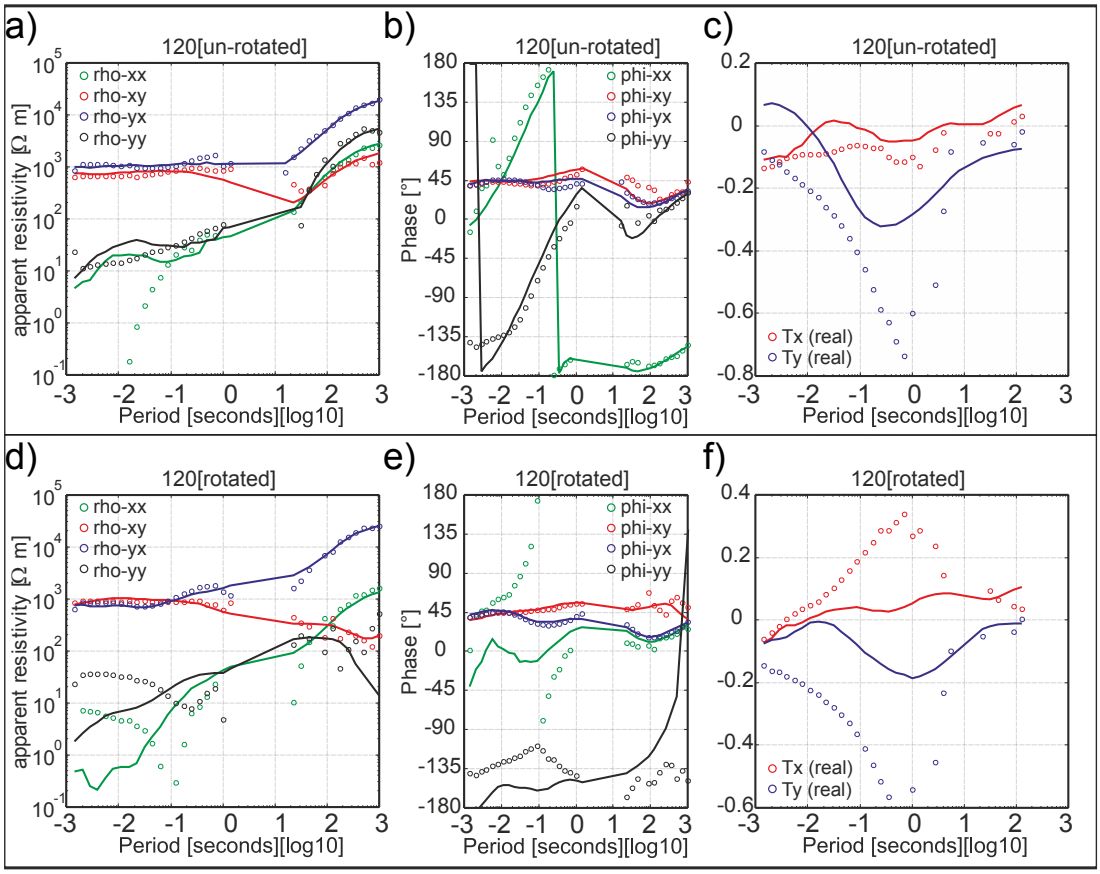

Figure 4.14: Upper row (a-c): Un-rotated data (circles) and model responses (solid lines) of site 217 from the inversion of model C (i.e. using un-rotated impedances and VTFs). Lower row (d-f): data fits of site 217 for models F (i.e. using rotated impedances and VTFs).This figure also shows that data rotation aligned to geo-electric strike direction resulted in bigger splitting and worse data fits, particularly between real Tx- and Ty- components.

The preferred 3-D model is inversion result of model C, exhibiting a total misfit of 1.8. There is no dependency of the inversion result on data component and grid rotation. All models display similar structures. Model C produced adequate agreements with other studies, such as geological, geochemical and micro-seismic studies (Figure 4.20 in Section 4.3). Furthermore, in general, inversion of un-rotated data resulted in lower misfits than inversion of rotated data.

4.2.2 Sensitivity test

The most striking structure from the 2-D inversion is the deep reaching conductor C2 (Section 4.1.4). Both preferred and constraint inversions show that this conductor extends more than 10 km depth and consists of shallow and deeper parts (Figures 4.6 and 4.8c). However, the preferred 3-D inversion as well as other models does not reveal the deeper part of the conductor C2.

In this Section, two sensitivity tests to check the extent and robustness of the conductor C2 is presented. This conductor C2 also appears in the 3-D inversion result. First, the inversion result of model C was modified by inserting a resistive block of 100 Ωm in a size of 3 km × 3 km × from surface to a depth of 10 km (small dashed red rectangle at C2 in Figure 4.15). The forward responses (orange lines in Figure 4.16) are away to the field data. This can be an indication that the conductor C2 is needed by the data.

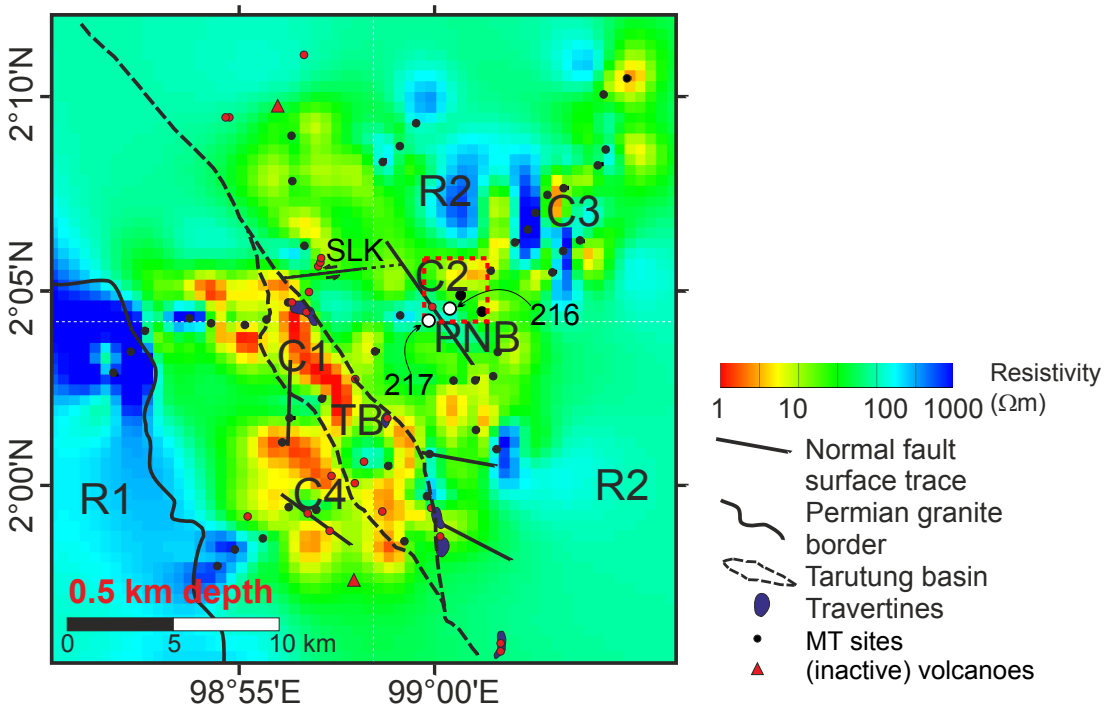

Figure 4.15: Horizontal sections from the 3-D inversion result of model C at a depth of 0.5 km. SLK indicates both the Silangkitang sinistral sealed fault and the Silangkitang acidic hot springs. PNB refers to both the Panabungan normal fault and the Panabungan neutral hot spring. Red dashed rectangle mark area where 100 Ωm resistive or 10 Ωm block were inserted for sensitivity tests. Two black circles inside the red dashed rectangle marks location of sites 216 and 217.

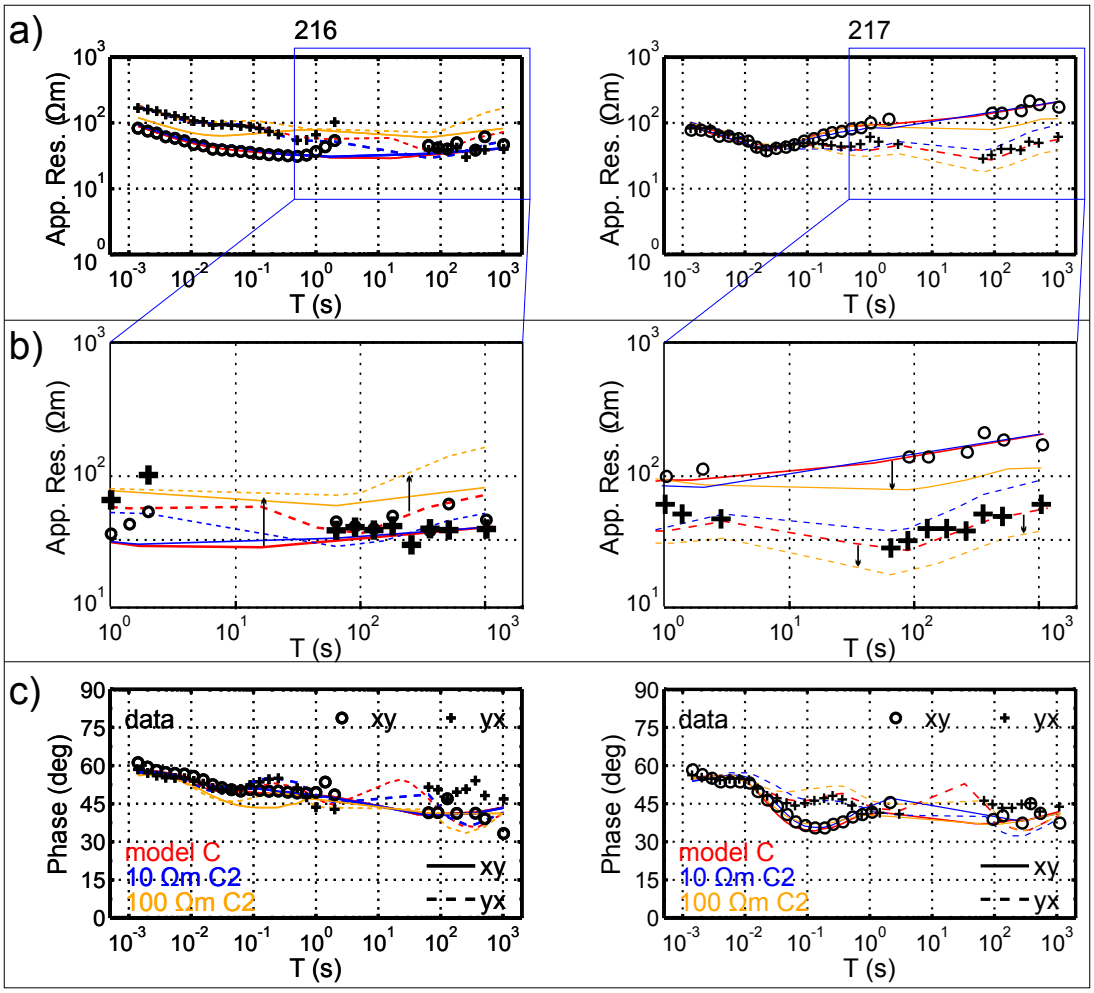

Figure 4.16: Un-rotated observed data (symbols) and model responses (lines) of sites 216 (left column) and 217 (right column), which are displayed as apparent resistivity (a and b- Zoom-in of apparent resistivity between 1 s and 1000 s) and phase (c). The red lines indicate the model responses of model C (i.e. the preferred model using un-rotated impedances and VTFs). The blue and orange lines indicate the responses of the modified model by inserting 100 Ωm resistive or 10 Ωm conductive block, respectively, in the red dashed rectangles area (Figure 4.15). The forward responses of first test (orange lines) shifted away from the data, particularly for yx-components at long periods. The forward responses of second test also display differences for yx-components. However, both blue and orange lines show significant differences in the period band with no data (as indicated by black arrow). This indicates that the maximum extend of conductor C2 is not well resolved.

For a second test, the inversion result of model C was modified by inserting a block of 10 Ωm in a size of 3 km × 3 km × from from surface to a depth of 10 km (small dashed red rectangle in Figure 4.15). The forward responses of xy-components (blue line) are similar to the field data and the inversion responses (red line), while yx-components exhibit small differences from the two responses (as indicated by red and blue dashed lines) in the period band with no data (i.e. due to removal of outliers in the dead band periods, see Section 3.2.2). It seems that data gaps in the dead band resulted in bigger problem in 3-D inversion than in 2-D inversion. Therefore, the maximum extend of conductor C2 is not well resolved in the 3-D inversion, including the sensitivity tests.

4.2.3 Comparison of the 2-D and 3-D inversion results

Figure 4.17 displays cross sections of 3-D inversion result of model B along four profiles, including 2-D inversion results for comparison. Both 2-D and 3-D models show similar structures, e.g. four conductors (labelled as C1, C2, C3 and C4). However, the 2-D and 3-D models show different depth extents of the structures. For example, the 2-D models show that the conductor C2 reaches depths of at least 20 km, while this conductor (C2) is imaged only to depths of approx. 5 km in the 3-D model.

Two resistors (labelled as R1 and R2) appear in all profiles. Resistor R1 is located to the west of the TB, while resistor R2 is situated to the east of the TB. Although both resistors R1 and R2 display resistivity values above 100 Ωm, the structure R2 exhibits in general lower resistivity values than the R1, particularly along profile 3 in Figure 4.17.

Profiles 2 and 3 show the conductor C1, beneath the TB. The conductors C2 and C3 are also present along profiles 2 and 3 (Figure 4.17). Both conductors C2 and C3 exhibit a resistivity value below 37 Ωm (see Section 4.3 for explanation of this selected value).

Both 2-D and 3-D inversion results along profile 4 (Figure 4.17) display the conductor C4. However, the resolution beneath the Martimbang volcano is poor for both 2-D and 3-D inversions. The number of sites along profile 4 in the 2-D inversion is six sites only. In the 3-D inversion, sites 406 (which was set up at the flank of the inactive Martimbang volcano) and 407 were excluded due too poor data quality, e.g. the VTF data are noisy at all period ranges.

Although 3-D results generally display shallower extents of the structures, 3-D inversion better controls structures in off-profile area. In the horizontal section at a depth of 0.5 km (Figure 4.15) or 1 km (Figure 4.10), the conductor C4 appears to be spatially correlated with a cluster of hot springs and the surface trace of a normal fault rather than with the inactive Martimbang volcano.

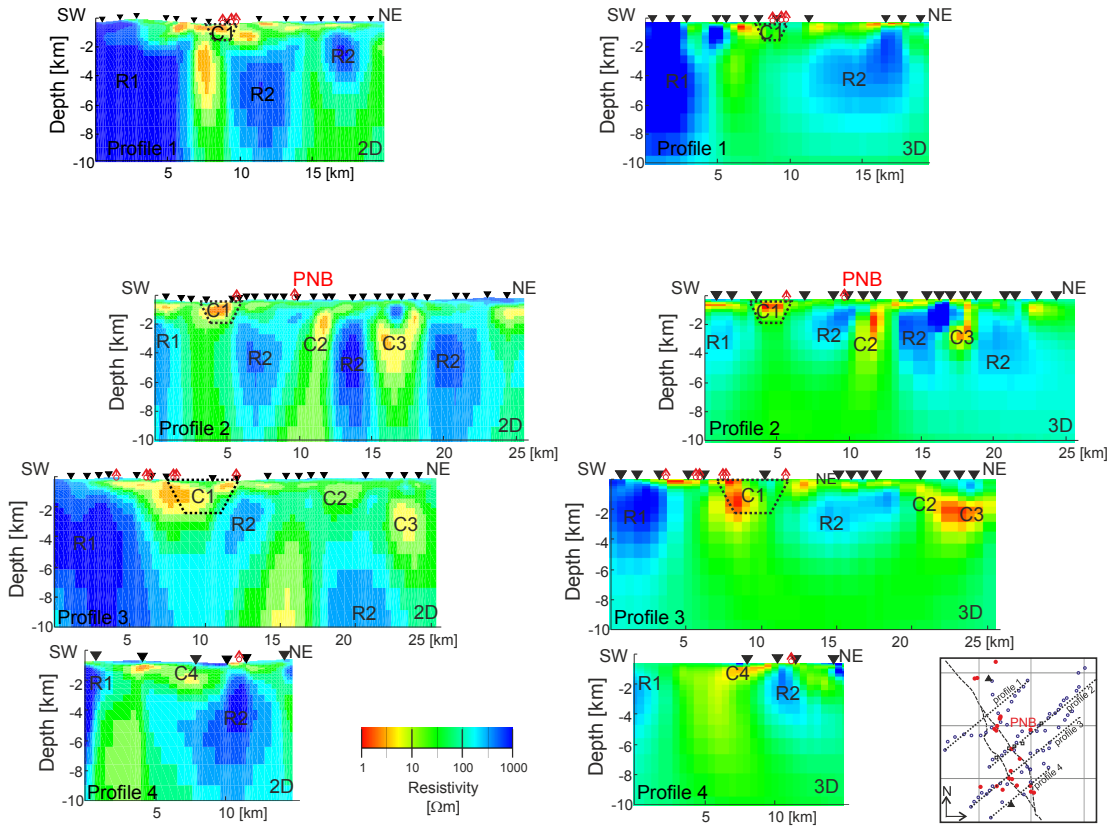

Figure 4.17: Cross sections from 2-D (left) and 3-D (right) inversions results. The black triangles indicate MT stations. Red arrows indicate hot spring locations. Conductive features are labelled with C, resistive features with R. No vertical exaggeration on the resistivity models. Both 2-D and 3-D inversion results show similar structures, such as the conductor C1 beneath the Tarutung basin (marked by the black-dashed trapezium). All profiles also display the resistors R1 and R2 in the SW and in the NE, respectively. However, the structures from the 2-D inversions are more elongated vertically than the 3-D results.

4.3 Discussion of the inversion results

The resistivity distribution can be analysed and interpreted as geological units in the study area, including the porosity and the possibility of fluid fill in the rock pores. The interpretation of these electrical conductive or resistive structures is based on both 2-D and 3-D inversion results. Vertical extents of the structures are determined from the 2-D results, while horizontal extents of the structures are resolved by the 3-D inversion. Furthermore, other geophysical as well as geochemical studies provide complementary information about the subsurface resistivity distribution.

As mentioned at the end of Section 4.2, both 2-D and the 3-D inversions resulted in similar structures: two resistors R1 and R2 and four conductors C1, C2, C3 and C4. In the following section, the term conductor C2 applies to both conductors C2 and C3. According to the 3-D inversions, these conductors (C2 and C3) are connected spatially, particularly at a depth of 2 km (Figure 4.20).

4.3.1 Electrical conductivity structures

Resistive structure R1

The resistor R1 appears consistently in the southwestern part of all profiles (Figure 4.17). Horizontal extent of the resistor R1 coincides spatially with the boundary between the Permian granites and the Miocene andesites in the western part of the study area (Figure 4.20). At surface, the Permian granites show a very low porosity (Nukman and Moeck, 2013). There is no indication of geothermal surface manifestation above Permian granite or of any faults (Nukman, 2014). Therefore, the resistor R1 is interpreted as impermeable Permian granites.

The resistor R1 correlates with a high magnetic anomaly region (Situmorang, 2005). However, the regional gravity anomaly in the southwestern part of the study area is relatively lower than in the northeastern part of the study area (Figure 3.5). This particular circumstance, i.e. the high magnetic anomaly coinciding with the low density anomaly and the high resistivity anomaly, is also found in the Taupo Volcanic Zone, New Zealand (Heise et al., 2007; Soengkono, 2011).

Resistive structure R2

Nukman (2014) suggests that the lithology in the eastern part of the Tarutung basin (TB), is weaker than the lithology in the western part of the TB. There are more faults in the eastern part from the TB than in the western part (Figure 3.2). This is in agreement with the MT inversion

results, which show that the resistivity of the structure R2, located in the eastern part of the study area, is in generally lower than the R1 (Figure 4.20).

At surface, resistor R2 corresponds with Miocene andesitic rocks (Figure 3.3 and Figure 4.20). The resistor R2 also coincides with a high Vp value and a low Vp/Vs ratio (Muksin et al., 2013). High Vp values, together with low Vp/Vs ratios, indicate low porosity of rocks. Accordingly, the resistor R2 can be interpreted as Miocene andesite with small primary porosity, which does not contain a significant amount of fluids.

Conductive structure C1

A conductive structure (C1) shows a resistivity < 10 Ωm, which appears consistently along profiles 1, 2, and 3 and coincides spatially with the TB (Figure 4.17). The 2-D inversion result of profile 1, crossing the northern edge of the TB, displays a depth of 1.5 km. Conversely, the 3-D result along the profile 1 does not show any conductive structure < 10 Ωm beneath the TB. Along profiles 2 and 3, the structure C1 is present in both 2-D and 3-D inversions and extends down to a depth of 2 km.

According to the surface geological mapping (Nukman and Moeck, 2013), the TB is bordered by at least two permeable normal faults. These faults provide pathways for (meteoric) surface water to flow into the TB until the base of the TB (i.e. impermeable rocks). The base of the TB is indicated by a resistive anomaly (> 10 Ωm), which coincides with a high Vp value (3.5 km/s) at a depth of 2.5 km mapped by Muksin et al. (2013). Accordingly, the permeable normal faults could also create pathways for mixed meteoric and magmatic water to flow up the surface and manifest as hot springs along the border of the TB (Figure 3.2).

The conductor C1 is interpreted as unconsolidated alluvium deposits, originating from the higher terrains east and west of the TB, including volcanic sedimentary rocks (such as the Holocene Toba Tuff). Accordingly, these unconsolidated sedimentary rocks with high porosity could be filled by fluids, as indicated by the hot springs along the edge of the TB.

Conductive structure C2

The most striking structure resulting from the 2-D and 3-D inversions is the vertical conductor C2, which appears consistently along profiles 2 and 3 (Figure 4.17). The conductor C2 is close to the locations of the Panabungan (PNB) hot spring and the PNB fault. At a depth of 2 km, the conductor C2 exhibits the lowest resistivity, i.e. 3 Ωm in the 2-D result and 1 Ωm in the 3-D result. Constrained 2-D inversion and 3-D forward modelling confirmed the robustness of this structure.

An empirical relationship by Archie (1942) (equation 2.1, see Section 2.2) was used to calculate the electrical resistivity (ρ) of structure C2. It should be noted that the modification of Archie's law by Caldwell et al. (1986) was not used due to the absence of the alteration mineral at surface (i.e. mapped by Nukman and Moeck (2013)). A porosity (ϕ) value of 10% was used for the calculation. This value based on the laboratory measurement on surface rock samples of the Miocene andesite around the Panabungan hot spring (Nukman, Pers. Comm., 2013).

For the case of a liquid dominated system, such as the Sipoholon geothermal field (Hochstein and Sudarman, 1993; Nukman and Moeck, 2013), water saturation (S_w) of the geothermal reservoir is at least 80% (Williams et al., 2011). Following Caldwell et al. (1986); Ussher et al. (2000), the saturation exponent (*n*) and a constant (*a*) are assumed as one, and the cementation factor (*m*) is often between one (i.e. for unconsolidated rocks) and two (i.e for consolidated rocks). The fluid resistivity values between 0.03 and 3 were assumed from Ucok et al. (1980), based on the salinity of the surface fluid samples from the hot springs (Nukman, 2014, Pers. Comm.). These values used for the calculation of the electrical resistivity are summarised in Table 4.3.

Table 4.3: Parameters used for the calculation, including the references used

Parameters	Values	References
a and n	1	Caldwell et al., 1986; Ussher et al., 2000
ρ_w	0.03-3	Ucok et al., 1980; Ussher et al., 2000; Nukman, 2014, Pers. Comm.
ϕ	0.1	Nukman, 2014
m	1-2	Caldwell et al., 1986; Ussher et al., 2000
S_w	0.8	Hochstein and Sudarman, 1993; Williams et al., 2011

The calculation using Archie's law (i.e. $\rho = a\ \rho_w\ \phi^{-m}\ S_w^{-n}$) resulted in a resistivity range of 3-37 Ωm (as indicated in a red transparent rhombus in Figure 4.18). The lowest resistivities of the conductor C2 derived from both 2-D and 3-D inversions is 3 Ωm and 1 Ωm, respectively. This is in agreement with the lowest resistivity resulted from the calculation (i.e. 3 Ωm).

However, this calculation is a rough estimation. There is a possibility that the resistivity is lower than 37 Ωm, if the fluid resistivity at depths is lower than 3 Ωm due to higher salinity and temperature. This resistivity value (37 Ωm) was used as the upper limit value of the conductor C2, indicating a region of permeable rock filled by hot saline fluid.

By using the highest value (i.e. 37 Ωm) as a contour surface in the 3-D result (Figure 4.19), the model shows that the vertical conductor, C2, extends and merges beneath the TB, as suggested by Nukman (2014). A resistivity contour using this value corresponds to a low Vp value and high Vp/Vs ratio as well as low Qp value found by Muksin et al. (2013) (Figure 4.20).

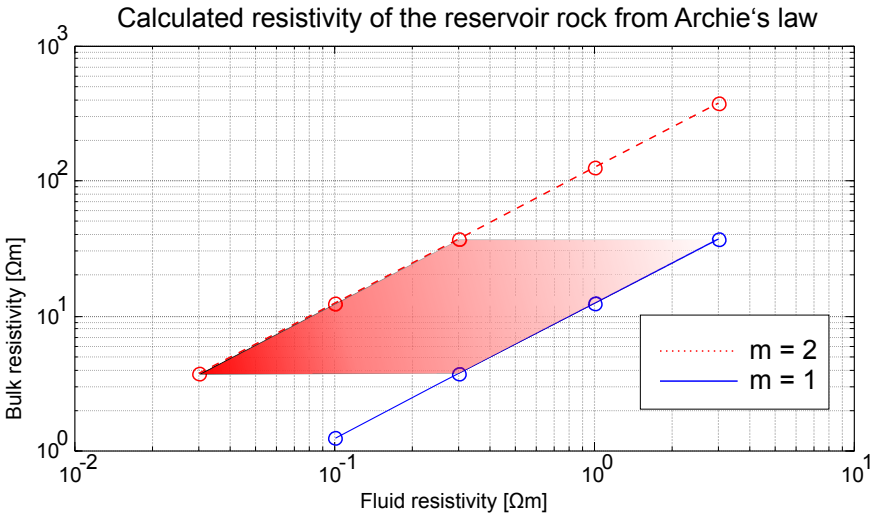

Figure 4.18: Calculated bulk resistivities of rocks (in Ωm) using Archie's Law. Variation of fluid resistivities (0.03-3 Ωm) were assumed from Ucok et al. (1980), based on the salinity of the surface fluid samples from the hot springs (Nukman, 2014, Pers. Comm.). 10% of porosity is an average porosity of surface rock samples around the PNB hot spring (Nukman and Moeck, 2013). 80% water saturation was assumed from Hochstein and Sudarman (1993); Williams et al. (2011). Accordingly, the cementation factor (m) is often between one (i.e. for unconsolidated rocks) and two (i.e for consolidated rocks).

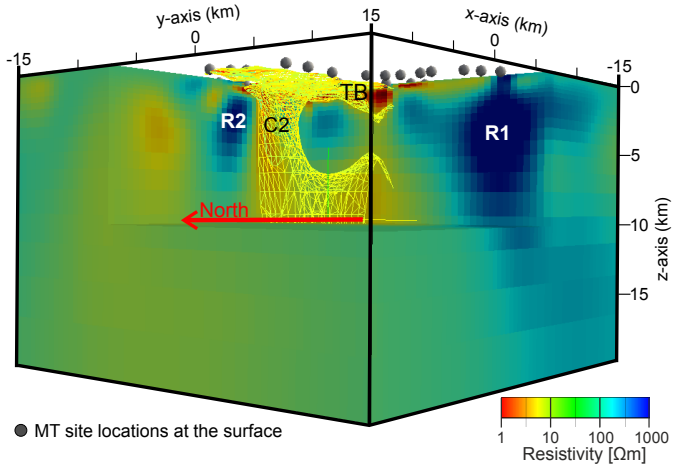

Figure 4.19: 3-D inversion result of model B viewed from the north-west. Red arrow points northward. A 3-D view of the conductor C2, indicated by the 37 Ωm resistivity cut-off (yellow wire-frames), shows that this conductor is dipping to the west and merges with the Sumatra fault beneath the TB, as suggested by Nukman (2014). Conductor C2 is located between two resistors: R1 and R2.

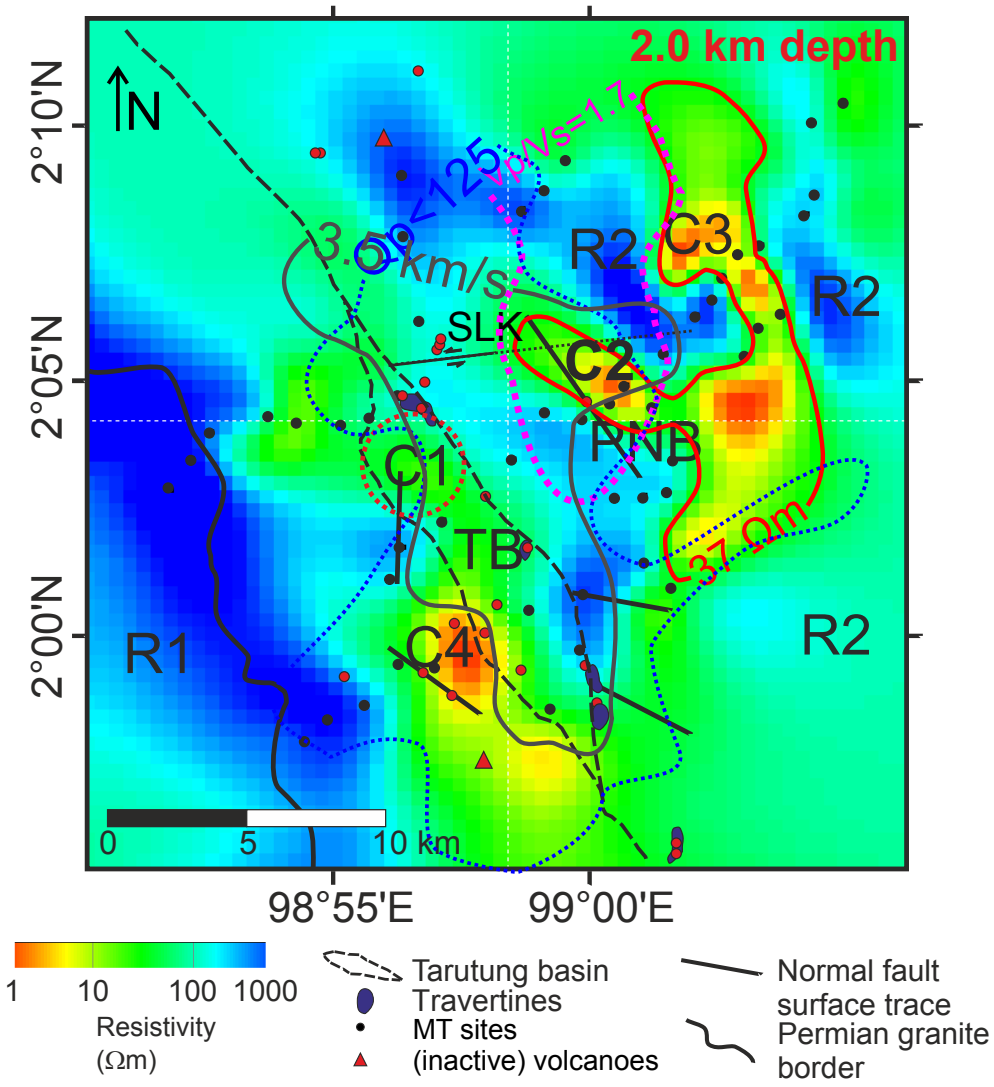

Figure 4.20: Horizontal sections from the 3-D inversion result of model C at a depth of 2 km. A contour of 37 Ωm was obtained from a calculation using Archie's law. SLK designates both the Silangkitang sinistral sealed fault and the Silangkitang acidic hot springs. PNB refers to both the Panabungan normal fault and the Panabungan neutral hot spring. This figure shows that the 37 Ωm contour, being a resistivity cut off of the conductor c2, corresponds to a low Vp value (grey line), a high Vp/Vs ratio (pink dashed line) and a low Qp value (blue dashed line). All these parameters are overlaid each other in the vicinity of the PNB and consistently indicate the presence of porous rocks filled by fluids.

Figures 4.17 and 4.19 show that in terms of electric resistivity distribution, a volcanic geothermal system displays a difference character compared to a non-volcanic geothermal system. In the volcanic geothermal system, the reservoir is characterised by resistive anomaly (i.e. due to illite occurences, see Section 2.2), which is present below a conductive layer (i.e. due to smectites). In the Sipoholon non-volcanic geothermal system, where the reservoir temperatures are most likely between 85 and 115 $^{\circ}$C (Nukman, 2014), there are no hydrothermal alteration rocks at surface. The vertical conductor C2 should not be interpreted as a smectite occurrences above the geothermal reservoir.

The vertical extension of conductor C2 is interpreted as a convective model of heat transport of hot water beneath the hot springs. To maintain convection, cold meteoric water is required to flow into the system. The conductor C2 exhibits the lowest resistivity at 2 km depth. The uppermost zone could be related to fluid pathways along faults. The fluid pathways would provide the means for surface water reaching down to greater depths. Accordingly, the fluid pathways also allow hot water from deeper levels to flow upward to the surface manifestations (e.g. the PNB hot spring).

The lowest resistivity of structure C2 at a depth of 2 km may be associated with a reservoir-like structure, i.e. due to the highest porosity and possibly permeability. This interpretation is supported by a low Vp, a high Vp/Vs ratio and a low Qp anomaly at a depth of 2 km (Figure 4.20), located around the Panabungan hot spring (Muksin et al., 2013). These anomalies were interpreted as porous rocks with hot and high fluid content (Muksin et al., 2013).

The deepest parts of conductor C2 could be associated with deep circulating fluids, which would act as heat source for the reservoir. Geochemical analyses of isotope ratios of Oxygen 18 and deuterium (δ) (Ardiwinata et al., 2005; Nukman, 2014) suggest that the hot springs in the eastern area of the basin contain up to 10% of magmatic water (i.e. the water originating from a mix of magma released fluids) and surface water.

Figures 4.19 and 4.20 also indicate that the conductor C2 is bordered by part of the resistor R2 to the north, which coincides with the Silangkitang (SLK) strike slip fault. The SLK fault is filled by fine quartz and acts as a fluid barrier (Nukman and Moeck, 2013; Nukman, 2014). This clarifies why the conductor C2 does not appear along profile 1 in both 2-D and 3-D inversions. This also shows the advantage of the 3-D inversion: it reveals the horizontal limit of structures.

Conductive structure C4

A shallow conductive structure (C4) is present at depths of 0.5-2 km beneath the inactive Martimbang volcano and correlates with a magnetic low anomaly found by Situmorang (2005). In geothermal systems, negative magnetic anomalies have been generally associated with alteration zones because a change in the mineral composition can decrease magnetic susceptibility. Additionally, the surroundings of the Martimbang volcano are associated with a Bouguer low, possibly caused by sedimentary rocks (Djudjun, 2005). The conductor C4 is interpreted as hydro-thermally altered andesitic material, due to high temperatures caused by the magma intrusion of Martimbang in the past.

If I use the same resistivity limit as for the conductor C2 (37 Ωm), then the conductor C4 also extends to a 10 km depth. However, as mentioned before in Subsection 4.2.3, the resolution beneath the Martimbang volcano is poor for both 2-D and 3-D inversions. Additionally, the geochemical data in the study area shows that the hot spring temperatures increase with distance from the Martimbang (Nukman and Moeck, 2013). The isotope ratios of Oxygen 18 and the deuterium (δ) of the hot springs close to the Martimbang are lower than those of the PNB hot spring (Ardiwinata et al., 2005; Nukman, 2014). Therefore, the hot springs close to the Martimbang show no magmatic signature.

4.3.2 Conceptual model of the Sipoholon geothermal system

One of the major outcomes of the MT study is the conceptual model of the Sipoholon geothermal system, which is based on the conductivity distributions combined with the results of other studies. The geothermal elements of the Sipoholon geothermal system are summarized in Figure 4.21, which shows a cross section of the 3-D inversion model.

First, meteoric waters, labelled as number 1 in Figure 4.21, flow into the underground. Simultaneously, magmatic waters ascend from the subsurface through the deeper part of a permeable fault system, creating hot deep circulating waters, labelled as number 2. Inferred from the geochemical studies, fluids of the PNB hot spring contain magmatic waters. It seems that the magmatic fluids prefer flowing through the PNB normal fault than through normal faults beneath the Tarutung basin as indicated by some seismic events trending upward coinciding with depth extent of the Panabungan (PNB) normal fault between depths of 4 km and 8 km.

The cold meteoric and hot magmatic waters mix in the reservoir, labelled as number 3. Finally, these mixed waters flow up to surface through the upper part of the permeable fault, resulting in geothermal manifestations (e.g. the PNB hot spring). It is also possible that some of the

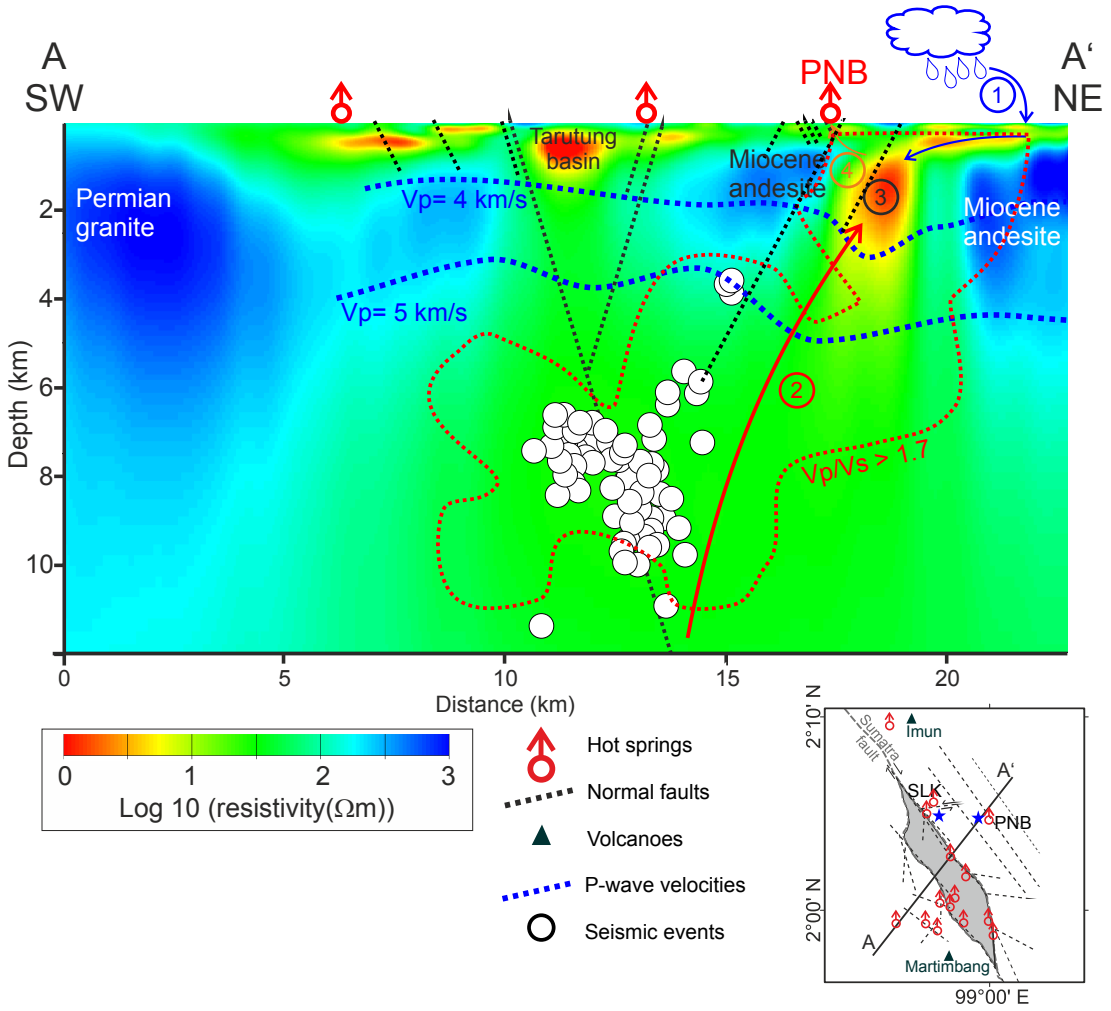

Figure 4.21: Cross section from the preferred 3-D MT inversion result and its interpretation. Black dashed lines indicate normal faults and are extended from surface to depths (modified from Nukman and Moeck (2013)). Blue dashed lines mark P-wave velocity and red dashed line indicates a high Vp/Vs ratio (modified from Muksin et al. (2013), including location of seismic events). Firts, cold meteoric water flow into the reservoir (as indicated by ①). Simultaneously, deep circulating hot water containing magmatic fluids ascends through the permeable faults (②). Cold and hot waters mix in the reservoir ③, when the mixed water are hot enough, then the mixed water rise up ④ to surface through permeable faults and appear as geothermal manifestations (i.e. hot springs).

mixed waters flow through the un-conformity of the Miocene andesites and then rise up along permeable faults producing hot springs on the edge of the Tarutung basin.

The borders of the Miocene andesite un-conformity in Figure 4.21 are deduced from the velocity model from Muksin et al. (2013) and from the surface geology from Nukman (2014). Accordingly, the mixed waters do not flow further to the west because the impermeable Permian granites prevents the water flowing further to the west. Similarly, the water also does not flow further to the north of the SLK sealed fault (Figure 4.20).

In summary, an area for future drilling is located between the Tarutung basin and the PNB fault. This area is characterized by low electrical conductivity, low velocity, high Vp/Vs ratio and high attenuation. Furthermore, fluid content of the PNB hot spring exhibit magmatic water signatures. It is probably safe to suggest two location for shallow (< 500 m depth) boreholes (as indicated by blue starts) prior to deeper exploration wells.

Chapter 5

Summary

Magnetotelluric (MT) data have been used to derive the subsurface conductivity structure of the Sipoholon geothermal system, which is classified as a structurally controlled geothermal system. A new conceptual model is compiled from the conductivity structure correlated with results from other disciplines.

Magnetotelluric measurements

This study presents magnetotelluric measurements in the Sipoholon area, located in the vicinity of the Tarutung basin (TB), a densely populated region. The TB is part of a negative flower structure along the 1650 km long Sumatra fault. High voltage power lines are parallel to the fault from the northern part to the southern part of the Sumatra island and generate noise in the MT data. For improving MT data quality, showing obvious man-made noise, advanced MT data processing procedures, i.e. successive delay line filtering and robust remote reference (RR) processing, were applied. However, strong coherent noise are present, which cannot be suppressed efficiently by the processing. This yields strongly scattered data in the band between 2 s and 20 s. These outliers were then manually removed before the data analysis and the inversion.

Analysis of the impedances and VTFs show a 2-D character of the data and result in a geo-electric strike of N36 °W, which is close to the Sumatra fault direction in the study area. This direction, i.e. N36 °W, is almost perpendicular to the real induction arrow directions at long periods and coincides with average direction of the principal axes of the phase tensor ellipses.

2-D inversion results

Two-dimensional (2-D) inversion was performed, including a number of tests with different data weighting and smoothing parameters. The influence of down-weighting the data components, e.g. using 0.05 error floor of VTFs, generates lower RMS, which means better data fit. Down-weighting ρ TE by using 100 % error floor is needed to accommodate static shift. Additionally, due to the fact that the ρ TE data are noisier, giving more weight to ρ TE resulted in higher RMS misfits and introduced inversion artifacts.

The smoothing parameters, i.e. global (τ) and horizontal (α), influence the model result. 2-D inversion using high values of smoothing parameters resulted in high RMS and shows almost no structure beneath 2 km depths. In contrast, using small values of smoothing parameters yield low RMS but high model roughness. By using optimal values of the smoothing parameters, a good compromise between good data fit and a minimum structure model is sought and obtained.

The preferred model for the 2-D inversion reveal two resistors and four conductors. One of the conductors is a deep reaching conductive anomaly, which correlates at surface with the location of the Panabungan (PNB) hot spring. A constrained inversion recovers this conductor. This implies that the deep reaching conductor is required by the data and it is not an artifact.

As mentioned before, the data outliers in the dead band (i.e. 2-20 s) were manually removed, which yields data gaps between short and long periods. An inversion test using hampered synthetic data in the dead band demonstrates that this is not a problem as long as the data at long periods are trustworthy.

3-D inversion results

Some data show a three-dimensional (3-D) character, thus a 3-D inversion was also performed, including data and grid rotation tests. The 3-D inversion using un-rotated impedances and VTFs displays similar high conductivity contrasts as the 3-D inversion using only impedances rotated to the geo-electric strike. However, RMS misfit of the first model results (using un-rotated impedances and VTFs) is lower, i.e. 1.8, than the second model, i.e. 2.9. The inversion of the rotated data resulted in an additional small conductor beneath the Permian granite location. The preferred model for the 3-D inversion is based on un-rotated impedances and VTFs.

Comparison of the 2-D and 3-D inversion results

The 3-D inversion reveals similar structures as the 2-D inversion. However, depths of the structures are generally shallower in 3-D than for 2-D inversion. Nevertheless, the 2-D and 3-D inversion results complement each other, as 3-D inversion better controls structures in off-profile area. The interpretation of structures from the 2-D and 3-D inversion are summarized below:

Conductor C1

A shallow conductor (C1) is revealed beneath the TB and is interpreted as unconsolidated sedimentary rocks with high porosity, which could be filled by fluids. The lowest resistivity value of the conductor C1 ($\leq 1\ \Omega$m) is located close to the Ria-Ria hot spring and the Ria-Ria normal fault. This suggests that there are fluid paths through permeable faults where the (hot saline) fluids can flow upwards to surface and form hot springs. The base of the conductor C1 coincides with the base of the TB and correspond to a high Vp layer.

Conductor C2

The deep reaching conductor correlates at surface with the location of the PNB hot spring and the PNB normal fault, which is part of a negative flower structure related to the Sumatra fault. The deep reaching conductor represents a permeable zone, filled with hot saline fluids, particularly at a depth of 2 km. This anomaly corresponds to a possible reservoir. The deep water circulation could be caused by the magmatic fluids. There are no indications for a magma chamber nor for magma upward movement (i.e. a plume-like conductive structure such as found in the Taupo Volcanic Zone, New Zealand (Heise et al., 2007, 2010)). Furthermore, typical surface manifestations corresponding to magma chamber occurrences in Indonesia (e.g. fumaroles, acidic surface alteration) are absent (Hochstein and Sudarman, 1993; Nukman and Moeck, 2013).

Conductor C4

Another shallow conductor is imaged beneath hot springs close to the inactive Martimbang volcano. This shallow conductor is interpreted as hydro-thermally altered andesitic material due to high temperatures caused by magma intrusion of the Martimbang in the past. There is no indication for a magma chamber occurrence beneath the inactive Martimbang volcano. Furthermore, temperatures of hot springs increase with distance from the Martimbang.

Resistors R1 and R2

The MT inversion results reveal two resistors. One resistor appears consistently in the southwestern part of all profiles and coincides spatially with the boundary between the Permian granites and the Miocene andesites. The other resistor occurs in the eastern part of the study area

and corresponds with Miocene andesitic rocks at surface. The MT inversion results display high resistivity responses for both granite and andesite rocks, but the resistivity of the structure R2 is in general lower than R1. The reason could be that the granites are less weathered/eroded than the andesites. However, both resistors R1 and R2 suggest that these high resistivities are due to compact rocks with low porosity.

Conceptual model of the Sipoholon geothermal system

A conceptual model of the Sipoholon geothermal system, based on the conductivity distribution, is composed from the interpretation of the 2-D and 3-D inversion results. Cold meteoric water enters a possible reservoir rock through permeable faults (e.g. the PNB fault). The cold water in the reservoir is then heated up by deep circulating hot magmatic fluids. The mixed waters, i.e. meteoric and magmatic waters, flow upwards through permeable faults due to thermal buoyancy.

The Sipoholon geothermal system is bordered by impermeable rocks, i.e. Permian granites, in the western part, and by a sealed fault in the northern part of the study area. Both sealed fault and the impermeable Permian granites prevent the fluid flow further to the north and west, respectively.

Outlook

This conceptual model is in a good agreement with models from geochemical and geological studies. However, a shallow ($\leq$ 500 m) borehole around the PNB would be advantageous to get more information about the subsurface. Further studies could be performed prior to an exploration drilling (i.e. $>$ 2 km depth). These studies include correlation between measured parameters like porosity, salinity, temperature, and resistivity of rocks, including a comparison with the inversion model results.

A structure that is most likely a target of future drilling is an electrically conductor at a depth of 2 km close to the PNB (i.e. the conductor C2), where low velocity and high Vp/Vs ratio occurs. A possible target for exploration as well as shallow borehole is located between the Ria-ria and the Panabungan hot springs, as indicated by red star in Figure 4.21. A possible target for injection well is located to the northeast of the Panabungan hot spring, as indicated by blue star in Figure 4.21.

Bibliography

Aldiss, D. T., Whandoyo, R., Sjaefudien, A. G., and Kusjino (1983). The geology of Sidikalang quadrangle, Sumatra, Indonesia. Technical report, Geological Research Centre, Bandung, Indonesia.

Anderson, E., Crosby, D., and Ussher, G. (2000). Bulls-eye! Simple resistivity imaging to reliably locate the geothermal reservoir. In *Proceedings World Geothermal Congress, Kyushu-Tohoku, Japan*. IGA.

Archie, G. E. (1942). The electrical resistivity log as an aid in determining some reservoir characteristics. *Tran. AIME*, 146:54–67.

Ardiwinata, N., Setiawan, Asngari, Supardjo, E., and Kurniawan, S. (2005). Penyelidikan geokimia panasbumi daerah Sipoholon, Kabupaten Tapanuli Utara, Sumatera Utara. Technical report, Center for Geological Resources, Bandung, Indonesia.

Avdeev, D. and Avdeeva, A. (2009). 3D magnetotelluric inversion using a limited-memory quasi-Newton optimization. *Geophysics*, 71:G191–G196. doi:10.1190/1.3114023.

Bahr, K. (1988). Interpretation of the magnetotelluric impedance tensor: regional induction and local telluric distortion. *Journal of geophysics*, 62:119–127.

Barber, A. J. and Crow, M. J. (2003). An evaluation of plate tectonic models for the development of Sumatra. *Gondwana Research*, 2:1–28.

Becken, M. and Burkhardt, H. (2004). An ellipticity criterion in magnetotelluric tensor analysis. *Geophys. J. Int.*, 159:69–82. doi:10.1111/j.1365-246X.2007.03612.x.

Becken, M., Ritter, O., and Burkhardt, H. (2008). Mode separation of magnetotelluric responses in three-dimensional environments. *Geophys. J. Int.*, 172:67–86.

Bellier, O. and Sebrier, M. (1995). Is the slip rate variation on the Great Sumatran Fault accommodated by fore-arc stretching? *Geophysical Research Letters*, 22:1969–1972.

Berdichevsky, M. N. and Dmitriev, V. I. (2008). *Models and methods of magnetotellurics*. Springer, Verlag, Berlin, Heidelberg.

Berdichevsky, M. N., Dmitriev, V. I., and Pozdnjakova, E. E. (1998). On two-dimensional interpretation of magnetotelluric soundings. *Geophys. J. Int.*, 133:585–606.

Berktold, A. (1983). Electromagnetic studies in geothermal regions. *Geophysical Surveys*, 6:173–200.

Booker, J. R. (2013). The magnetotelluric phase tensor: A critical review. *Surv Geophys*, 35:7–40. doi:10.1007/s10712-013-9234-2.

Cagniard, L. (1953). Basic theory of the magnetotelluric method of geophysical prospecting. *Geophysics*, 18:605–635.

Caldwell, G., Pearson, C., and Zahadi, H. (1986). Resistivity of rocks in geothermal systems: A laboratory study. In *Proceedings of the Eighth New Zealand Geothermal Workshop, Auckland, New Zealand*. University of Auckland.

Caldwell, T. G., Bibby, H. M., and Caldwell, C. (2004). The magnetotelluric phase tensor. *Geophys J Int*, 158:457–469. doi:10.1111/j.1365-246X.2004.02281.x.

Caricchi, L., Burlini, L., and Ulmer, P. (2008). Propagation of P and S-waves in magmas with different crystal contents: Insights into the crystallinity of magmatic reservoirs. *Journal of Volcanology and Geothermal Research*, 178:740–750.

Cathelineau, M., Oliver, R., Izquierdo, G., Garfias, A., Nieva, D., and Izaguirre, O. (1983). Mineralogy and distribution of hydrothermal mineral zones in Los Azufres (Mexico) geothermal field. In *Proceedings of the Ninth Workshop on Geothermal Reservoir Engineering, California, U.S.A.* Stanford University.

Chen, X. (2008). Filterung von geophysikalischen Zeitreihen mit periodisch auftretenden multifrequenten Störsignalen. Diploma Thesis, Technischen Universität Berlin.

Cumming, W. (2009). Geothermal resource conceptual models using surface exploration data. In *Proceedings of the Thirty-Fourth Workshop on Geothermal Reservoir Engineering, California, U.S.A.* Stanford University.

Curewitz, D. and Karson, J. A. (1997). Structural settings of hydrothermal outflow: Fracture permeability maintained by fault propagation and interaction. *Journal of Volcanology and Geothermal Research*, 79:149–168.

Darma, S., Harsoprayitno, S., Setiawan, B., Hadyanto, Sukhyar, R., Soedibjo, A. W., Ganefianto, N., and Stimac, J. (2010). Geothermal energy update: Geothermal energy development and utilization in Indonesia. In *Proceedings World Geothermal Congress, Bali, Indonesia*. IGA.

Djudjun, A. (2005). Penyelidikan gaya berat daerah panasbumi Sipoholon, Kabupaten Tapanuli Utara, Sumatera Utara. Technical report, Center for Geological Resources, Bandung, Indonesia.

Egbert, G. D. and Kelbert, A. (2012). Computational recipes for electromagnetic inverse problems. *Geophys. J. Int.*, 189:251–267. doi:10.1111/j.1365-246X.2011.05347.x.

Ellis, A. J. and Mahon, W. A. J. (1982). *Chemistry and geothermal systems*. Academic Press, Inc., London, UK.

Flovenz, O. G., Spangenberg, E., Kulenkampff, J., Arnason, K., Karlsdottir, R., and Huenges, E. (2005). The role of electrical interface conduction in geothermal exploration. In *Proceedings World Geothermal Congress, Antalya, Turkey*. IGA.

Fridleifsson, I. B., Bertani, R., Huenges, E., Lund, J. W., Ragnarsson, A., and Rybach, L. (2008). The possible role and contribution of geothermal energy to the mitigation of climate change. In *Proceedings of the IPCC Scoping meeting on the renewable energy sources, Lübeck, Germany*. the University of Flensburg.

Gabas, A. and Marcuello, A. (2003). The relative influence of different types of magnetotelluric data on joint inversions. *Earth Planets Space*, 55:243–248.

Geiermann, J. and Schill, E. (2010). 2-D Magnetotellurics at the geothermal site at Soultz-sous-Forêts: Resistivity distribution to about 3000 m depth. *Comptes Rendus Geoscience*, 342:587–599. doi:10.1016/j.crte.2010.04.001.

Genrich, J. F., Bock, Y., McCaffrey, R., Prawirodirdjo, L., Stevens, C. W., Puntodewo, S. S. O., Subarya, C., and Wdowinski, S. (2000). Distribution of slip at the northern Sumatra fault system. *Journal of Geophysical Research*, 105:28.327–28.341.

Giroud, N., Vuataz, F. D., and Schill, E. (2012). Geothermal reservoir of the EGS pilot plant at Soultz-sous-Forêts (France): Monitoring of the exploitation and prediction of its behaviour. Technical report, Swiss Federal Office of Energy, Ittigen, Switzerland.

Hansen, P. C. (2000). The l-curve and its use in the numerical treatment of inverse problems. In *In Computational Inverse Problems in Electrocardiology, ed. P. Johnston, Advances in Computational Bioengineering*, pages 119–142. WIT Press.

Hasan, R., Setiadarma., Risdianto, D., and Supardi, K. (2005). Geologi daerah panasbumi Sipoholon, Kabupaten Tapanuli Utara, Sumatera Utara. Technical report, Center for Geological Resources, Bandung, Indonesia.

Heise, W., Bibby, H. M., Caldwell, T. G., Bannister, S. C., Ogawa, Y., Takakura, S., and Uchida, T. (2007). Melt distribution beneath a young continental rift: The Taupo Volcanic Zone, New Zealand. *Geophys. Res. Lett.*, 34:L14313,1–6. doi:10.1029/2007GL029629.

Heise, W., Caldwell, T. G., Bibby, H. M., and Bannister, S. C. (2008). Three-dimensional modelling of magnetotelluric data from the Rotokawa geothermal field, Taupo Volcanic Zone, New Zealand. *Geophys. J. Int.*, 173:740–750. doi:10.1111/j.1365-246X.2008.03737.x.

Heise, W., Caldwell, T. G., Bibby, H. M., and Bennie, S. L. (2010). Three-dimensional electrical resistivity image of magma beneath an active continental rift, Taupo Volcanic Zone, New Zealand. *Geophys. Res. Lett.*, 37:L10301,1–5. doi:10.1029/2010GL043110.

Hersir, G. P. and Arnason, K. (2012). Resistivity of rocks. In *Proceedings of the Short Course VII on Exploration for Geothermal Resources, Lake Naivasha, Kenya*. United Nations University.

Hersir, G. P. and Bjornsson, A. (1991). *Geophysical Exploration for geothermal resources: principles and application*. UNU Geothermal Training Programme, Reykjavik, Iceland.

Hochstein, M. P. (1988). Assessment and modelling of geothermal reservoirs (small utilization schemes). *Geothermics*, 17:15–49.

Hochstein, M. P. and Sudarman, S. (1993). Geothermal resources of Sumatra. *Geothermics*, 22:181–200.

Hochstein, M. P. and Sudarman, S. (2008). History of geothermal exploration in Indonesia from 1970 to 2000. *Geothermics*, 37(3):220–266.

Hoffmann-Rothe, A. (2002). Combine structural and magnetotelluric investigation across the West Fault Zone in the Northern Chile. Technical report, GFZ, Potsdam, Germany.

Karato, S. I. and Wang, D. (2013). *Electrical Conductivity of Minerals and Rocks, in Physics and Chemistry of the Deep Earth*. John Wiley and Sons, Ltd, Chichester, UK.

Katili, J. A. (1975). Volcanism and plate tectonics in the Indonesian island arcs. *Tectonophysics*, 26:165–188.

Kelbert, A., Meqbel, M., Egbert, G. D., and Tandon, K. (2014). Modem: A modular system for inversion of electromagnetic geophysical data. *Computers & Geosciences*, 66:40–537. doi:10.1016/j.cageo.2014.01.010.

Koulakov, I., Yudistira, T., Luehr, B. G., and Wandono. (2009). P, S velocity and Vp/Vs ratio beneath the Toba caldera complex (Northern Sumatra) from local earthquake tomography. *Geophys. J. Int.*, 62:1–19. doi:10.1111/j.1365-246X.2009.04114.x.

Krings, T. (2007). The influence of robust statistics, remote reference, and horizontal magnetic transfer functions on data processing in magnetotellurics. Master's thesis, Universität Münster.

Llera, F. J., Sato, M., Nakatsuka, K., and Yokoyama, H. (1990). Temperature dependence of the electrical resistivity of water saturated rocks. *Geophysics*, 56:576–585.

Lubimova, E. A., Zorin, U. A., and Lysak, S. V. (1972). Geothermal anomaly in the Baikal lake region. *Geothermics*, 1:31–34.

Lund, J. W. and Bloomquist, R. G. (2012). Development of geothermal policy in the United States - What works and what doesn't work. In *Proceedings of the Thirty-Seventh Workshop on Geothermal Reservoir Engineering, California, U.S.A.* Stanford University.

Manzella, A., Ungarelli, C., Ruggieri, G., Giolito, C., and Fiordelisi, A. (2010). Electrical resistivity at the Travale geothermal field (Italy). In *Proceedings World Geothermal Congress, Bali, Indonesia*. IGA.

Meqbel, N. M., Egbert, G. D., Wannamaker, P. E., and Kelbert, A. (2014). Deep electrical resistivity structure of the north western U.S. derived from 3D inversion of USArray magnetotelluric data. *Earth and Planetary Science Letters*. doi:10.1016/j.epsl.2013.12.026.

Meqbel, N. M. M. (2009). *The electrical conductivity structure of the Dead Sea Basin derived from 2D and 3D inversion of magnetotelluric data*. Phd thesis, Fachber. Geowiss., Freie Universität Berlin, Germany.

Metcalfe, I. (1983). Conodont faunas, age and correlation of the Alas Formation (Carboniferous), Sumatra. *Geological Magazine*, 120:579–586.

Muñoz, G. (2013). Exploring for geothermal resources with electromagnetic methods. *Surv. Geophys.*, 35:101–122.

Muñoz, G., Ritter, O., and Moeck, I. (2010). A target-oriented magnetotelluric inversion approach for characterizing the low enthalpy Groß Schönebeck geothermal reservoir. *Geophys. J. Int.*, 183:1199–1215.

Muksin, U., Haberland, C., Bauer, K., and Weber, M. (2013). Three-dimensional upper crustal

structure of the geothermal system in Tarutung (North Sumatra, Indonesia) revealed by seismic attenuation tomography. *Geophys. J. Int.*, 195:2037–2049. doi:10.1093/gji/ggt383.

Munandar, A. and Widodo, S. (2013). Geothermal resources development in Indonesia. In *Proceedings of the 10th Asian Geothermal Symposium, Tagaytay, Philippines*. AIST.

Nukman, M. (2014). *Geothermal exploration involving structural geology and hydro-chemistry in the Tarutung Basin, Northern Central Sumatra (Indonesia)*. Phd thesis, Fakultät VI, Technischen Universität Berlin, Germany.

Nukman, M. and Moeck, I. (2013). Structural controls on a geothermal system in the Tarutung Basin, North Central Sumatra. *Journal of Asian Earth Sciences*, 74:86–96.

Quist, A. S. and Marshall, W. L. (1968). Electrical conductances of aqueous sodium chloride solutions from 0 to 800° and at pressures to 4000 bars. *J. Phys. Chem.*, 72:684–703.

Ritter, O., Junge, A., and Dawes, G. (1998). New equipment and processing for magnetotelluric remote reference observations. *Geophysical Journal International*, 132:535–548.

Rodi, W. and Mackie, R. L. (2001). Nonlinear conjugate gradients algorithm for 2-D magnetotelluric inversion. *Geophysics*, 66:174–187.

Schiavone, D. and Loddo, M. (2007). 3-D density model of Mt. Etna Volcano (Southern Italy). *Journal of Volcanology and Geothermal Research*, 164:161–175.

Sieh, K. and Natawidjaja, D. (2000). Neotectonics of the Sumatra fault, Indonesia. *Journal of Geophysical Research*, 105:28.295–28.326.

Situmorang, T. (2005). Penyelidikan geomagnet daerah panasbumi Sipoholon, Kabupaten Tapanuli Utara, Sumatera Utara. Technical report, Center for Geological Resources, Bandung, Indonesia.

Soengkono, S. (2011). Deep interpretation of gravity and airborne magnetic data of the central Taupo Volcanic Zone. In *Proceedings of the New Zealand Geothermal Workshop, Auckland, New Zealand*. New Zealand Geothermal Association.

Szarka, L. (1988). Magnetic noise in the earth - A review. *Surveys in Geophysics*, 9:287–318.

Tamanyu, S. and Sakaguchi, K. (2003). Conceptual model for non-volcanic geothermal resources - examples from Tohoku Japan. In *Proceedings European Geothermal Conference, Szeged, Hungary*. Hungarian Geothermal Association.

Tietze, K. and Ritter, O. (2013). Three-dimensional magnetotelluric inversion in practice – the

electrical conductivity structure of the San Andreas Fault in Central California. *Geophys. J. Int.*, 195(1):130–147. doi:10.1093/gji/ggt234.

Tikhonov, A. N. (1950). On determining electrical characteristics of the deep layers of the Earth's crust. *Dok. Akad. Nauk., USSR*, 73(2):295–297.

Ucok, H., Ershaghi, I., and Olhoeft, G. (1980). Electrical resistivity of geothermal brines. *J. Petrol. Technol.*, 32:717–727.

Umeda, K., Ninomiya, A., and Negi, T. (2009). Heat source for an amagmatic hydrothermal system, Noto Peninsula, Central Japan. *Journal of Geophysical Research*, 114:B01202. doi:10.1029/2008JB005812.

Ussher, G., Harvey, C., Johnstone, R., and Anderson, E. (2000). Understanding the resistivities observed in geothermal systems. In *Proceedings World Geothermal Congress, Kyushu-Tohoku, Japan*. IGA.

Vozoff, K. (1990). Magnetotellurics: Principles and practice. *Earth Planet. Sci.*, 99:441–471.

Vrolijk, P. (1990). On the mechanical role of smectite in subduction zones. *Geology*, 18:703–707.

Wannamaker, P., Maris, V., Sainsbury, J., and Iovenitti, J. (2013). Intersecting fault trends and crustal-scale fluid pathways below the Dixie Valley geothermal area, Nevada, inferred from 3D magnetotelluric surveying. In *Proceedings of the Thirty-Eighth Workshop on Geothermal Reservoir Engineering, California, U.S.A*. Stanford University.

Wannamaker, P. E., Hohmann, G. W., and Ward, S. H. (1984). Magnetotelluric responses of three-dimensional bodies in layered Earths. *Geophysics*, 49:1517–1533.

Weckmann, U., Magunia, A., and Ritter, O. (2005). Effective noise separation for magnetotelluric single site data processing using a frequency domain selection scheme. *Geophysical Journal International*, 161:635–652.

Wiese, H. (1962). Geomagnetische Tiefentellurik Teil II: Die Streichrichtung der untergrundstrukturen des elektrischen Widerstandes, erschlossen aus geomagnetischen Variationen. *Geofisica Pura e Applicata*, 52:83–103.

Williams, C. F., Reed, M. J., and Anderson, A. F. (2011). Updating the classification of geothermal resources. In *Proceedings of the Thirty-Sixth Workshop on Geothermal Reservoir Engineering, California, U.S.A*. Stanford University.

Appendix

Appendix A

For 2D inversion, a mesh generator in WinGlink software package was used. The width of the columns beneath stations was set to 80 m with horizontal increase factor of 1.5. The first layer was set up as 50 m height with a vertical increase factor of 1.2. The total section length and depths are created based on the minimum frequency input.

The grid set-up took into account for the topography. The total number of cells of each profiles depending on the minimum frequency and total number of site. Proifle 4, having the smallest site numbers (6) along profile, exhibits smaller number of columns than profile 2, being the highest site numbers (26) along profile. A simplified mesh is displayed in Figure 5.1.

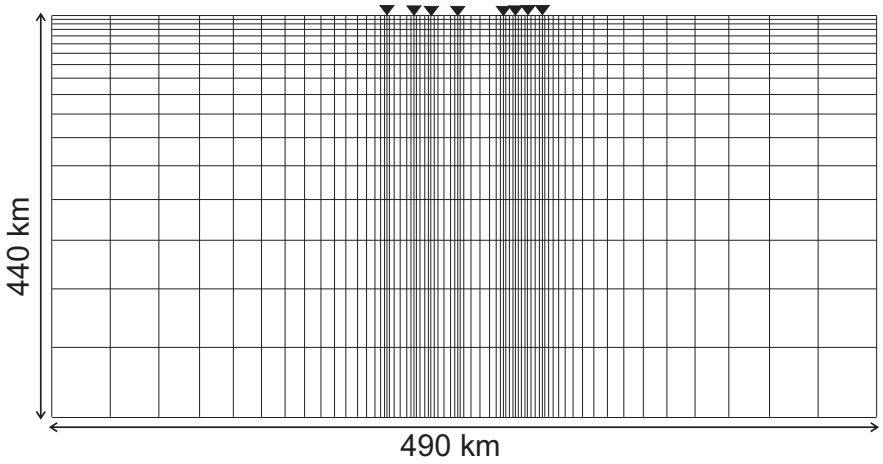

Figure 5.1: A schematic view of the 2-D mesh used for the inversion. Beneath the MT sites, the column width is 80 m. A horizontal increase factor was set to 1.5, creating total length 490 km (i.e. for profile 2). The vertical grid increases by factor 1.2 from 50 m to 74 km height, yielding total depth of 440 km (i.e. for profile 2).

Appendix B

The 3-D Grid software package (Meqbel, 2014, Pers. Comm.) was used to configure a grid. The grid cell dimensions used for the inversion of the Sipoholon data set were 500 m $\times$ 500 m in lateral extent inner grid. Outer grids or the padding cells increase by factor 1.5 for 10 cells each in the east, west, north, and south direction from the edges of the inner grid. The vertical grid increases by a factor 1.2 from 500 m to 367 km. The total inner and outer grid lead to a total model space of 80 $\times$ 80 $\times$ 40 cells, which is equal to 200 km $\times$ 200 km $\times$ 367 km (see Figure 5.2).

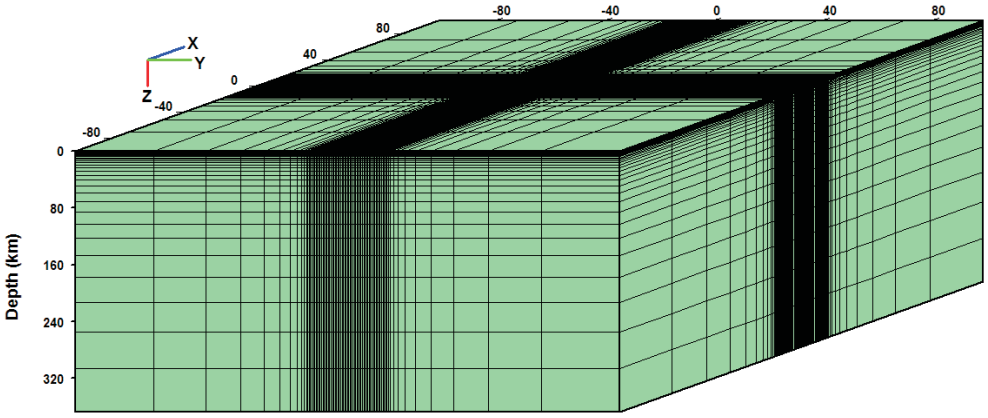

Figure 5.2: A schematic view of the 3D model used for the inversion. X-axes marks N-S directions. Y-axes is in E-W direction. Z-axes is downwards. The centre of the grid, where the MT sites are located, is a regular grid of 500 m $\times$ 500 m in lateral extent. The padding cells are increase by factor 1.5 and are 10 cells to the east, 10 cells to the west, 10 cells to the south, and 10 cells to the north. The vertical grid increases by factor 1.2 from 500 m to 367 km.

Appendix C

The results (Figure 5.3) and the responses (Figure 5.4) display significant differences. This figure indicates that a homogeneous half-space of 1000 Ωm is further from the average resistivity of the data.

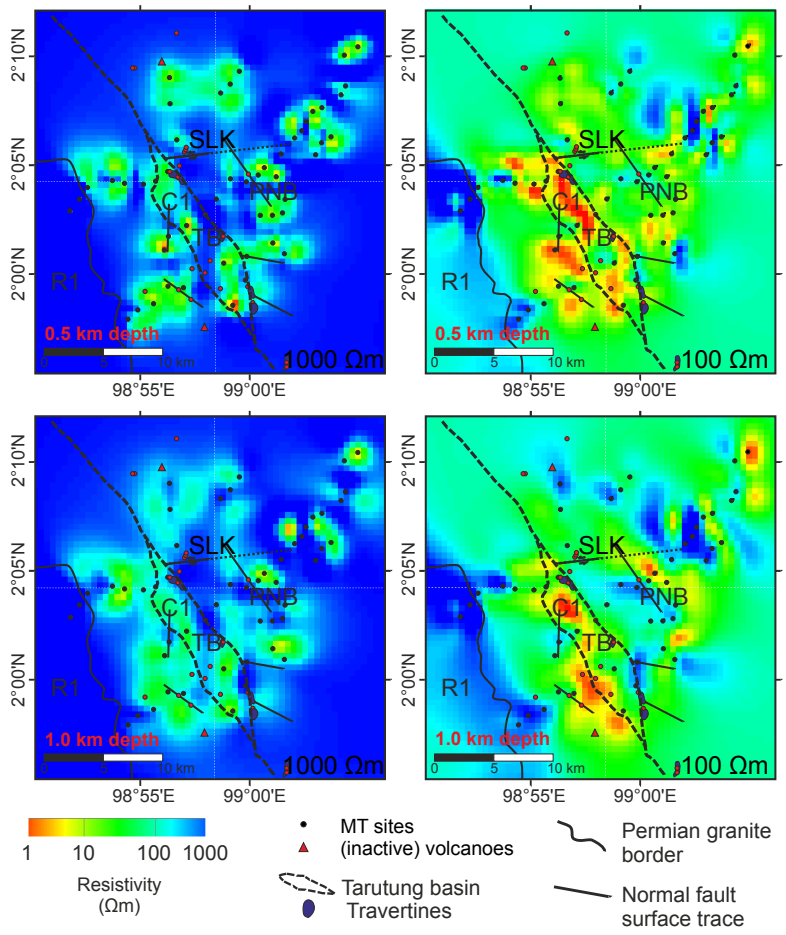

Figure 5.3: Horizontal sections from the 3-D inversion result at depths of 0.5 km and 1.0 km using homogeneous half-spaces 100 Ωm (right column) and 1000 Ωm (left column).

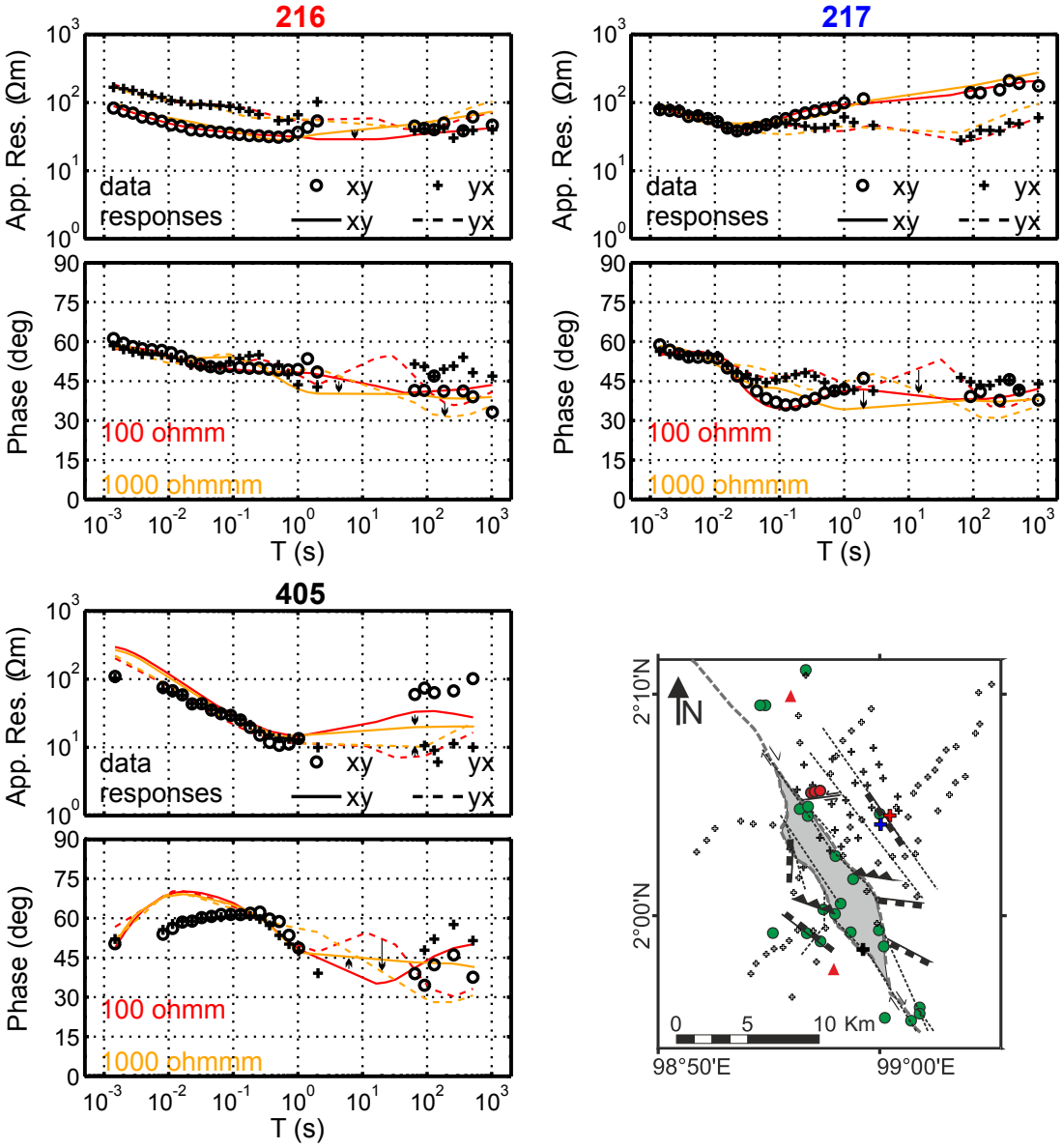

Figure 5.4: Un-rotated observed data (symbols) and model responses (lines) of some sites 216, 217 and 405 (as indicated by red, blue and black crosses, respectively, in lower right panel). Red and orange lines indicate the model responses of the inversion model using homogeneous half-space of 100 Ωm and 1000 Ωm, respectively.

Appendix D

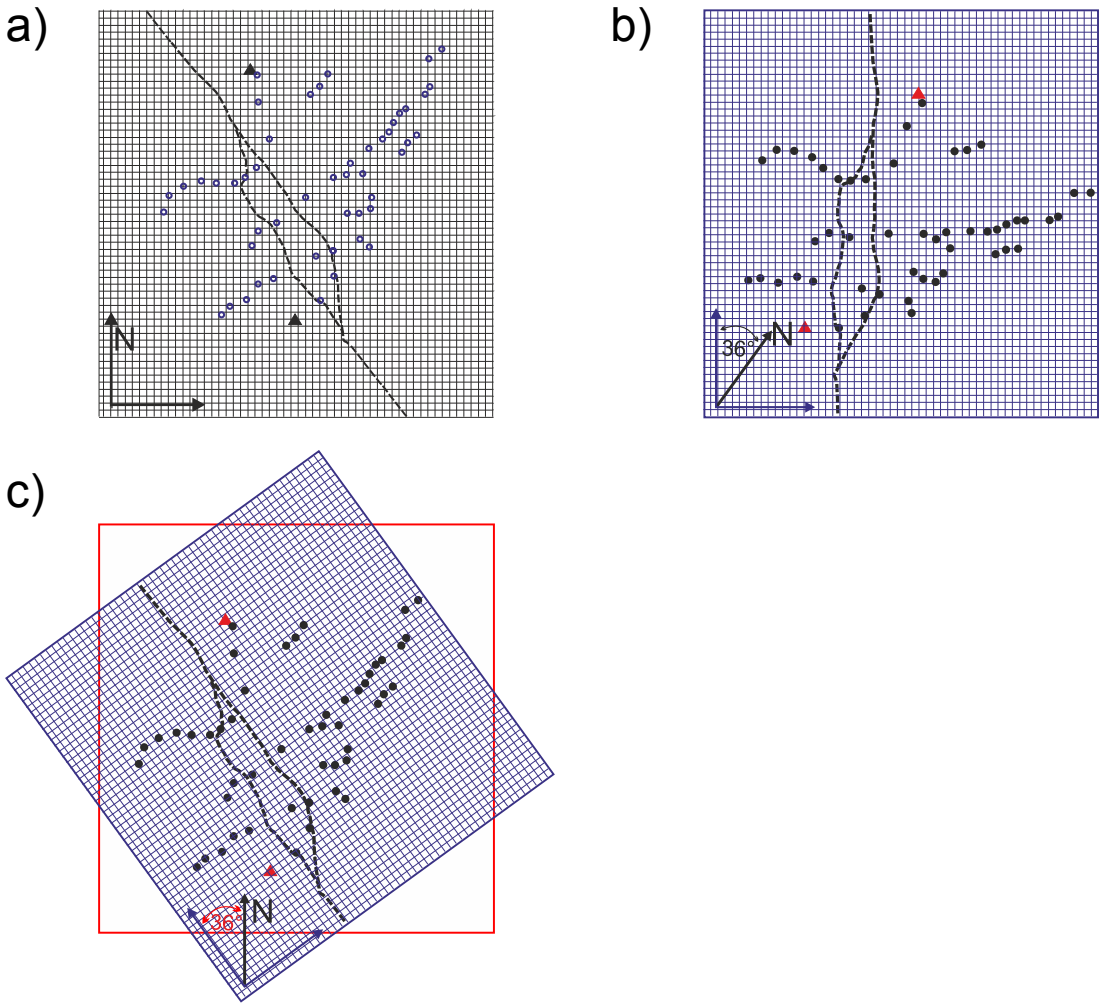

Figure 5.5: Plan view of the core grid schemes used in the inversions. MT sites are marked by black circles. The Tarutung basin is plotted as a black dashed line (after Nukman (2014)). a) The geographical coordinate system (black rectangle) was used for models A, B and C. North is upward. b) Models D, E and F used a coordinate system aligned to the geo-electrical strike direction N36 °W (blue rectangle). c) The red rectangle depicts the horizontal sections of models D, E and F, which were rotated to 36 ° to make visualization of the horizontal sections easier (as indicated by the blue grids). Note that his rotated horizontal sections include some padding cells.

Appendix E

Selected measured data are on the following pages of the Sipoholon and the corresponding responses of 2-D and 3-D model (red lines). These stations are the stations which were used for both 2-D and 3-D inversions. Each page displays four figures from one site. The four figures consist of:

1. Upper left: The apparent resistivity and phase before delay line filtering and remote reference processing was applied.
2. Upper right: The apparent resistivity and phase after delay line filtering and remote reference processing was applied. To clarify, the outliers data were manually removed before the data analysis and the inversion, i.e. mostly between period ranges 2 s and 20 s.
3. Lower left: Rotated observed data (symbols) and model responses of the 2-D preferred model which are displayed as apparent resistivity and phase. Red lines are model responses of Figure 4.6.
4. Lower right: Un-rotated observed data (symbols) and model responses (lines) consist of aparent resistivity and phase responses of the 3-D preferred model. The red lines indicate the model responses of Figure 4.12 or Figure 4.20.

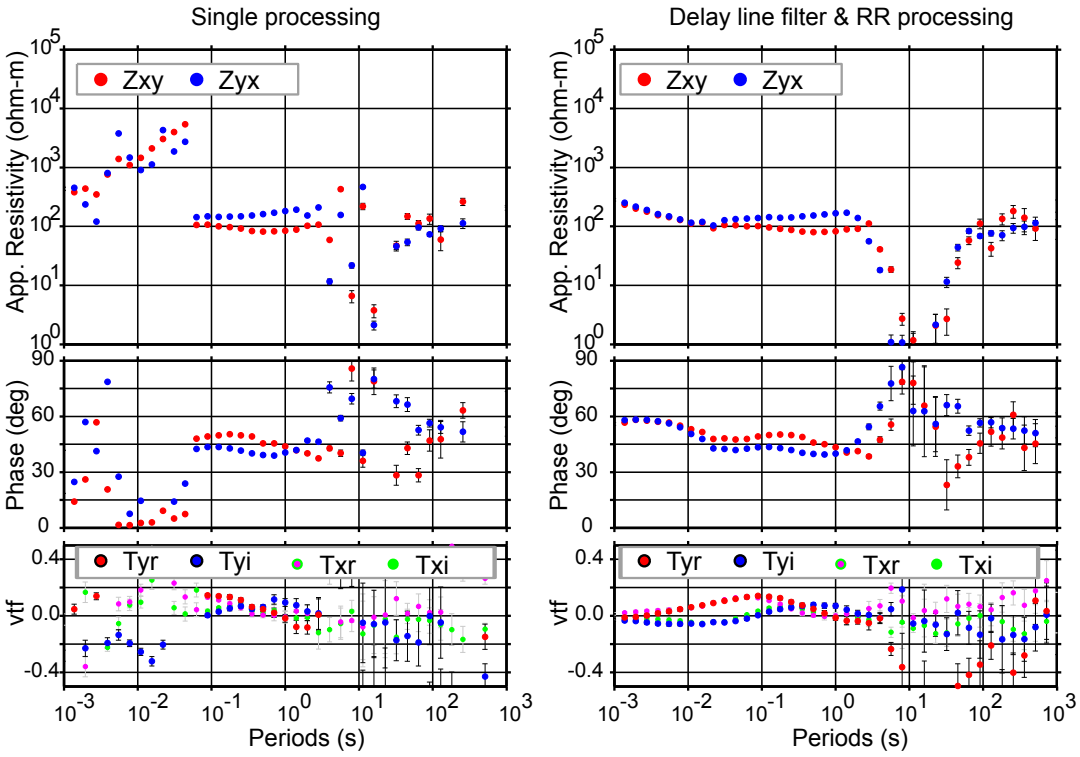
Single processing
Delay line filter & RR processing
App. Resistivity (ohm-m)
Phase (deg)
vtf
Zxy
Zyx
Tyr
Tyi
Txr
Txi
Periods (s)

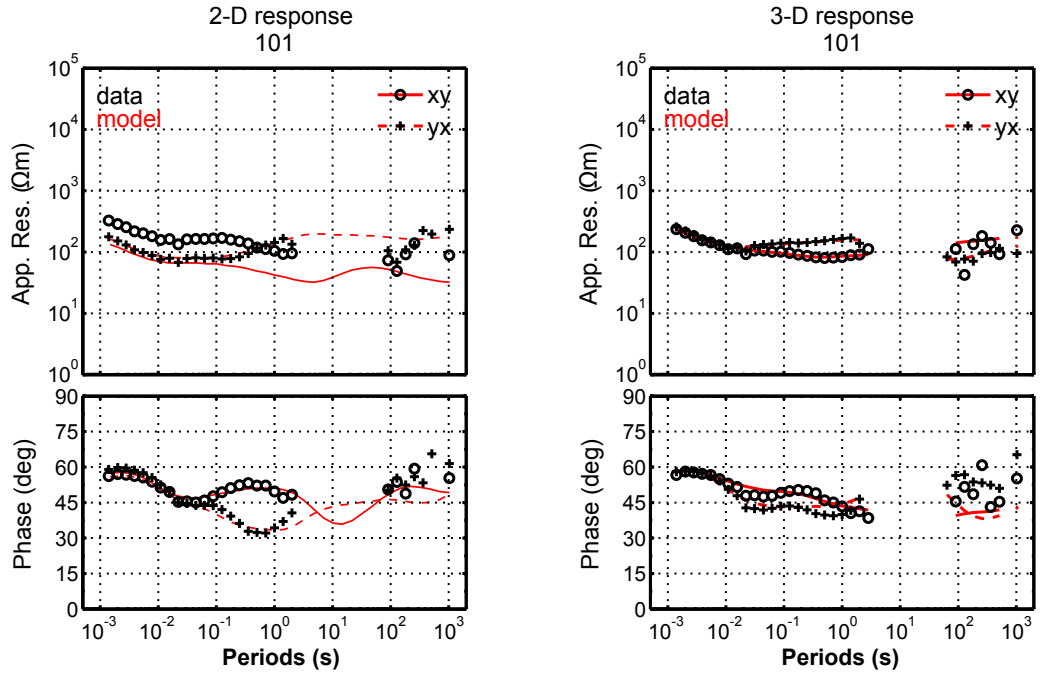
2-D response
101
3-D response
101
data
model
xy
yx
App. Res. (Ωm)
Phase (deg)
Periods (s)

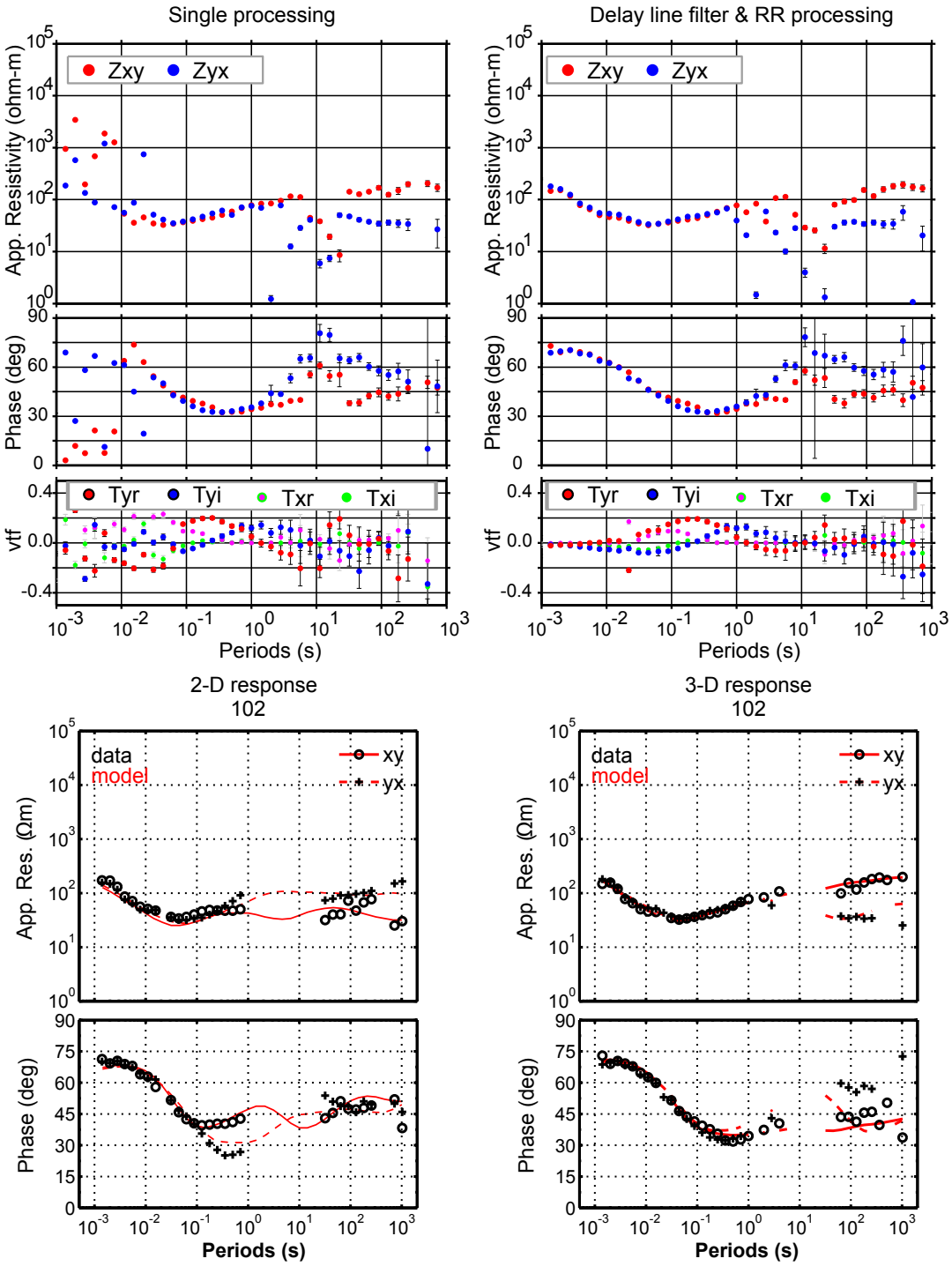
Single processing
Delay line filter & RR processing
App. Resistivity (ohm-m)
Zxy
Zyx
Phase (deg)
vtf
Tyr
Tyi
Txr
Txi
Periods (s)
2-D response
102
3-D response
102
data
model
xy
yx
App. Res. (Ωm)
Phase (deg)
Periods (s)

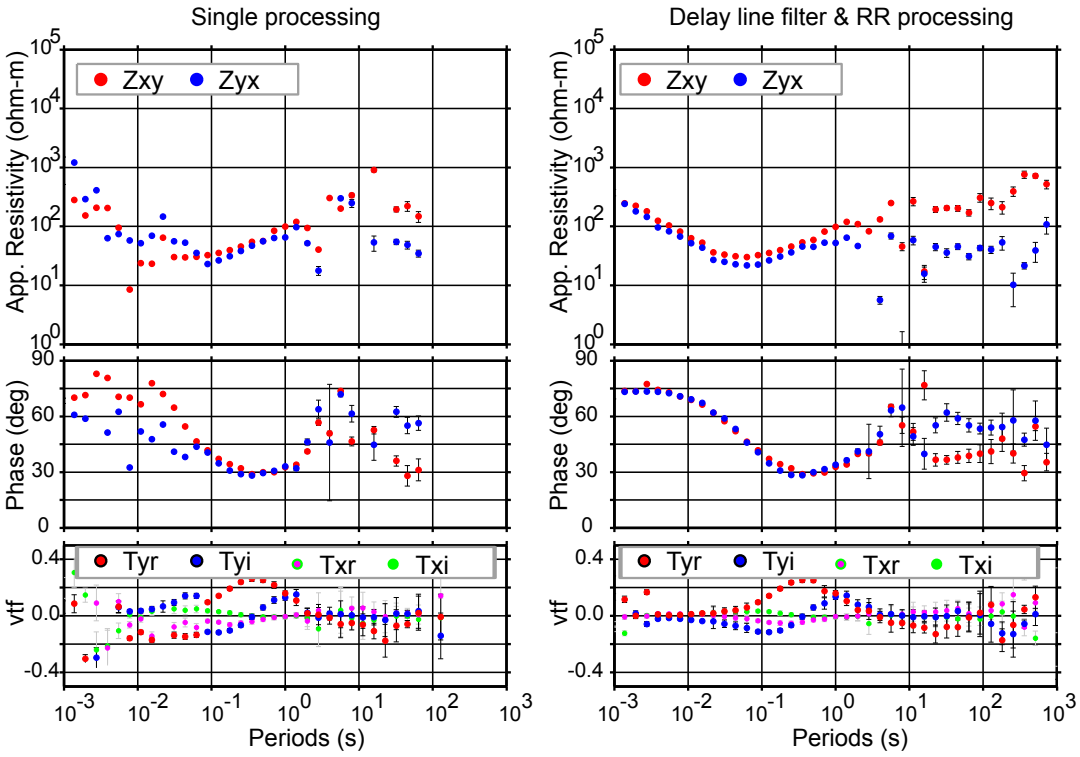
Single processing
Delay line filter & RR processing
App. Resistivity (ohm-m)
Phase (deg)
vtf
Zxy
Zyx
Tyr
Tyi
Txr
Txi
Periods (s)

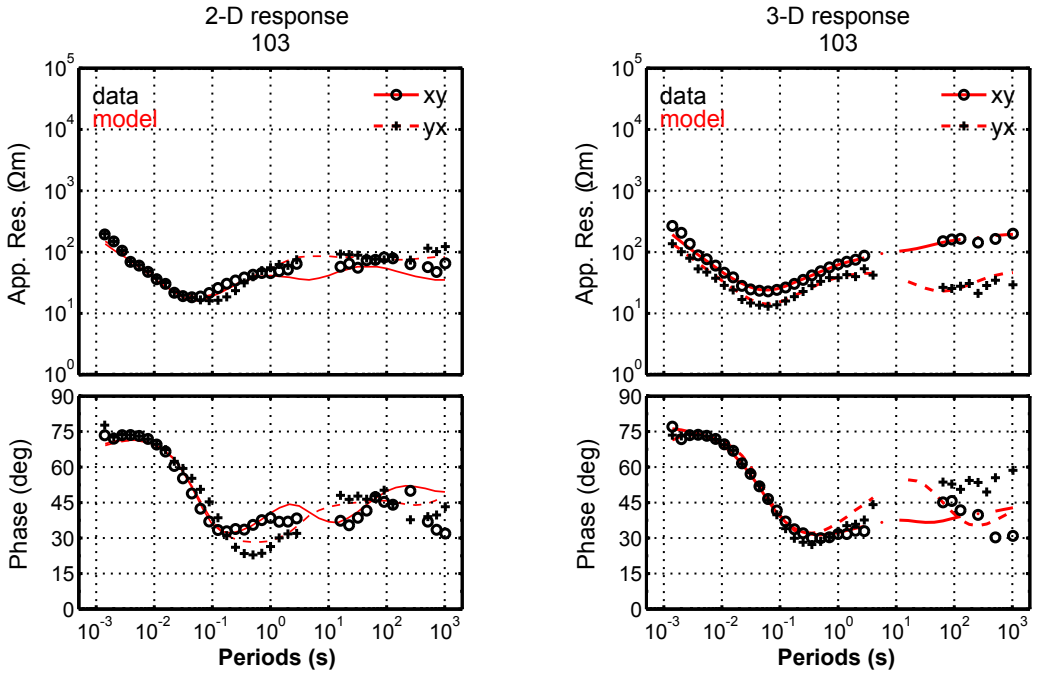
2-D response
103
3-D response
103
data
model
xy
yx
App. Res. (Ωm)
Phase (deg)
Periods (s)

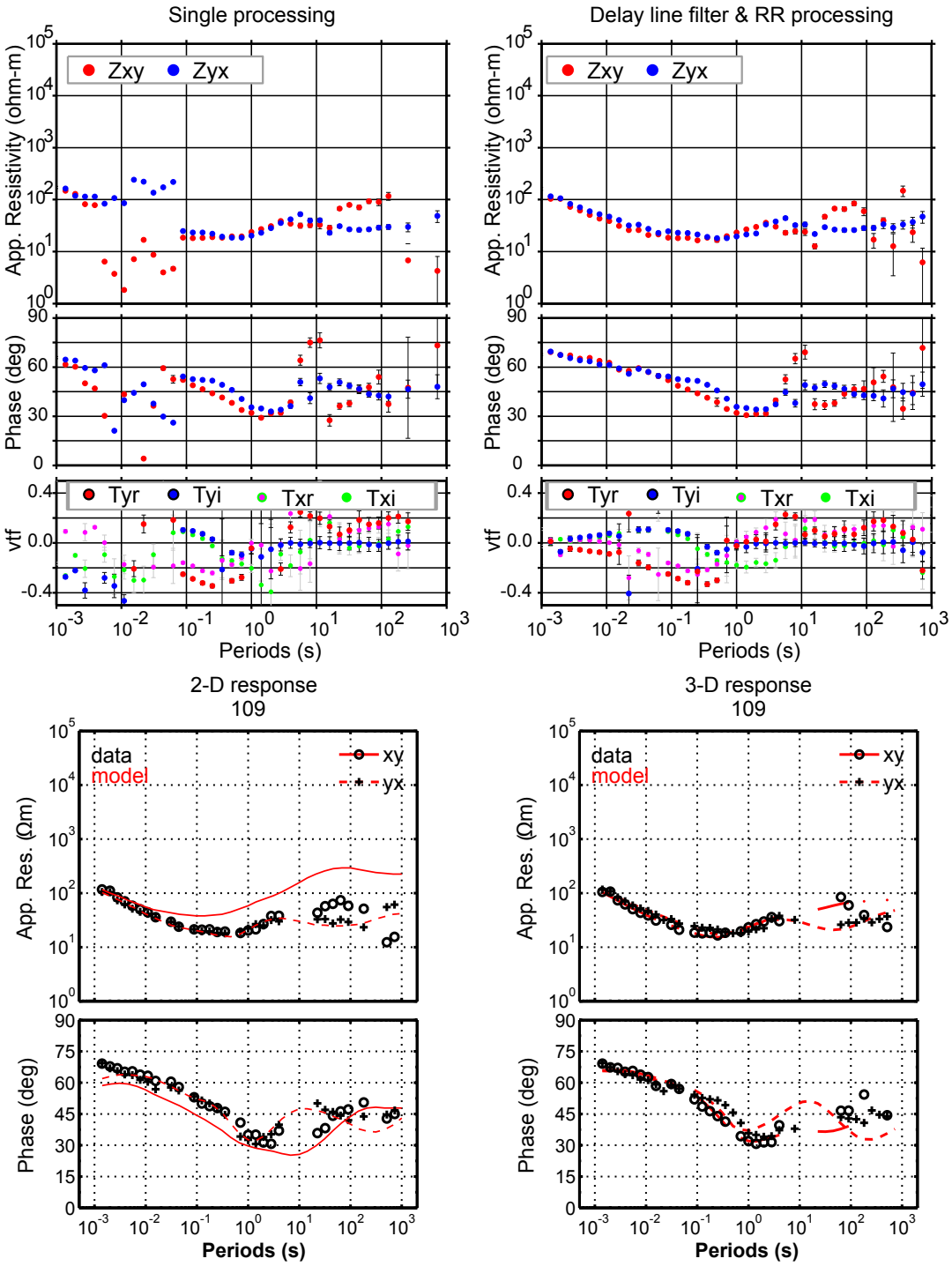
Single processing
Delay line filter & RR processing
App. Resistivity (ohm-m)
Phase (deg)
vtf
Zxy
Zyx
Tyr
Tyi
Txr
Txi
Periods (s)
2-D response
109
3-D response
109
data
model
xy
yx
App. Res. (Ωm)
Phase (deg)
Periods (s)

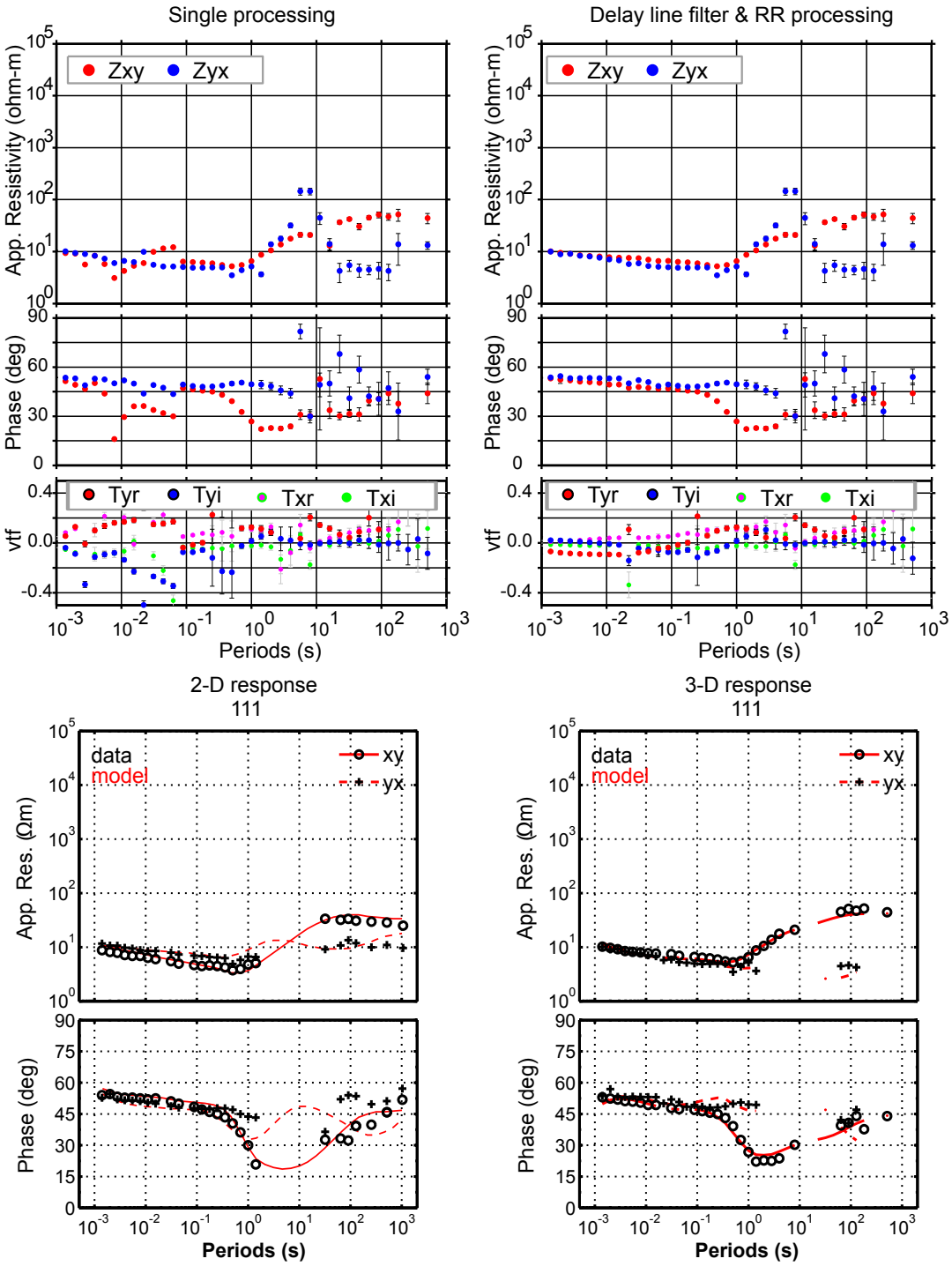
Single processing
Delay line filter & RR processing
App. Resistivity (ohm-m)
Phase (deg)
vtf
Zxy
Zyx
Tyr
Tyi
Txr
Txi
Periods (s)
2-D response
111
3-D response
111
data
model
xy
yx
App. Res. (Ωm)
Phase (deg)
Periods (s)

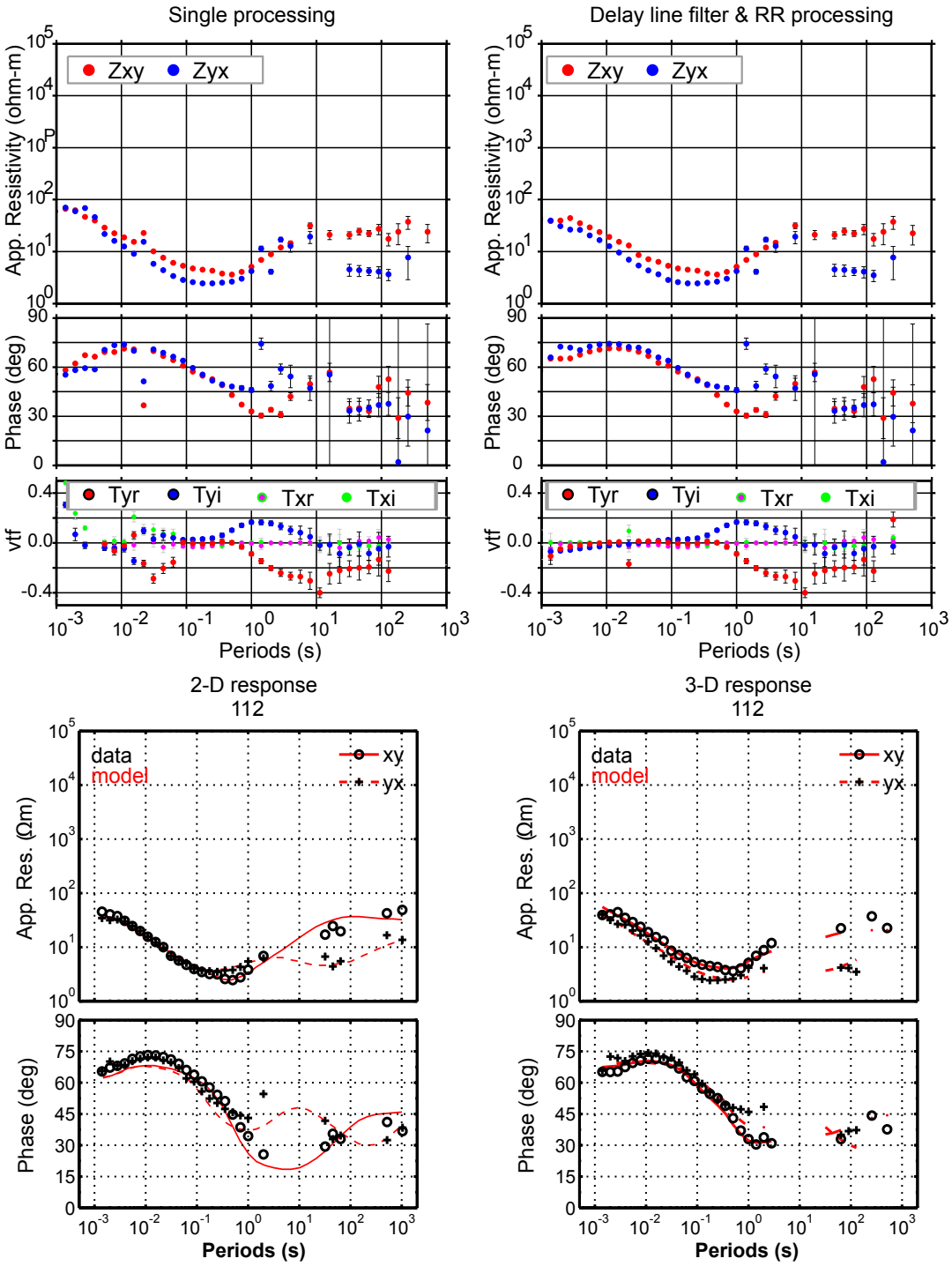
Single processing
Delay line filter & RR processing
App. Resistivity (ohm-m)
Phase (deg)
vtf
Zxy
Zyx
Tyr
Tyi
Txr
Txi
Periods (s)
2-D response
112
3-D response
112
data
model
xy
yx
App. Res. (Ωm)
Phase (deg)
Periods (s)

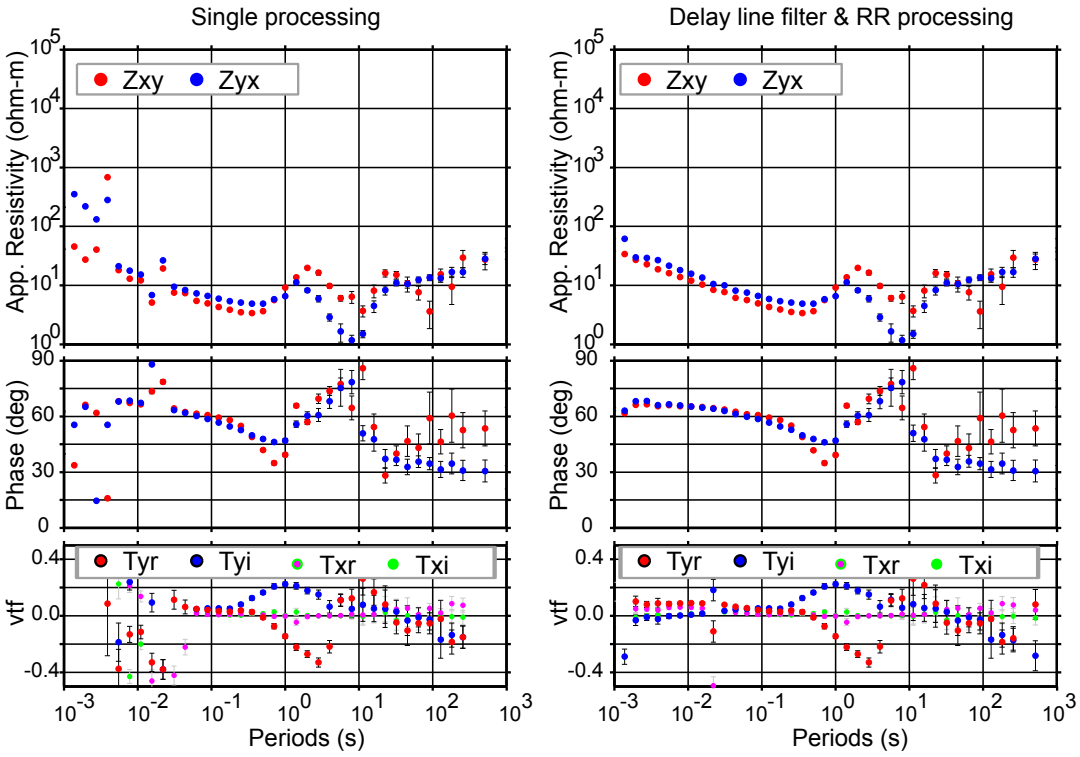
Single processing
Delay line filter & RR processing
App. Resistivity (ohm-m)
Phase (deg)
vtf
Zxy
Zyx
Tyr
Tyi
Txr
Txi
Periods (s)

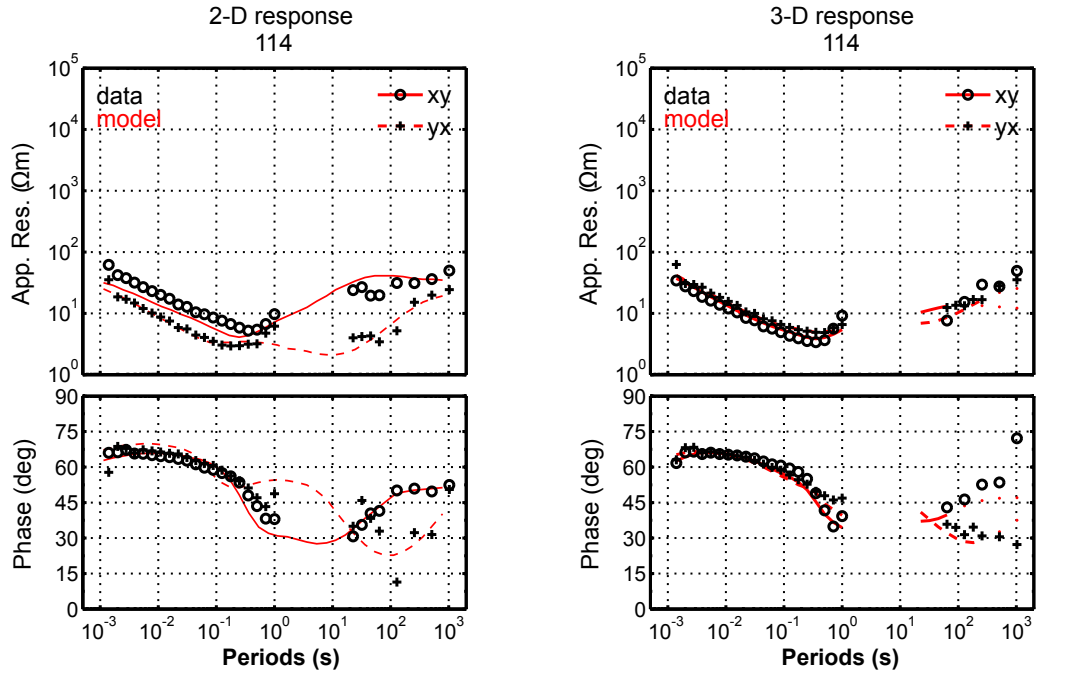
2-D response
114
3-D response
114
data
model
xy
yx
App. Res. (Ωm)
Phase (deg)
Periods (s)

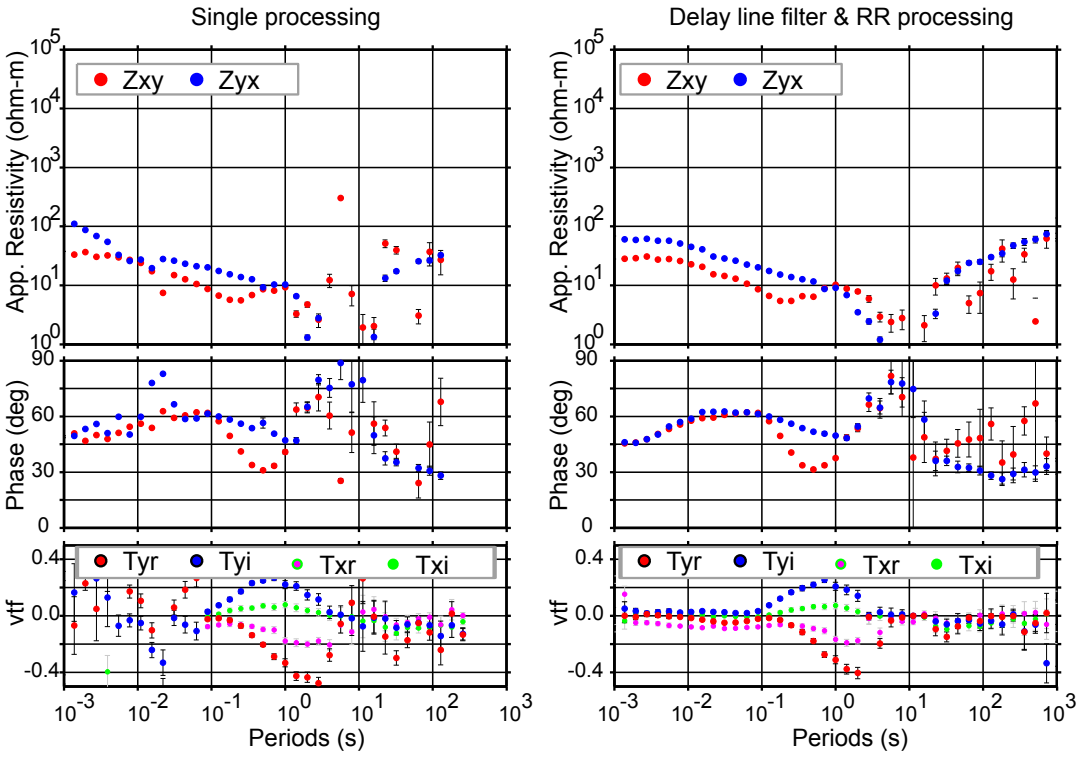
Single processing
Delay line filter & RR processing
App. Resistivity (ohm-m)
Phase (deg)
vtf
Zxy
Zyx
Tyr
Tyi
Txr
Txi
Periods (s)

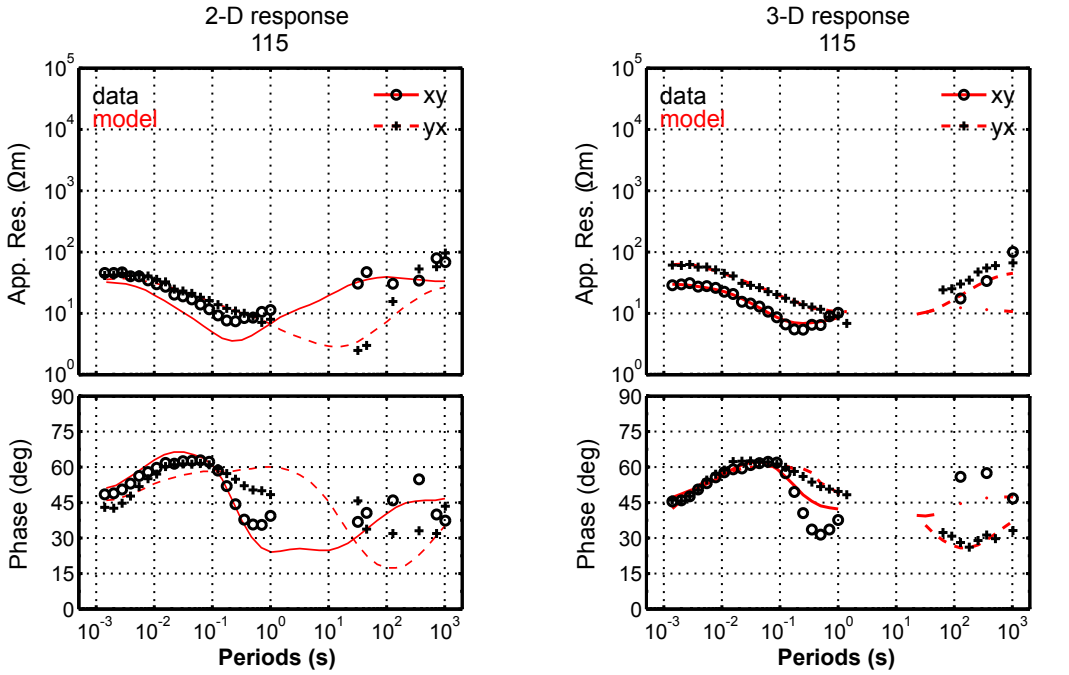
2-D response
115
3-D response
115
data
model
xy
yx
App. Res. (Ωm)
Phase (deg)
Periods (s)

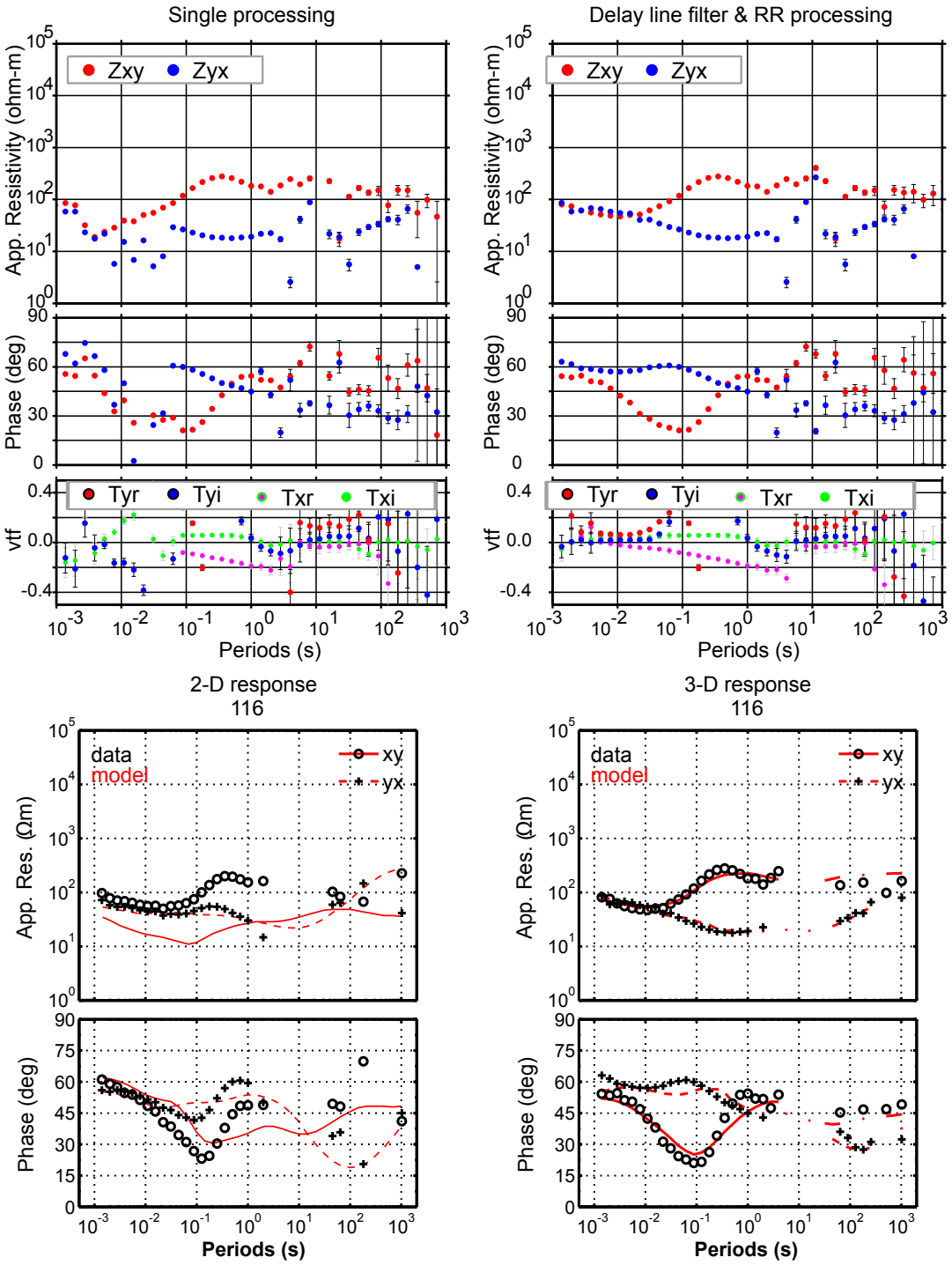
Single processing
Delay line filter & RR processing
App. Resistivity (ohm-m)
Phase (deg)
vtf
Zxy
Zyx
Tyr
Tyi
Txr
Txi
Periods (s)
2-D response
116
3-D response
116
data
model
xy
yx
App. Res. (Ωm)
Phase (deg)
Periods (s)

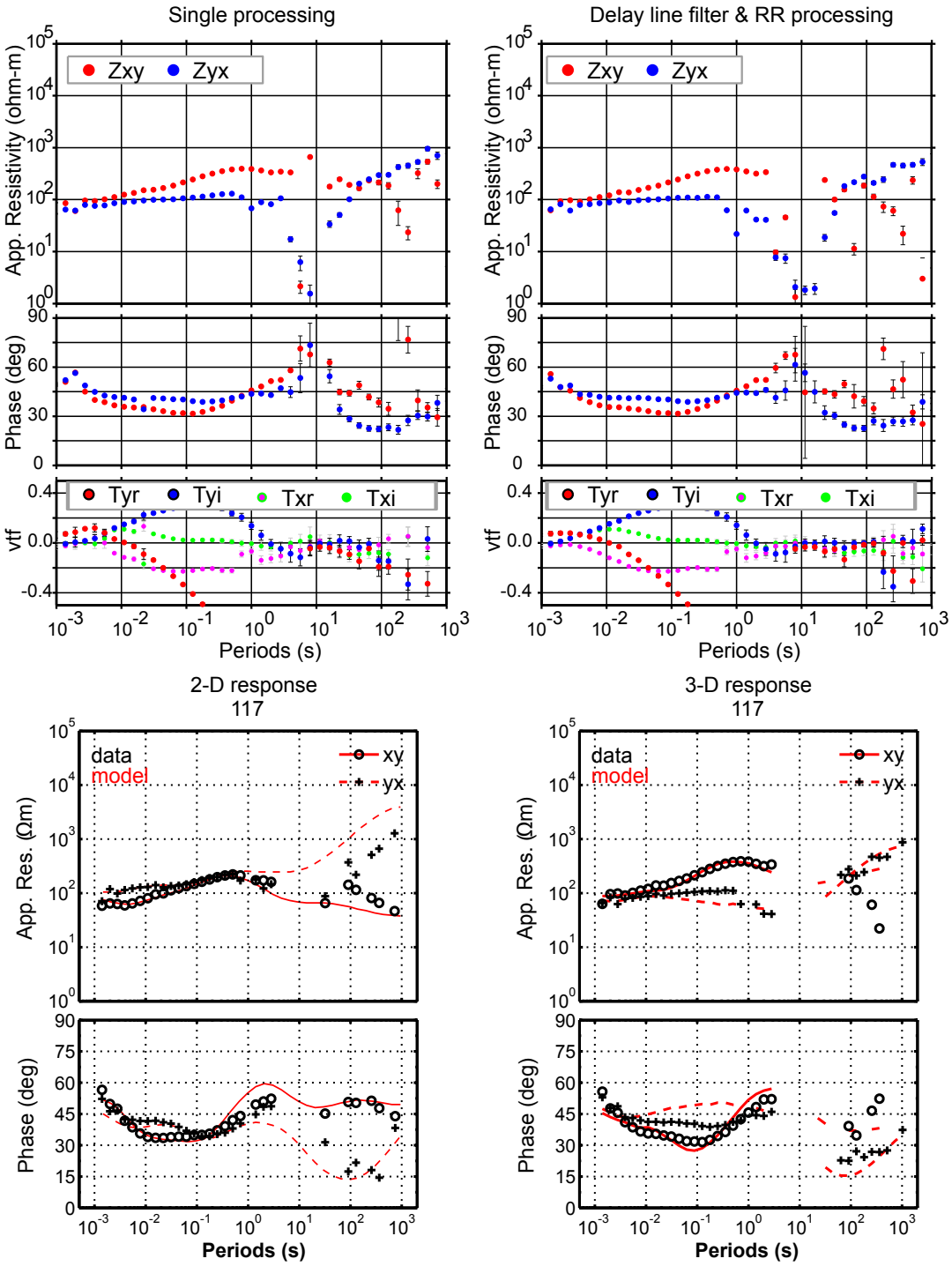
Single processing
Delay line filter & RR processing
App. Resistivity (ohm-m)
Phase (deg)
vtf
Zxy
Zyx
Tyr
Tyi
Txr
Txi
Periods (s)
2-D response
117
3-D response
117
data
model
xy
yx
App. Res. (Ωm)
Phase (deg)
Periods (s)

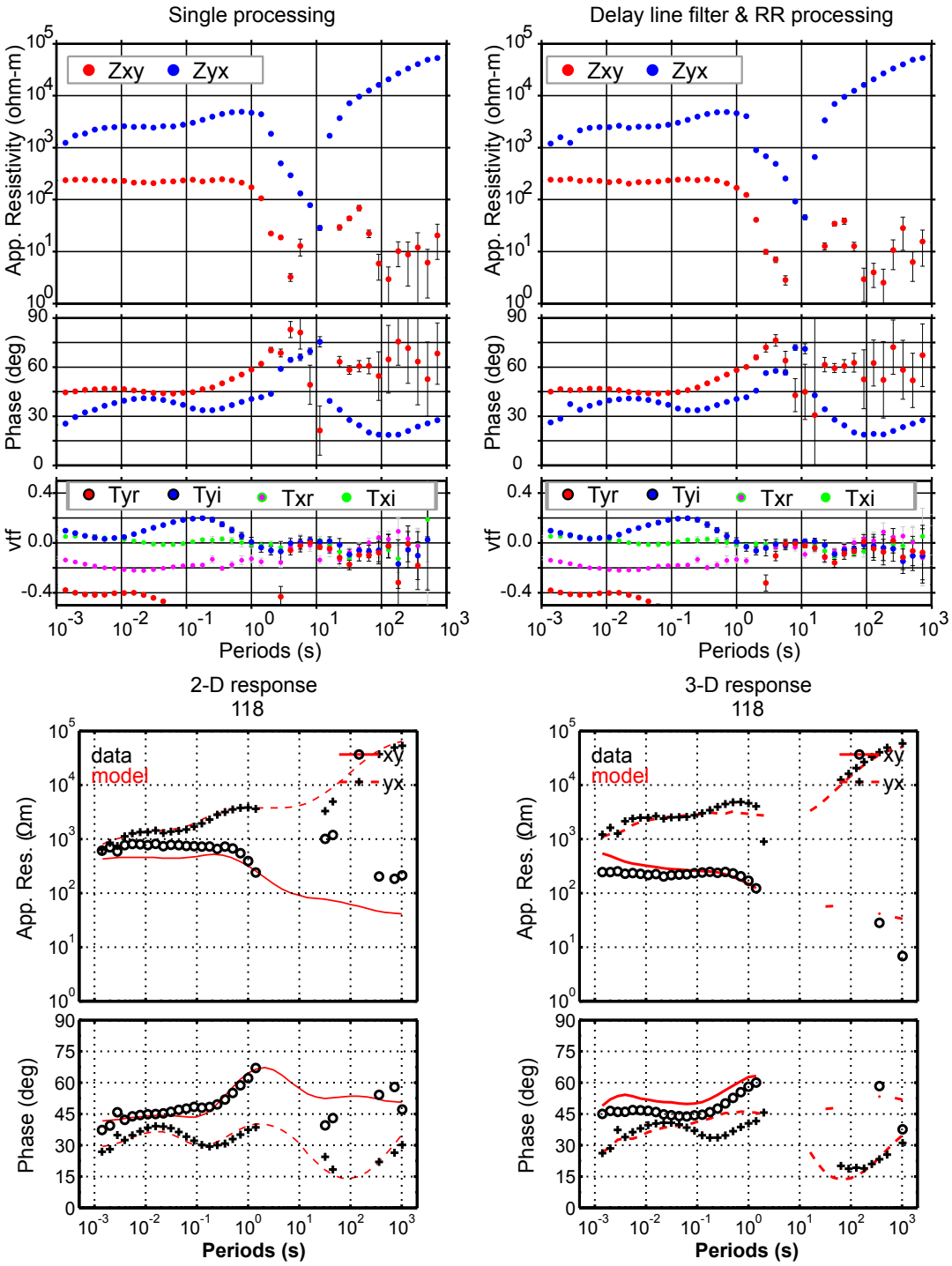
Single processing
Delay line filter & RR processing
App. Resistivity (ohm-m)
Zxy
Zyx
Phase (deg)
vtf
Tyr
Tyi
Txr
Txi
Periods (s)
2-D response
118
3-D response
118
data
model
xy
yx
App. Res. (Ωm)
Phase (deg)
Periods (s)

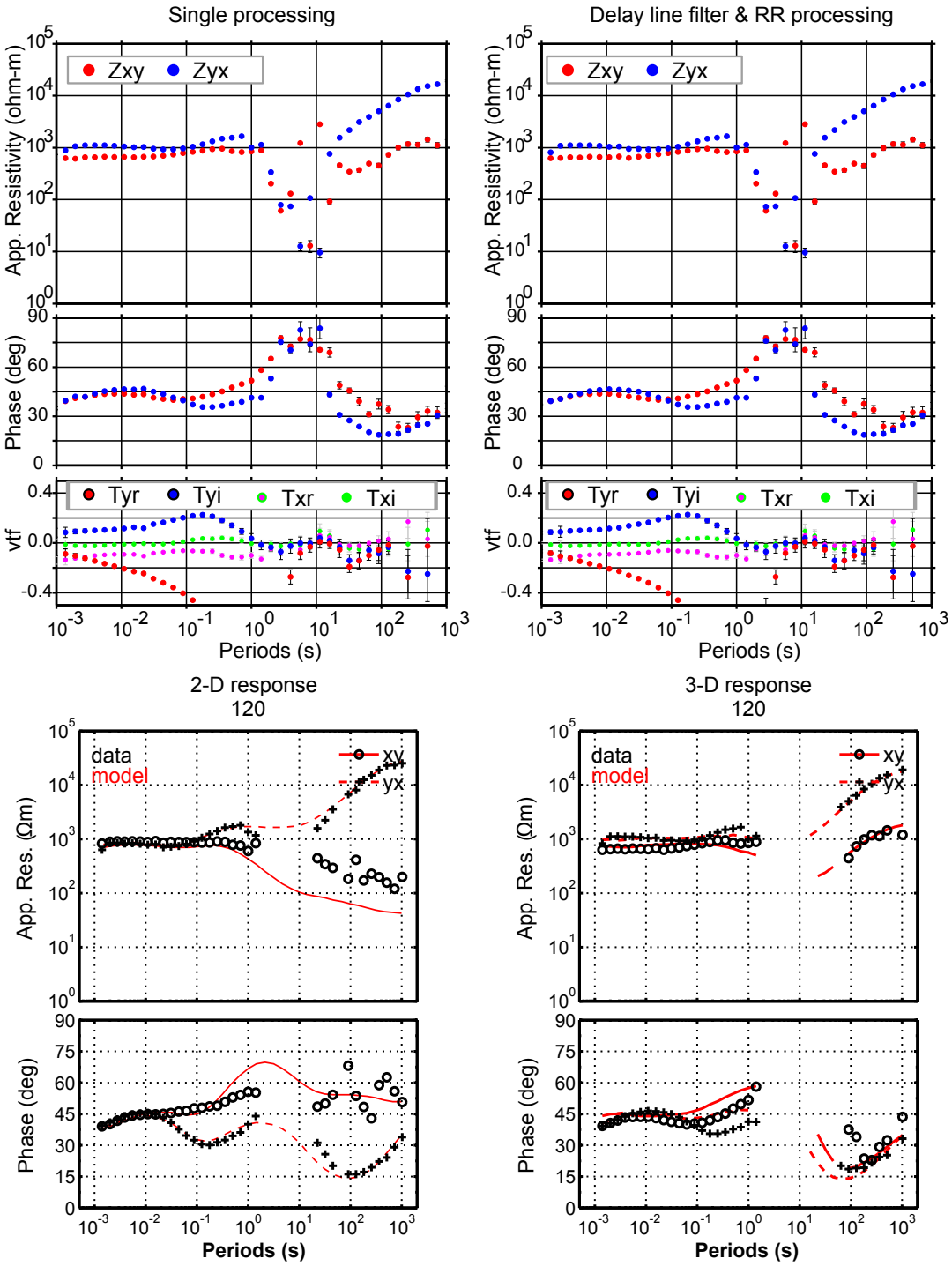
Single processing
Delay line filter & RR processing
App. Resistivity (ohm-m)
Phase (deg)
vtf
Zxy
Zyx
Tyr
Tyi
Txr
Txi
Periods (s)
2-D response
120
3-D response
120
data
model
xy
yx
App. Res. (Ωm)
Phase (deg)
Periods (s)

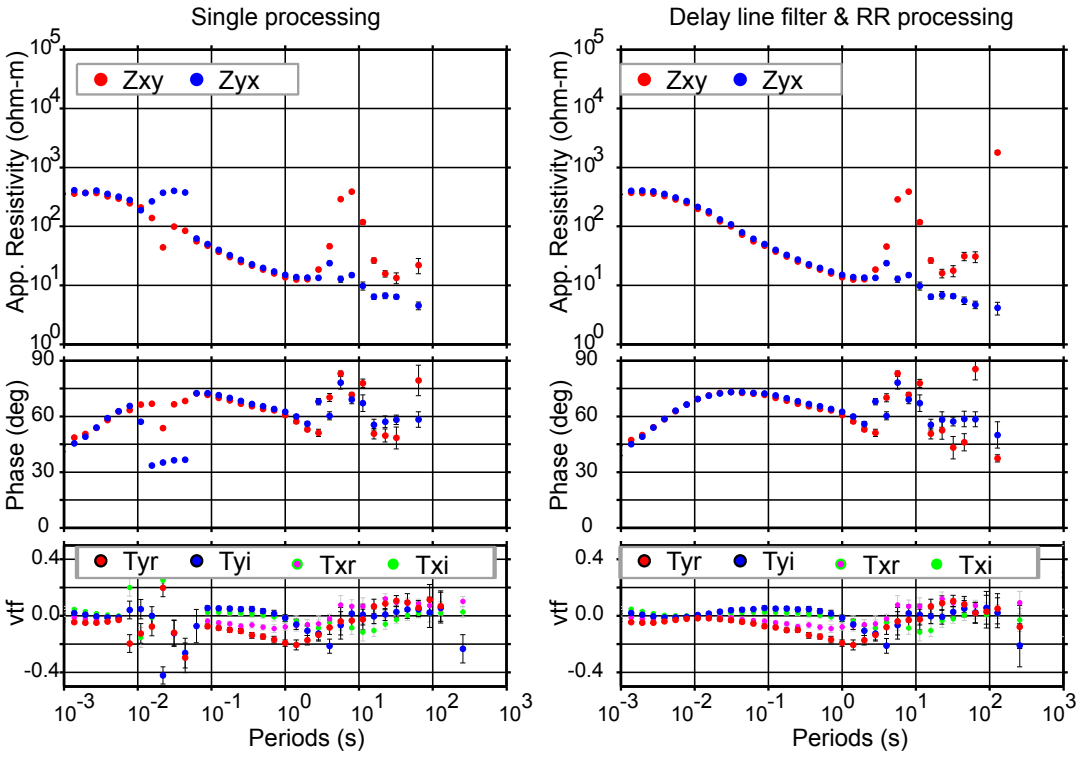
Single processing
Delay line filter & RR processing
App. Resistivity (ohm-m)
Phase (deg)
vtf
Zxy
Zyx
Tyr
Tyi
Txr
Txi
Periods (s)

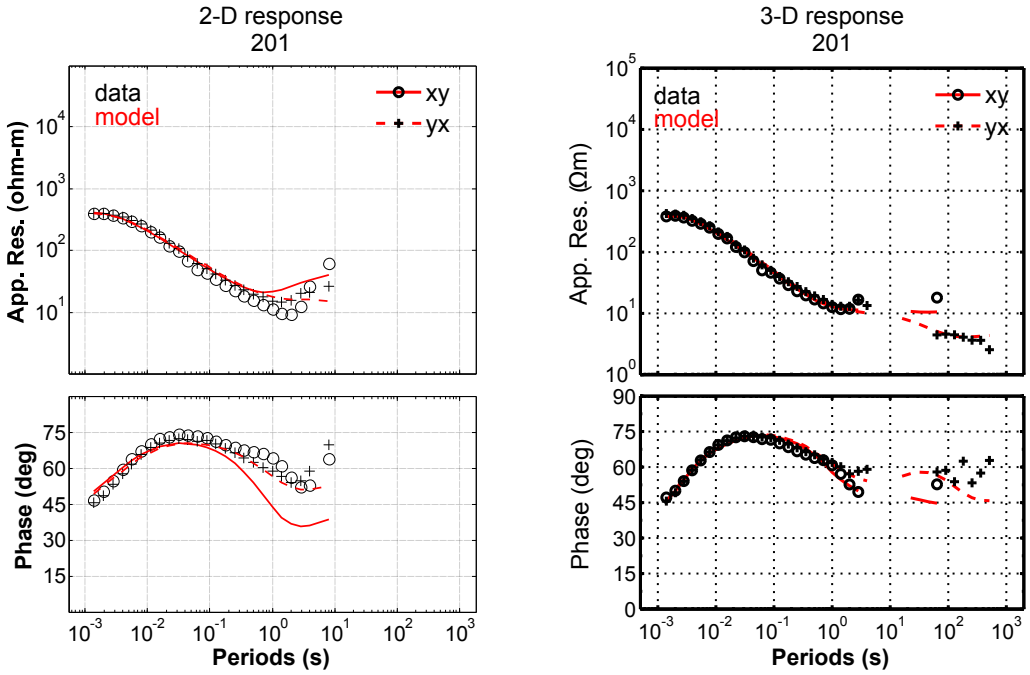
2-D response
201
3-D response
201
data
model
xy
yx
App. Res. (ohm-m)
App. Res. (Ωm)
Phase (deg)
Periods (s)

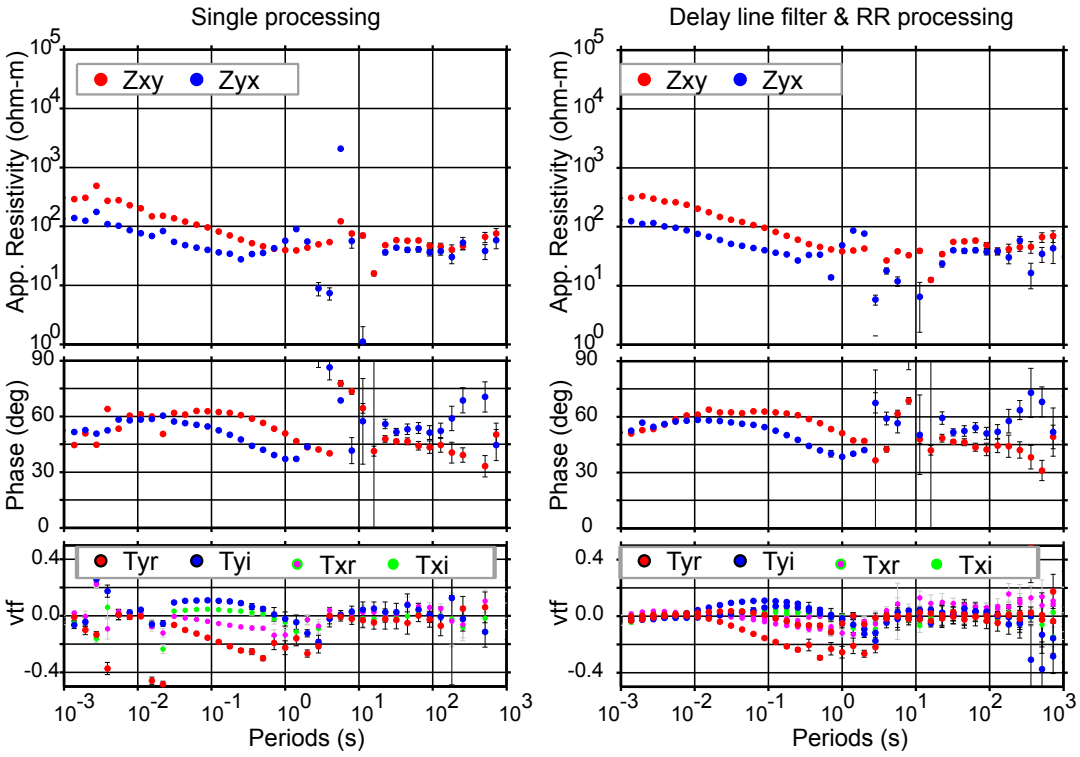
Single processing
Delay line filter & RR processing
App. Resistivity (ohm-m)
Phase (deg)
vtf
Zxy
Zyx
Tyr
Tyi
Txr
Txi
Periods (s)

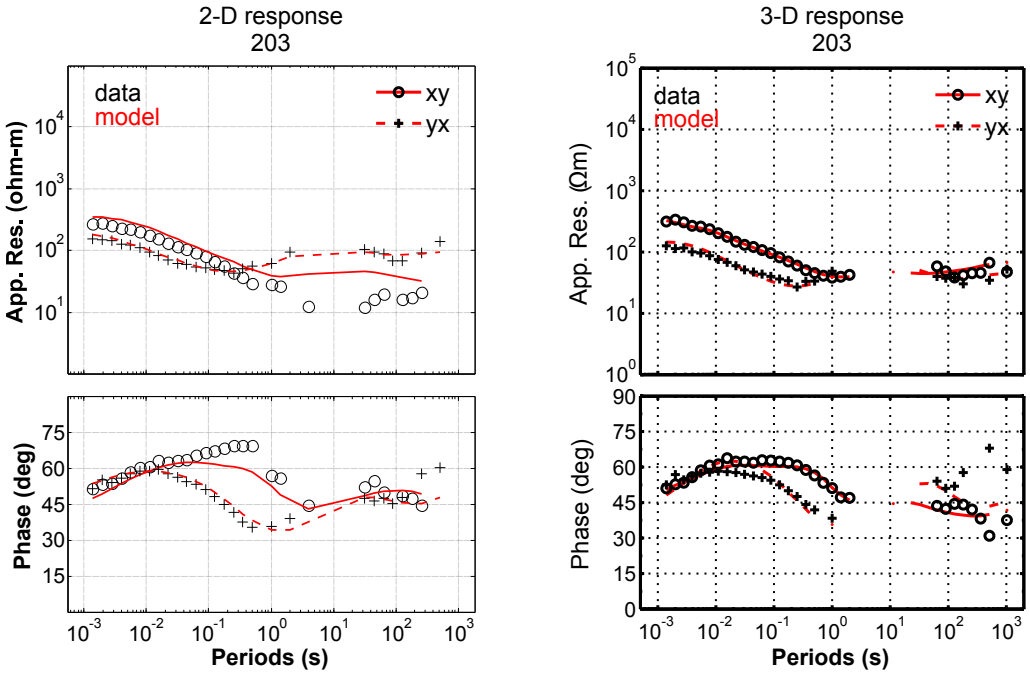
2-D response
203
3-D response
203
data
model
xy
yx
App. Res. (ohm-m)
App. Res. (Ωm)
Phase (deg)
Periods (s)

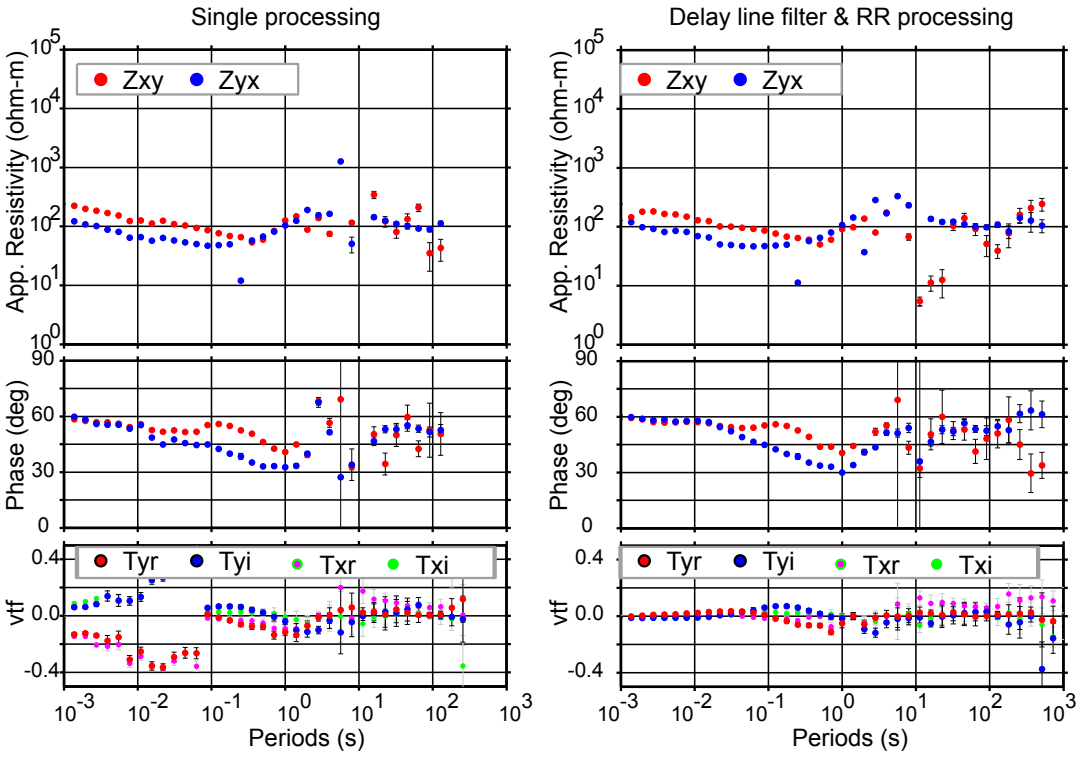
Single processing
Delay line filter & RR processing
App. Resistivity (ohm-m)
Phase (deg)
vtf
Zxy
Zyx
Tyr
Tyi
Txr
Txi
Periods (s)

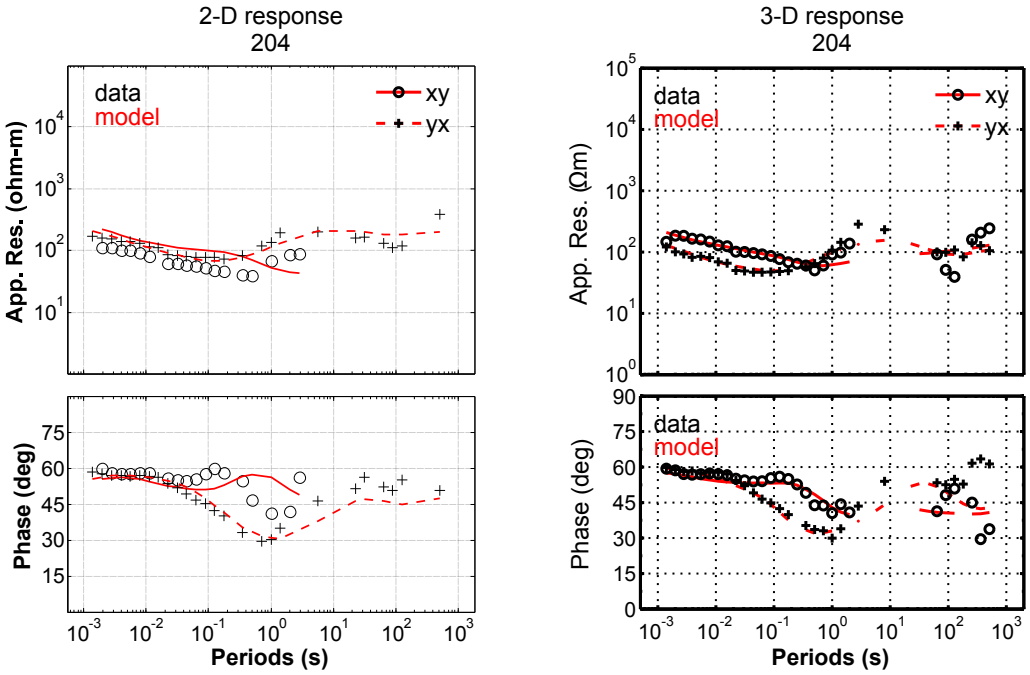
2-D response
204
3-D response
204
data
model
xy
yx
App. Res. (ohm-m)
App. Res. (Ωm)
Phase (deg)
Periods (s)

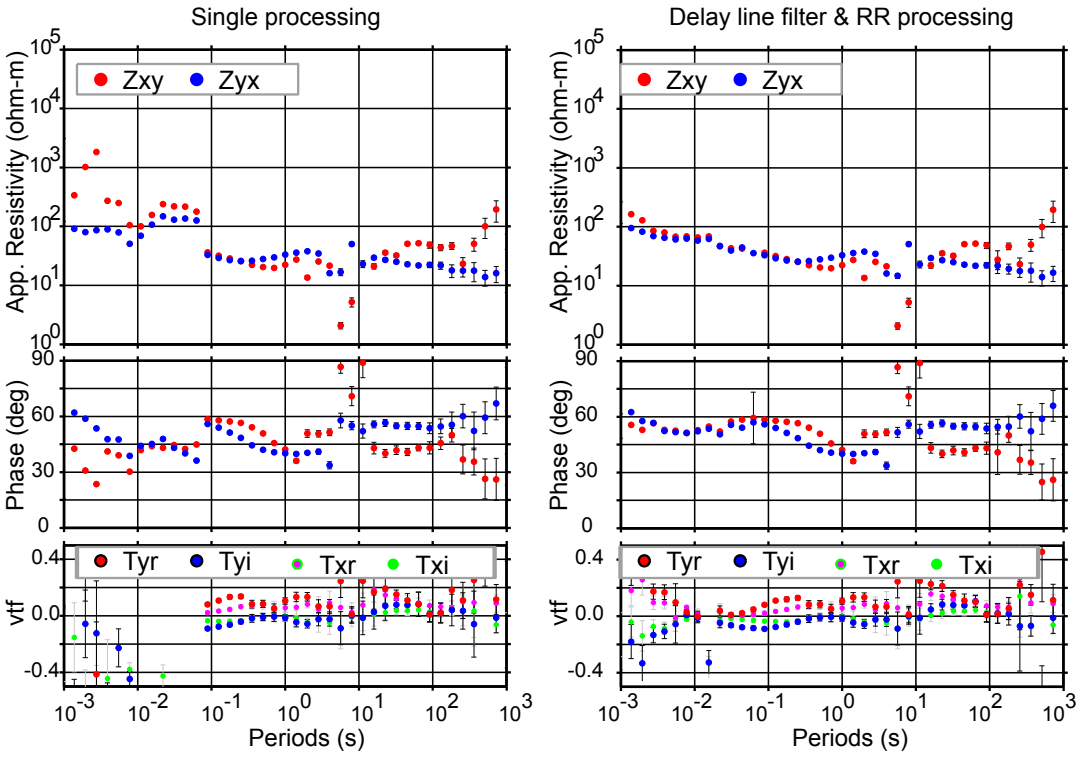
Single processing
Delay line filter & RR processing
App. Resistivity (ohm-m)
Phase (deg)
vtf
Zxy
Zyx
Tyr
Tyi
Txr
Txi
Periods (s)

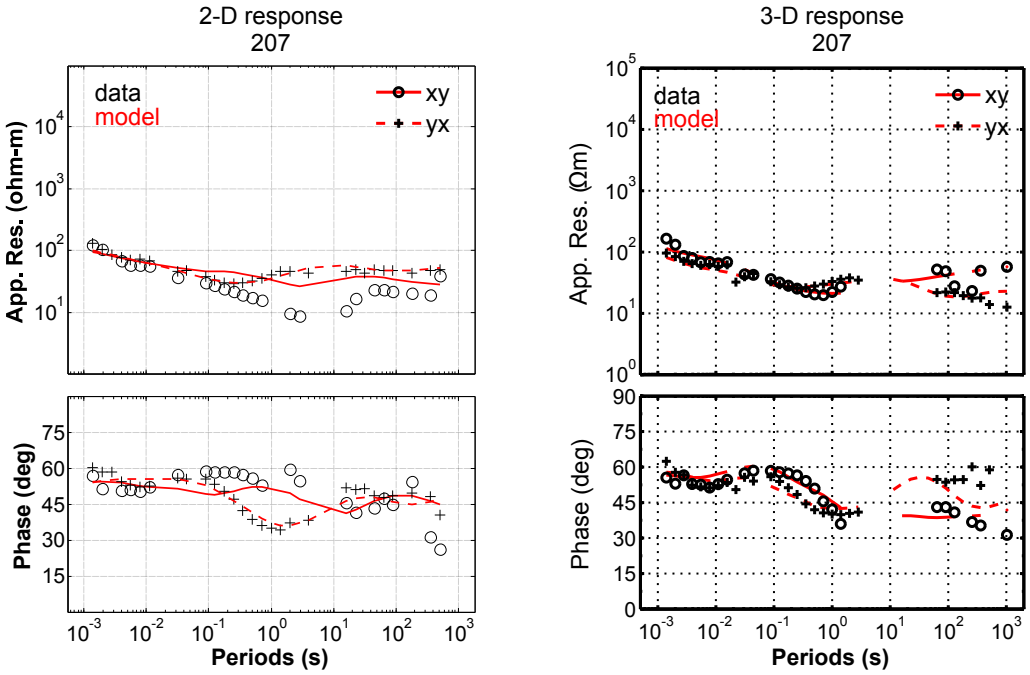
2-D response
207
3-D response
207
data
model
xy
yx
App. Res. (ohm-m)
App. Res. (Ωm)
Phase (deg)
Periods (s)

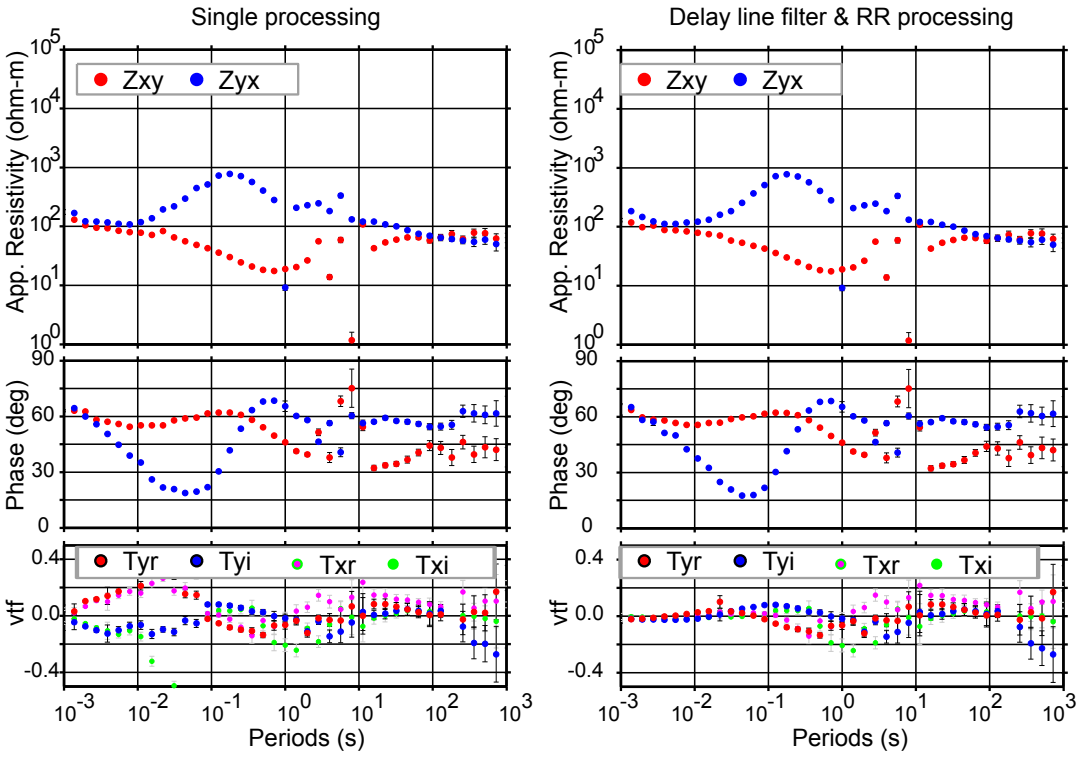
Single processing
Delay line filter & RR processing
App. Resistivity (ohm-m)
Phase (deg)
vtf
Zxy
Zyx
Tyr
Tyi
Txr
Txi
Periods (s)

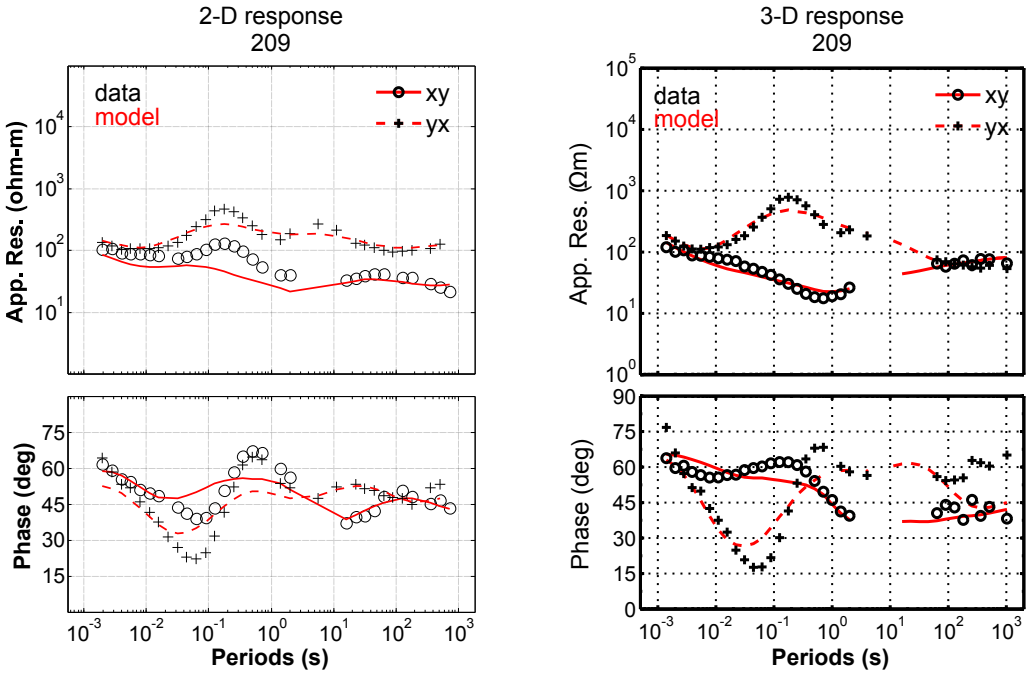
2-D response
209
3-D response
209
data
model
xy
yx
App. Res. (ohm-m)
App. Res. (Ωm)
Phase (deg)
Periods (s)

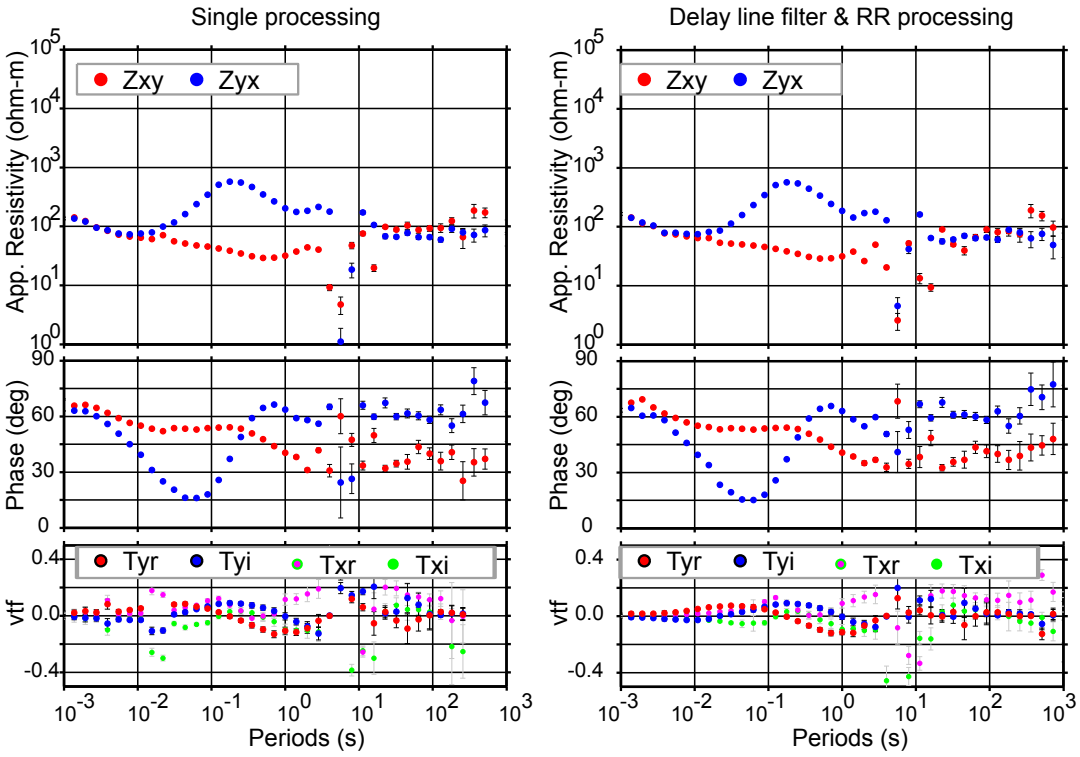
Single processing
Delay line filter & RR processing
App. Resistivity (ohm-m)
Phase (deg)
vtf
Zxy
Zyx
Tyr
Tyi
Txr
Txi
Periods (s)

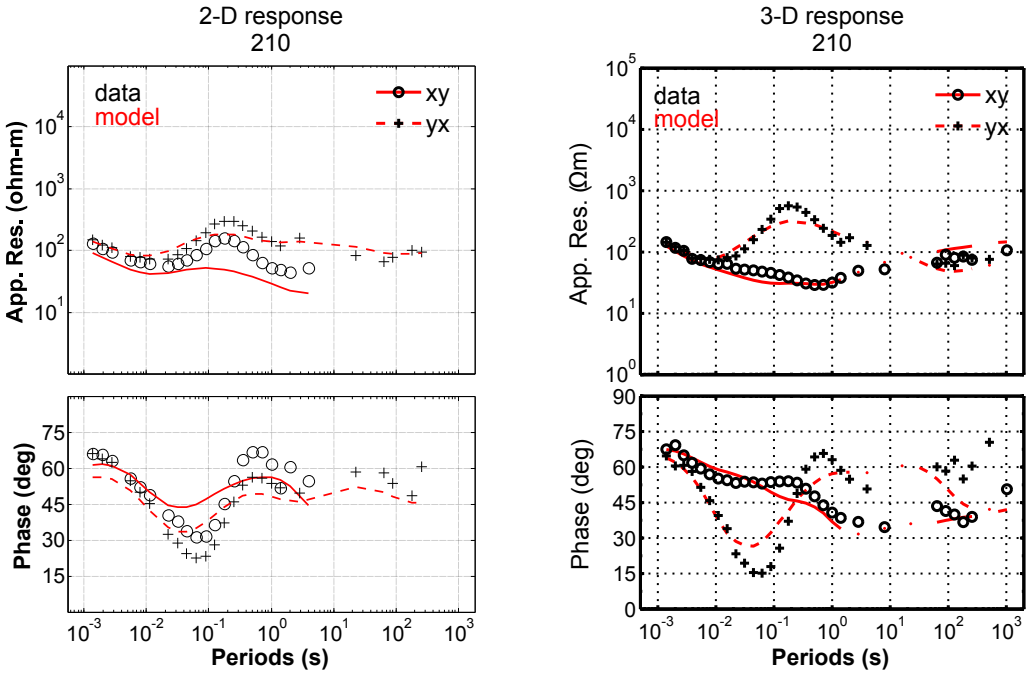
2-D response
210
3-D response
210
data
model
xy
yx
App. Res. (ohm-m)
App. Res. (Ωm)
Phase (deg)
Periods (s)

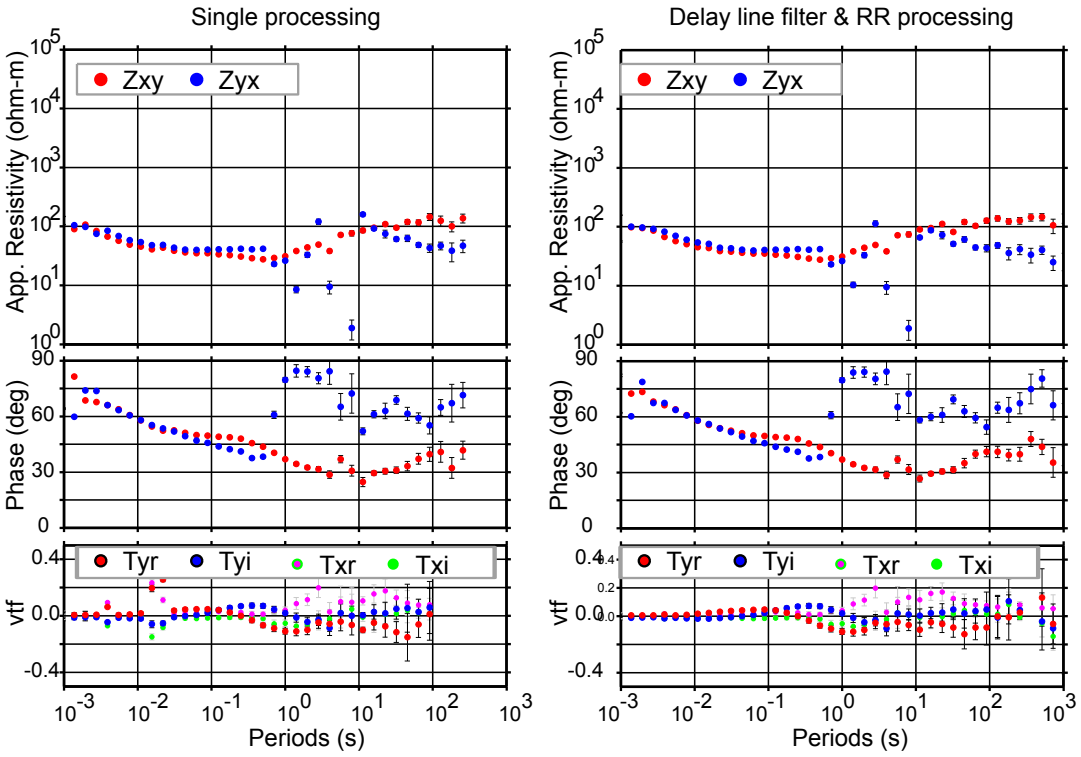
Single processing
Delay line filter & RR processing
App. Resistivity (ohm-m)
Phase (deg)
vtf
Zxy
Zyx
Tyr
Tyi
Txr
Txi
Periods (s)

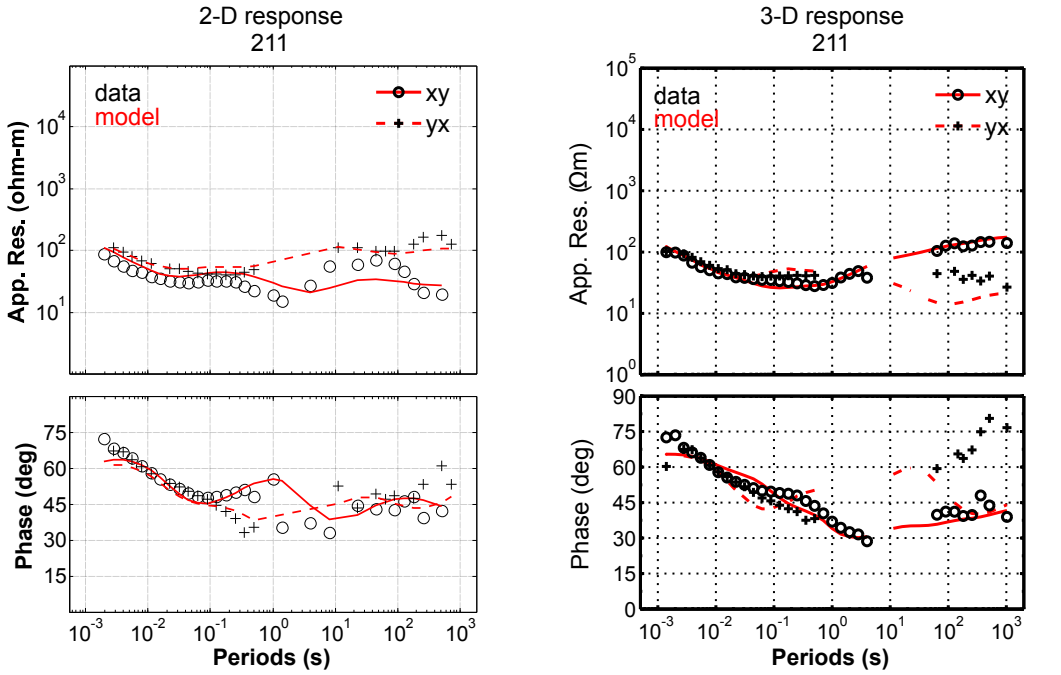
2-D response
211
3-D response
211
data
model
xy
yx
App. Res. (ohm-m)
App. Res. (Ωm)
Phase (deg)
Periods (s)

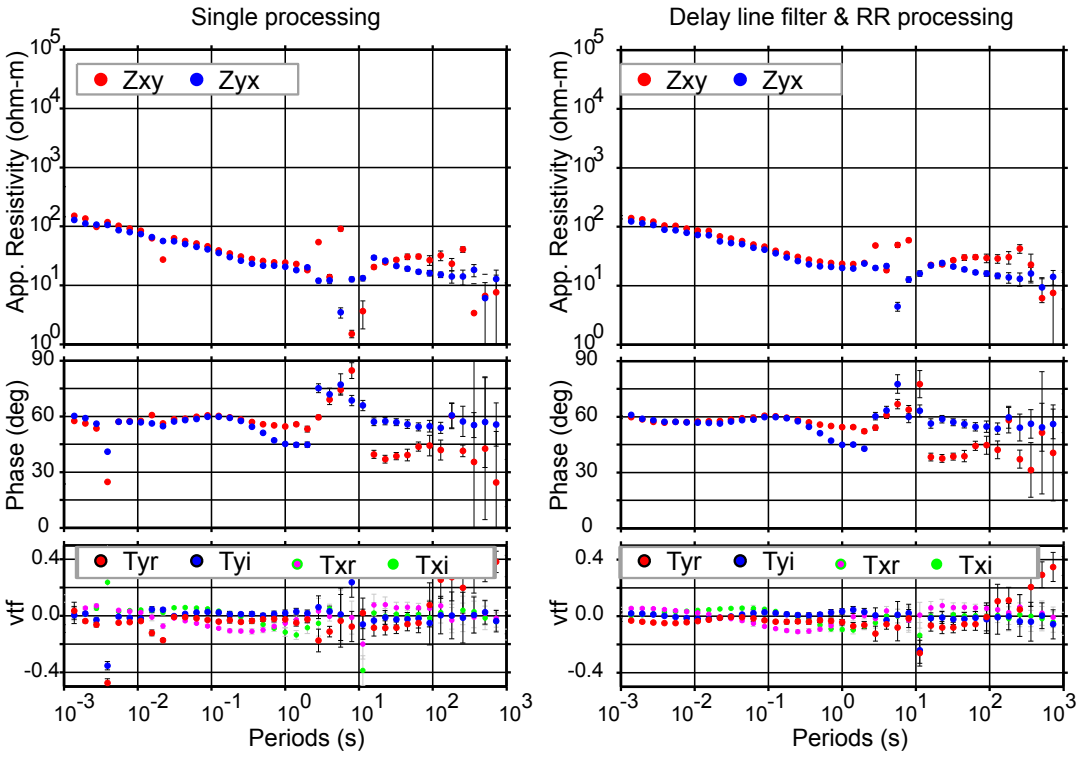
Single processing
Delay line filter & RR processing
App. Resistivity (ohm-m)
Phase (deg)
vtf
Zxy
Zyx
Tyr
Tyi
Txr
Txi
Periods (s)

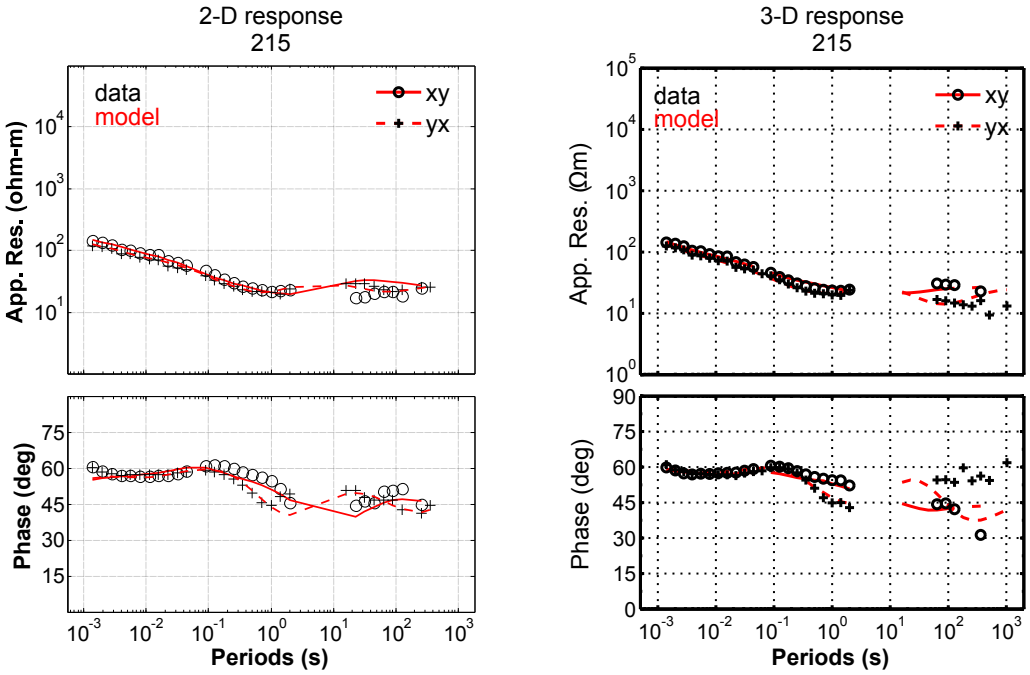
2-D response
215
3-D response
215
data
model
xy
yx
App. Res. (ohm-m)
App. Res. (Ωm)
Phase (deg)
Periods (s)

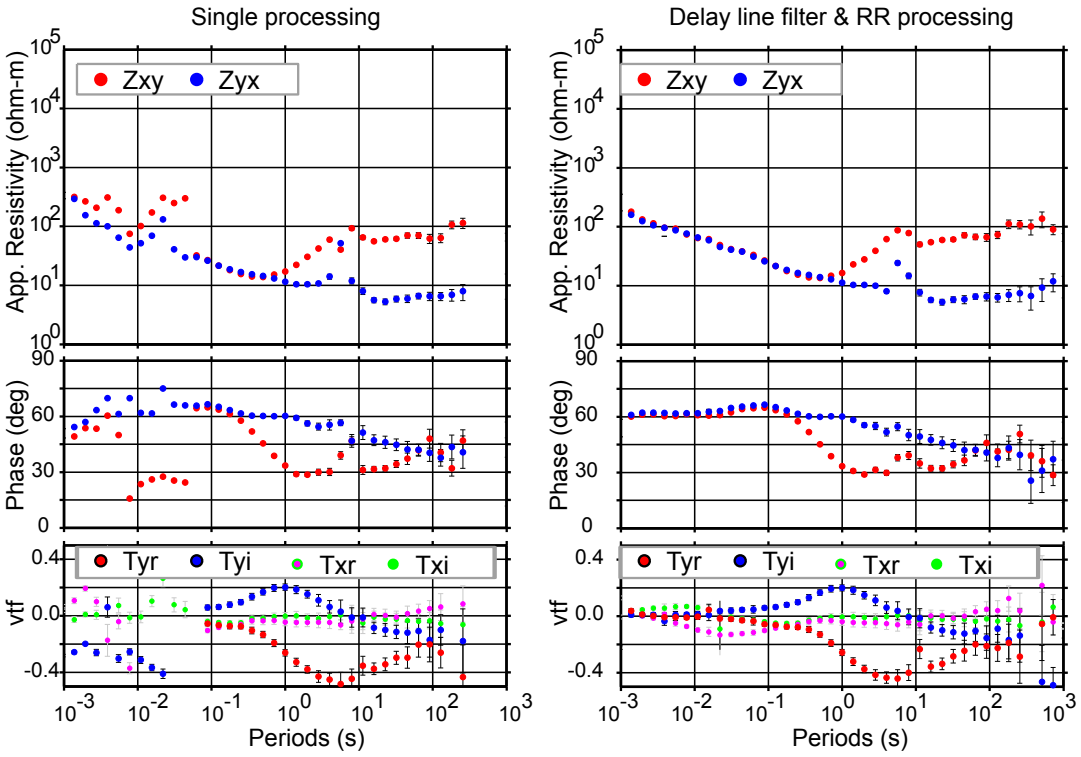
Single processing
Delay line filter & RR processing
App. Resistivity (ohm-m)
Phase (deg)
vtf
Zxy
Zyx
Tyr
Tyi
Txr
Txi
Periods (s)

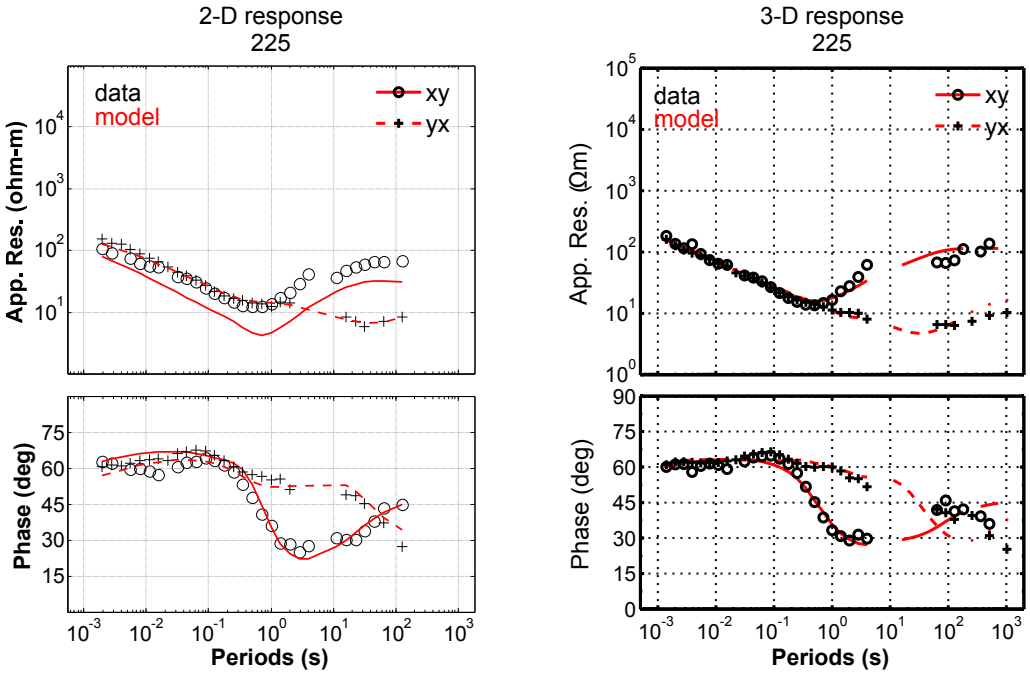
2-D response
225
3-D response
225
data
model
xy
yx
App. Res. (ohm-m)
App. Res. (Ωm)
Phase (deg)
Periods (s)

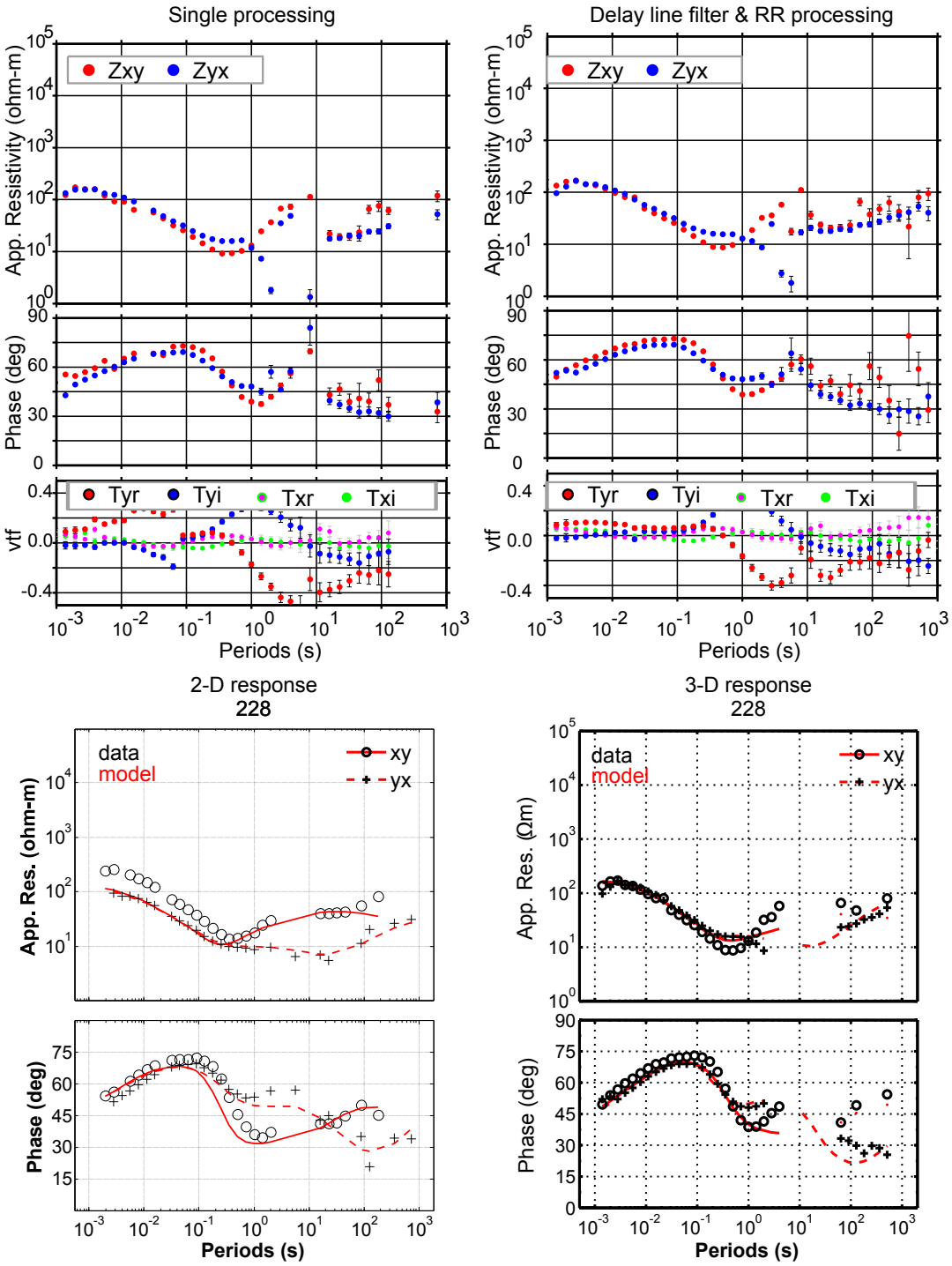
Single processing
Delay line filter & RR processing
App. Resistivity (ohm-m)
Phase (deg)
vtf
Zxy
Zyx
Tyr
Tyi
Txr
Txi
Periods (s)
2-D response
228
3-D response
228
data
model
xy
yx
App. Res. (ohm-m)
App. Res. (Ωm)
Phase (deg)
Periods (s)

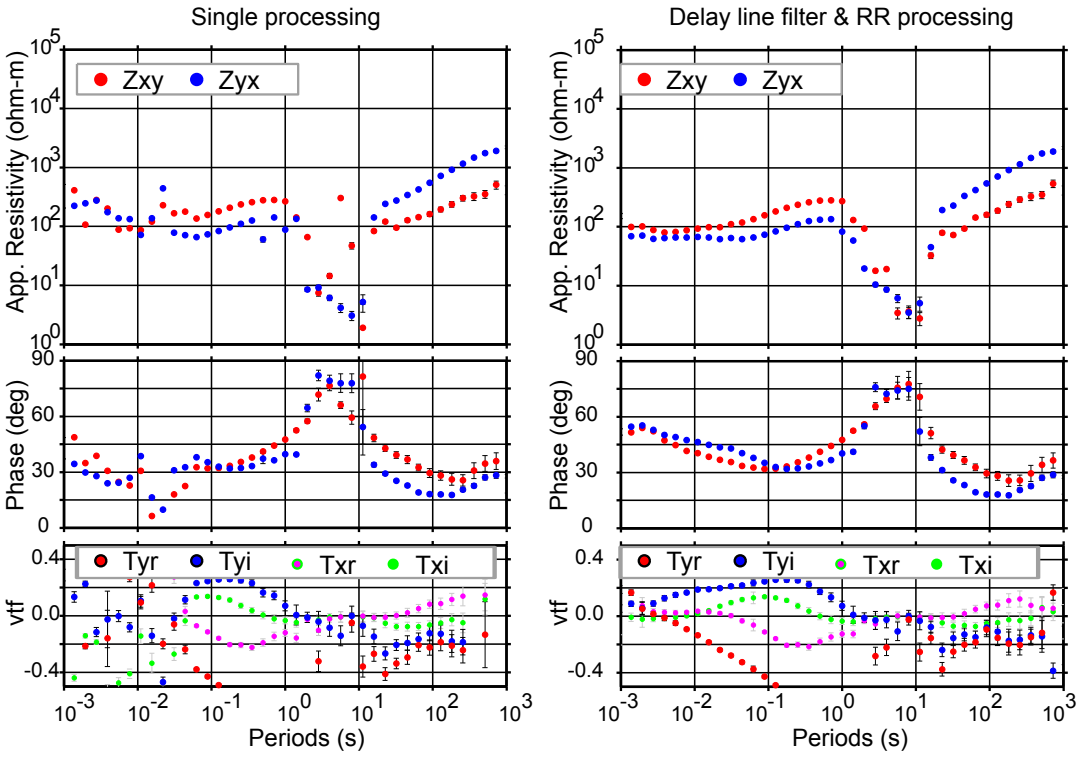
Single processing
Delay line filter & RR processing
App. Resistivity (ohm-m)
Phase (deg)
vtf
Zxy
Zyx
Tyr
Tyi
Txr
Txi
Periods (s)

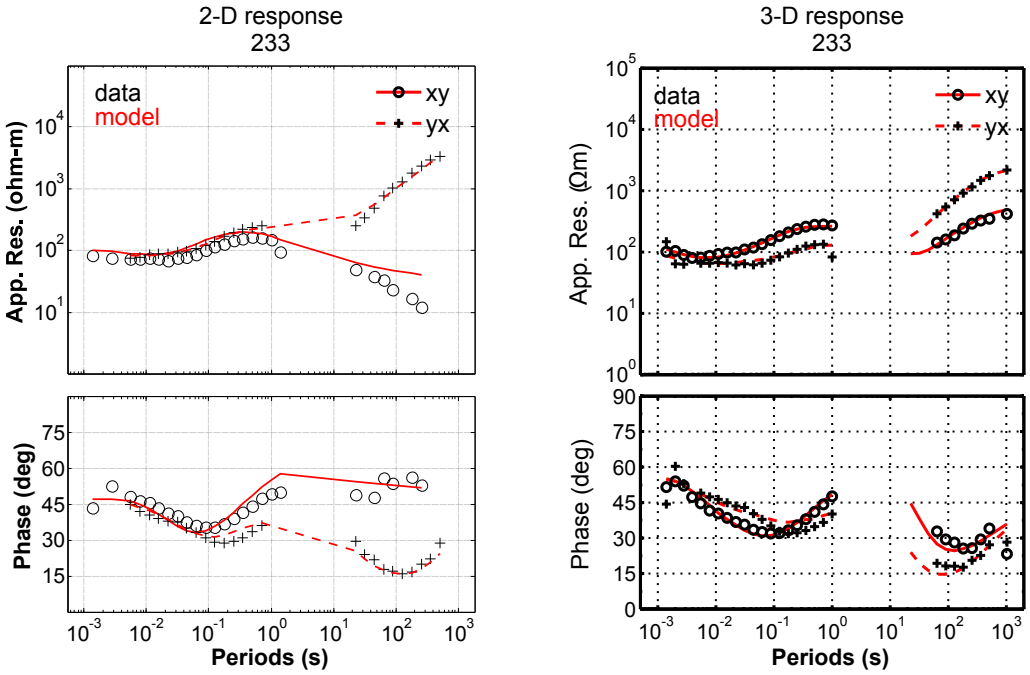
2-D response
233
3-D response
233
data
model
xy
yx
App. Res. (ohm-m)
App. Res. (Ωm)
Phase (deg)
Periods (s)

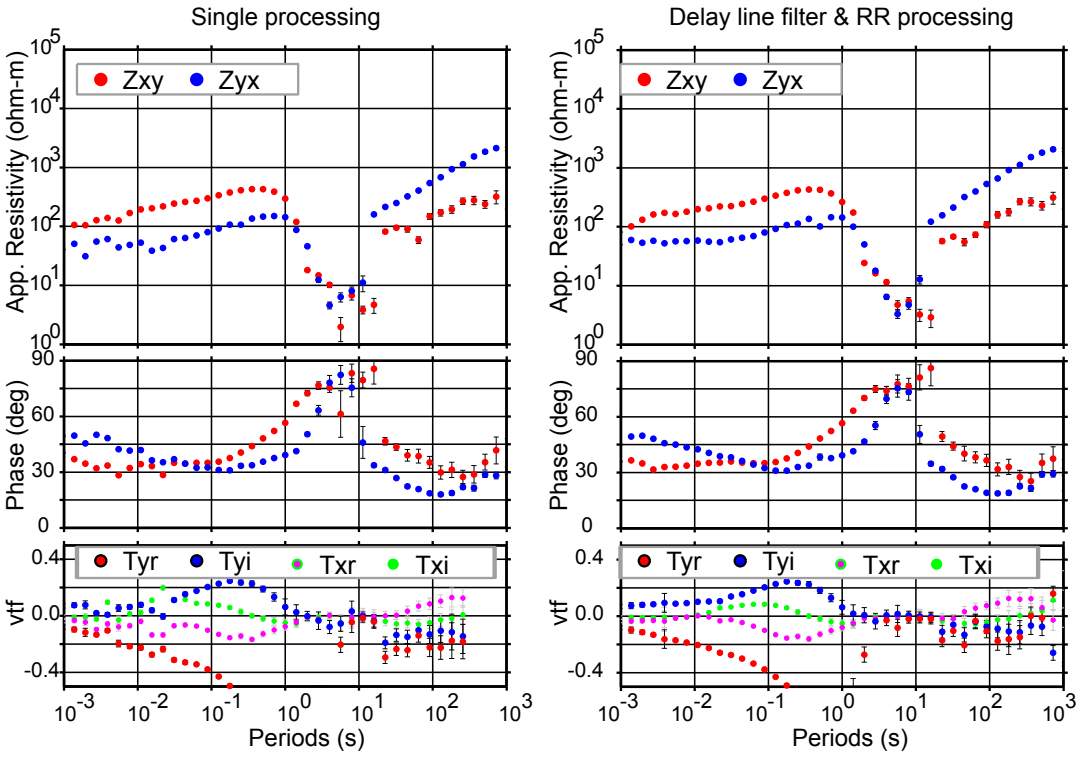
Single processing
Delay line filter & RR processing
App. Resistivity (ohm-m)
Phase (deg)
vtf
Zxy
Zyx
Tyr
Tyi
Txr
Txi
Periods (s)

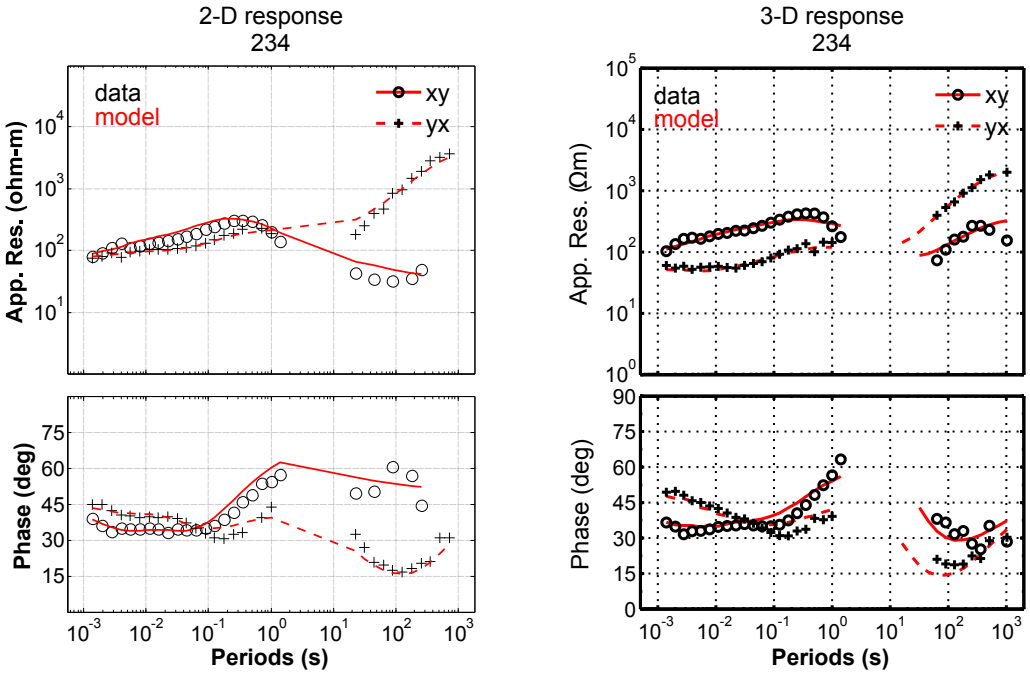
2-D response
234
3-D response
234
data
model
xy
yx
App. Res. (ohm-m)
App. Res. (Ωm)
Phase (deg)
Periods (s)

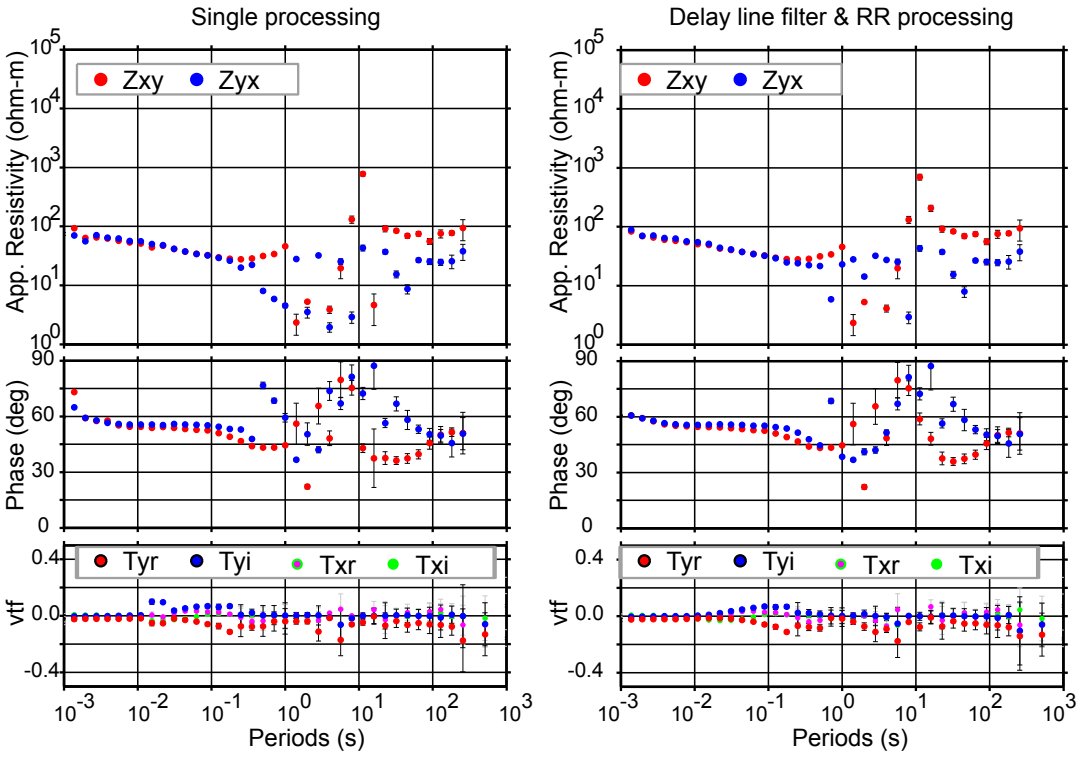
Single processing
Delay line filter & RR processing
App. Resistivity (ohm-m)
Phase (deg)
vtf
Zxy
Zyx
Tyr
Tyi
Txr
Txi
Periods (s)

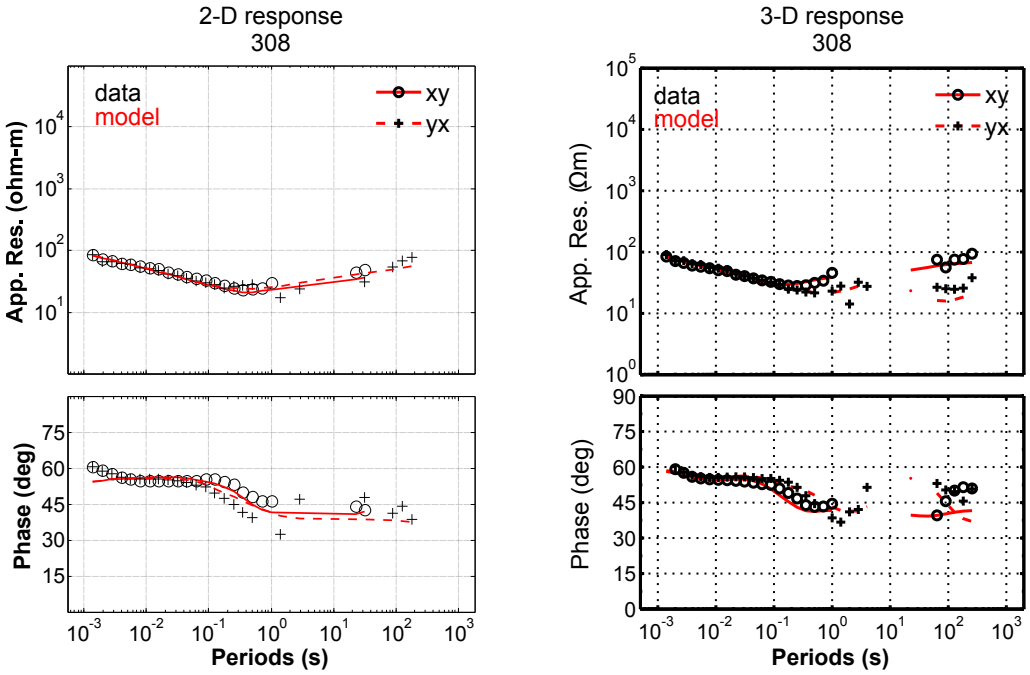
2-D response
308
3-D response
308
data
model
xy
yx
App. Res. (ohm-m)
App. Res. (Ωm)
Phase (deg)
Periods (s)

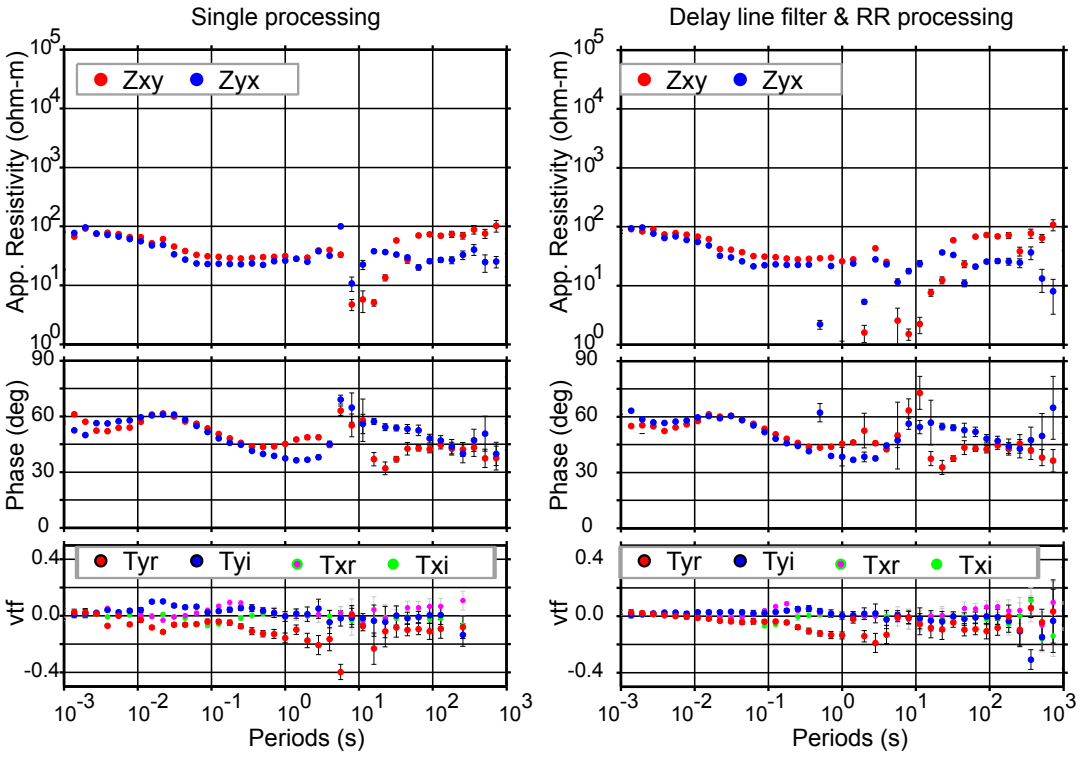
Single processing
Delay line filter & RR processing
App. Resistivity (ohm-m)
Phase (deg)
vtf
Zxy
Zyx
Tyr
Tyi
Txr
Txi
Periods (s)

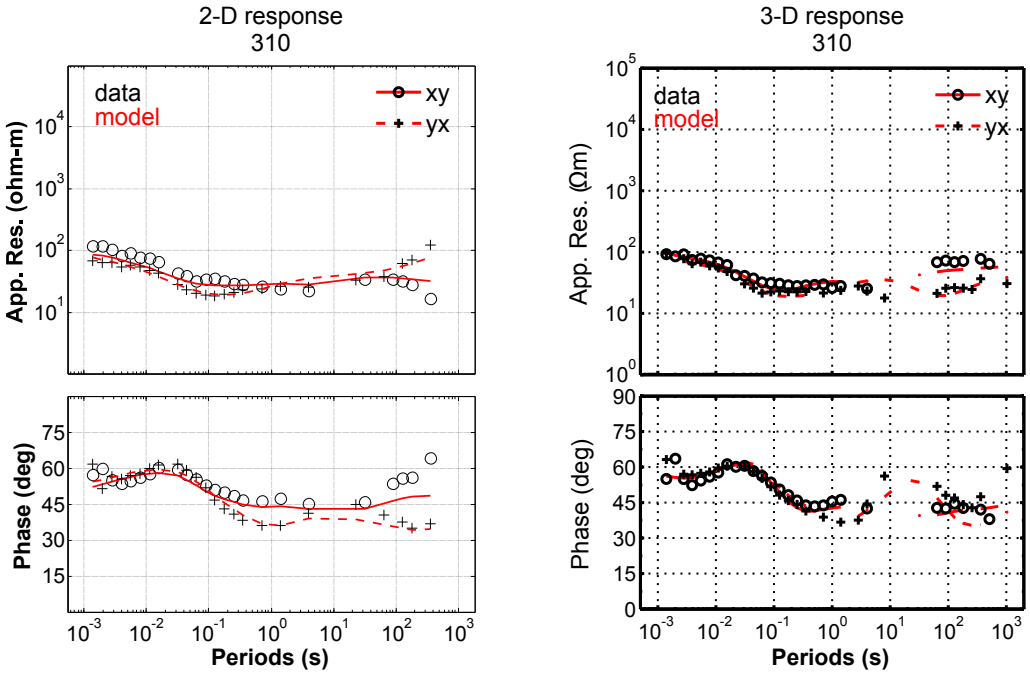
2-D response
310
3-D response
310
data
model
xy
yx
App. Res. (ohm-m)
App. Res. (Ωm)
Phase (deg)
Periods (s)

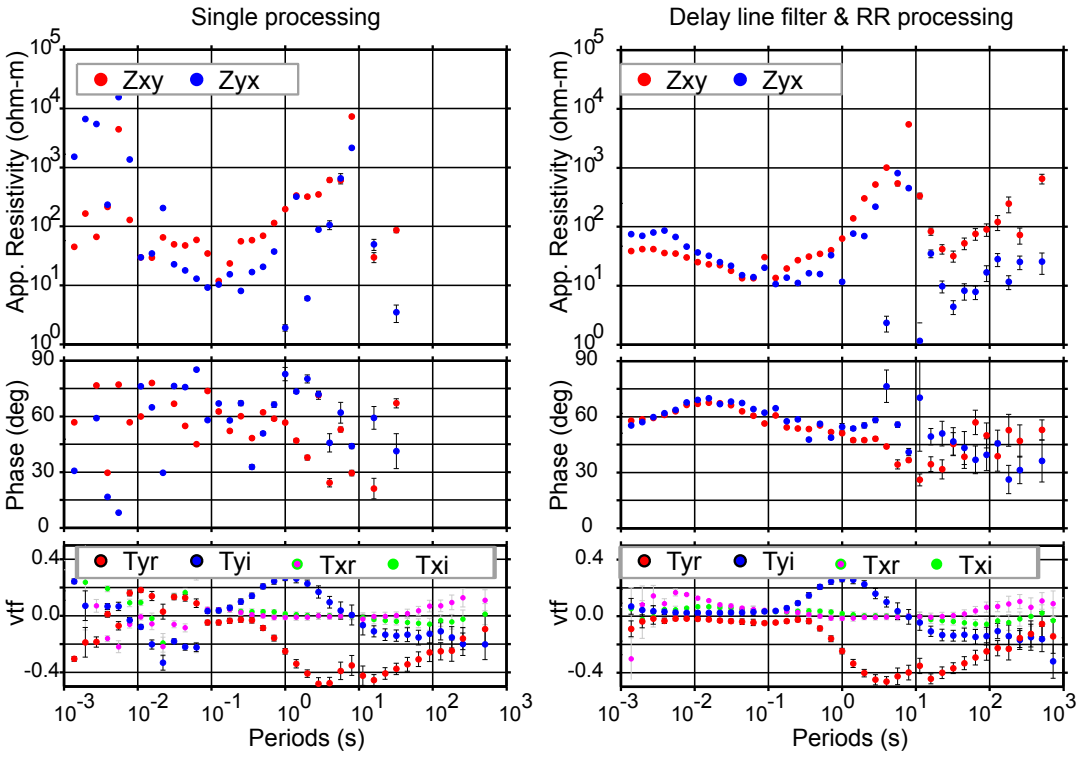
Single processing
Delay line filter & RR processing
App. Resistivity (ohm-m)
Phase (deg)
vtf
Zxy
Zyx
Tyr
Tyi
Txr
Txi
Periods (s)

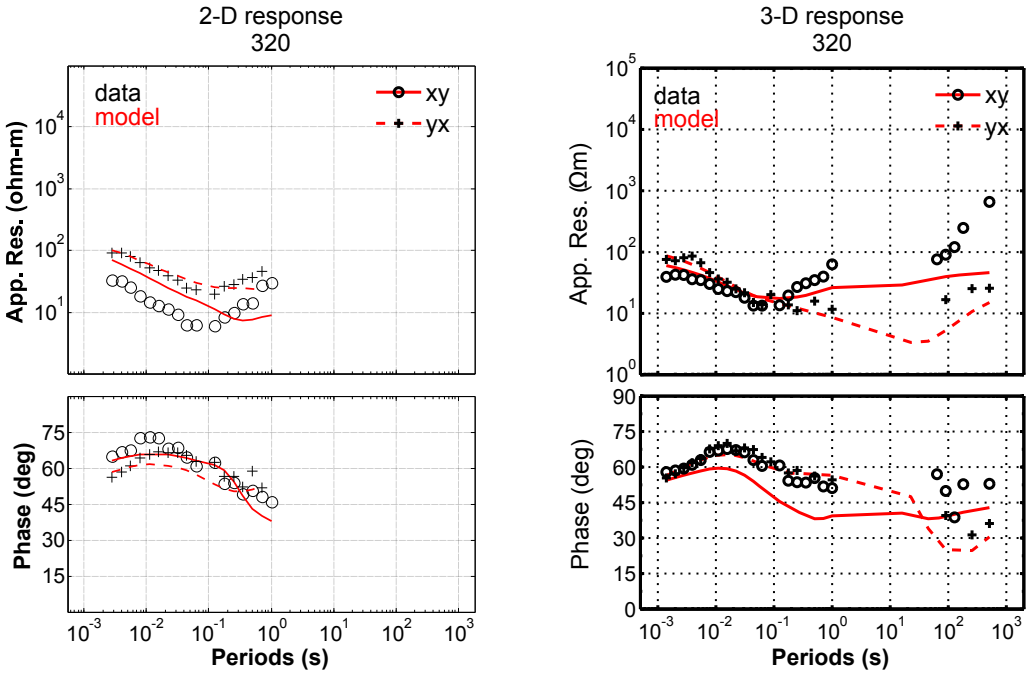
2-D response
320
3-D response
320
data
model
xy
yx
App. Res. (ohm-m)
App. Res. (Ωm)
Phase (deg)
Periods (s)

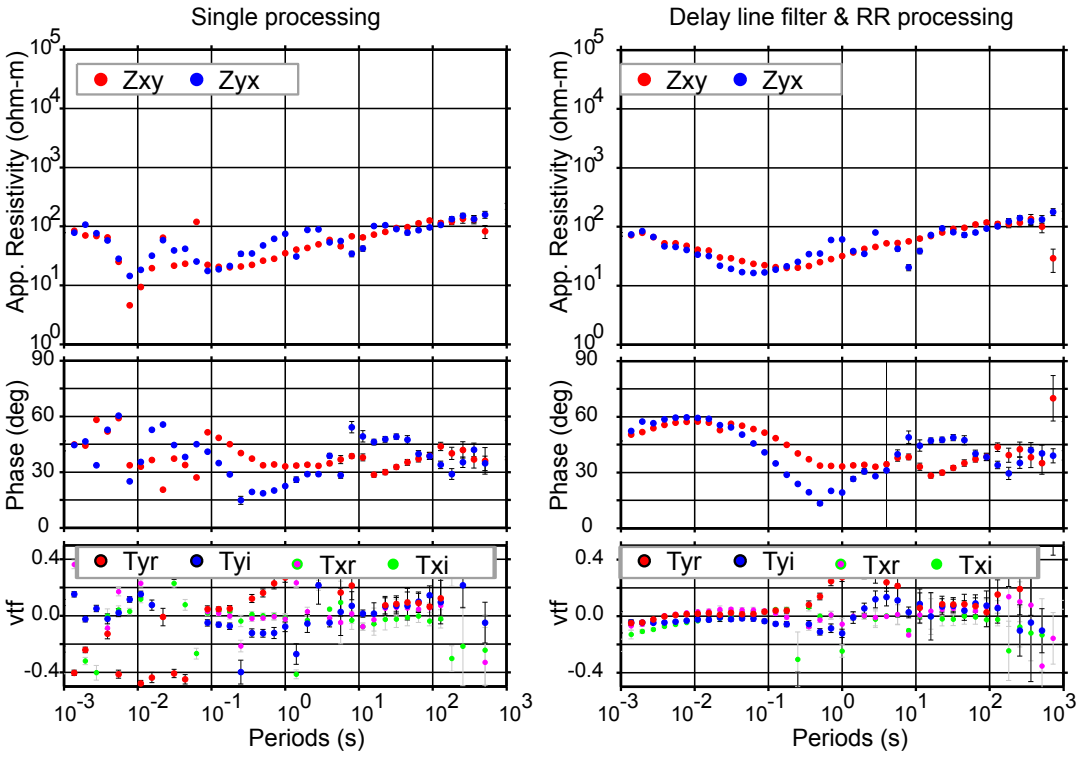
Single processing
Delay line filter & RR processing
App. Resistivity (ohm-m)
Phase (deg)
vtf
Zxy
Zyx
Tyr
Tyi
Txr
Txi
Periods (s)

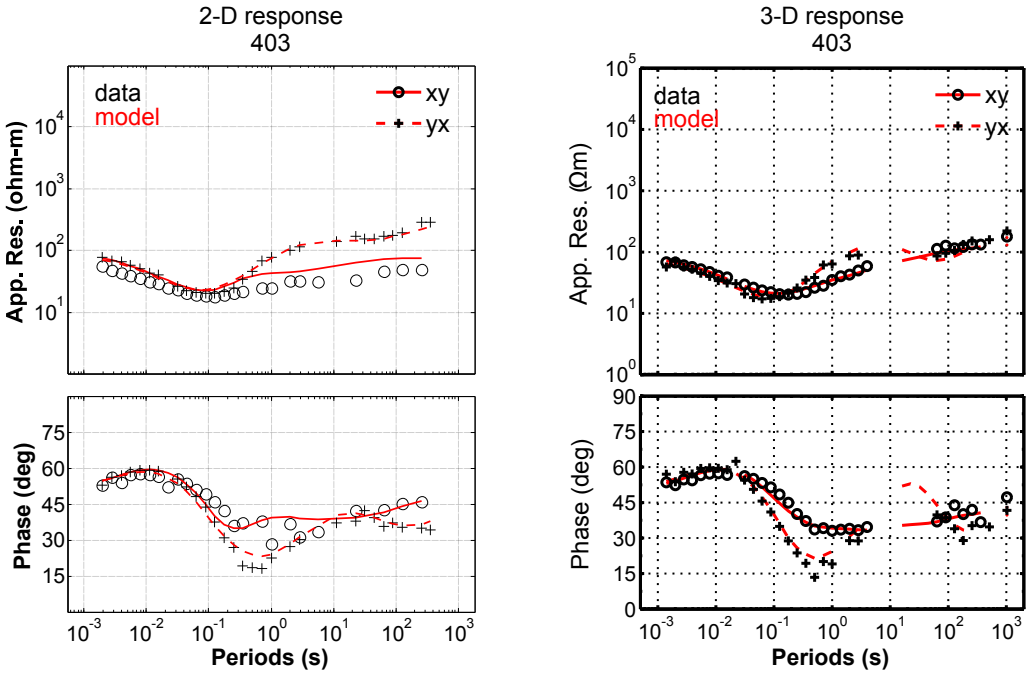
2-D response
403
3-D response
403
data
model
xy
yx
App. Res. (ohm-m)
App. Res. (Ωm)
Phase (deg)
Periods (s)

Statement of Original Authorship

I hereby declare that I wrote this dissertation by myself and that all sources quoted, paraphrased or otherwise referred to are acknowledged in the text, as well as in the cited literature.

The work described has not been submitted in any other degree in any university.

Parts of Chapter 4 are submitted and are under revision in *Geothermics*.

Berlin, November 6, 2014
Sintia W. Niasari.

Curriculum Vitae

For reasons of data protection, the curriculum vitae is not included in the online version.

Publications

Paper

S. W. Niasari, G. Muñoz, M. Kholid, and O. Ritter. Electrical conductivity image of the Sipoholon geothermal system, Sumatra, Indonesia. Submitted and under revision in *Geothermics*.

Conferences

2015

S. W. Niasari, G. Muñoz, K. Muhammad, E. Suhanto, and O. Ritter. 3D inversion of magnetotelluric data from the Sipoholon geothermal field, Sumatra, Indonesia. *Proceedings of World Geothermal Congress, Melbourne, Australia, 19-25 April 2015.*

2014

S. W. Niasari, G. Muñoz, and O. Ritter. Subsurface conductivity image from 3D MT inversion of the Sipoholon geothermal field, Indonesia. *Proceedings of 22nd EM Induction Workshop Weimar, Germany, August 24-30, 2014.*

2013

S. W. Niasari, G. Muñoz, M. Kholid, and O. Ritter. Subsurface conductivity image from MT data of the Sipoholon geothermal field, Indonesia. *Proceedings of International Geothermal Conference, Bandung, Indonesia, December 2-6, 2013.*

S. W. Niasari, G. Muñoz, and O. Ritter. 3D inversion of MT data from the Sipoholon geothermal field, Indonesia: Un-rotated vs rotated MT data. *Proceedings of International Geothermal Conference, Bandung, Indonesia, December 2-6, 2013.*

S. W. Niasari, G. Muñoz, M. Kholid, and O. Ritter. 3D inversion of MT data from the Sipoholon geothermal field, Indonesia. *Proceedings of Elektromagnetische Tiefenforschung, Kirchundem, September 23-27, 2013.*

2012

S. W. Niasari, G. Muñoz, M. Kholid, and O. Ritter. 2D model of the Sipoholon geothermal field, Indonesia. *Proceedings of Electromagnetic Induction Workshop, Darwin, Australia, July 25-31, 2012.*

S. W. Niasari, G. Muñoz, M. Kholid, and O. Ritter. Magnetotelluric Exploration of the Sipoholon geothermal field, Indonesia. *Proceedings of EGU (European Geosciences Union), Vienna, Austria, April 23-27, 2012.*

S. W. Niasari, G. Muñoz, K. Muhammad, E. Suhanto, and O. Ritter. Magnetotelluric Exploration of the Sipoholon geothermal field, Indonesia. *Proceedings of fourth European Geothermal PhD Day, March 29-30, 2012.*

S. W. Niasari, G. Muñoz, M. Kholid, and O. Ritter. Magnetotelluric Exploration of the Sipoholon geothermal field, Indonesia - A preliminary study. *Proceedings of Deutsche Geophysikalische Gesellschaft, Köln, February 21-24, 2012.*

2011

S. W. Niasari, G. Muñoz, M. Kholid, and O. Ritter. Magnetotelluric Exploration of the Sipoholon geothermal field, Indonesia - Processing challenge. *Proceedings of Elektromagnetische Tiefenforschung, Neustadt, September 26-30, 2011.*

S. W. Niasari, G. Muñoz, K. Muhammad, E. Suhanto, and O. Ritter. Magnetotelluric Exploration of the Sipoholon geothermal field, Indonesia. *Proceedings of Annual meeting of Indonesian Geothermal Association, December 12-14, 2011.*